

CAPITAL UNIVERSITY OF SCIENCE AND
TECHNOLOGY, ISLAMABAD



Scattering Analysis in Bifurcated
and Trifurcated Waveguides
Involving Structural
Discontinuities

by

Touqeer Nawaz

A thesis submitted in partial fulfillment for the
degree of Doctor of Philosophy

in the

Faculty of Computing
Department of Mathematics

2022

Scattering Analysis in Bifurcated and Trifurcated Waveguides Involving Structural Discontinuities

By

Touqeer Nawaz

(DMT 151002)

Dr. Baris Erbas, Professor

Eskisehir Technical University, Turkey

(Foreign Evaluator 1)

Dr. Layal Hakim, Senior Lecturer

University of Exeter, UK

(Foreign Evaluator 2)

Dr. Muhammad Afzal

(Thesis Supervisor)

Dr. Muhammad Sagheer

(Head, Department of Mathematics)

Dr. Muhammad Abdul Qadir

(Dean, Faculty of Computing)

**DEPARTMENT OF MATHEMATICS
CAPITAL UNIVERSITY OF SCIENCE AND TECHNOLOGY
ISLAMABAD**

2022

Copyright © 2022 by Touqeer Nawaz

All rights reserved. No part of this thesis may be reproduced, distributed, or transmitted in any form or by any means, including photocopying, recording, or other electronic or mechanical methods, by any information storage and retrieval system without the prior written permission of the author.

DEDICATION

To

My Great Father

&

My Great Mother



**CAPITAL UNIVERSITY OF SCIENCE & TECHNOLOGY
ISLAMABAD**

Expressway, Kahuta Road, Zone-V, Islamabad
Phone:+92-51-111-555-666 Fax: +92-51-4486705
Email: info@cust.edu.pk Website: <https://www.cust.edu.pk>

CERTIFICATE OF APPROVAL

This is to certify that the research work presented in the thesis, entitled “**Scattering Analysis in Bifurcated and Trifurcated Waveguides Involving Structural Discontinuities**” was conducted under the supervision of **Dr. Muhammad Afzal**. No part of this thesis has been submitted anywhere else for any other degree. This thesis is submitted to the **Department of Mathematics, Capital University of Science and Technology** in partial fulfillment of the requirements for the degree of Doctor in Philosophy in the field of **Mathematics**. The open defence of the thesis was conducted on **August 17, 2022**.

Student Name : Touqeer Nawaz (DMT-151002)

The Examining Committee unanimously agrees to award PhD degree in the mentioned field.

Examination Committee :

- (a) External Examiner 1: Dr. Mehmood ul Hassan
Professor
COMSATS University, Islamabad
- (b) External Examiner 2: Dr. Amjad Hussain
Associate Professor
QAU, Islamabad
- (c) Internal Examiner : Dr. Muhammad Sagheer
Professor
CUST, Islamabad

Supervisor Name : Dr. Muhammad Afzal
Associate Professor
CUST, Islamabad

Name of HoD : Dr. Muhammad Sagheer
Professor
CUST, Islamabad

Name of Dean : Dr. Muhammad Abdul Qadir
Professor
CUST, Islamabad

AUTHOR'S DECLARATION

I, **Touqeer Nawaz (Registration No. DMT-151002)**, hereby state that my PhD thesis entitled, '**Scattering Analysis in Bifurcated and Trifurcated Waveguides Involving Structural Discontinuities**' is my own work and has not been submitted previously by me for taking any degree from Capital University of Science and Technology, Islamabad or anywhere else in the country/ world.

At any time, if my statement is found to be incorrect even after my graduation, the University has the right to withdraw my PhD Degree.



(Touqeer Nawaz)

Dated: **17** August, 2022

Registration No : DMT-151002

PLAGIARISM UNDERTAKING

I solemnly declare that research work presented in the thesis titled “**Scattering Analysis in Bifurcated and Trifurcated Waveguides Involving Structural Discontinuities**” is solely my research work with no significant contribution from any other person. Small contribution/ help wherever taken has been duly acknowledged and that complete thesis has been written by me.

I understand the zero tolerance policy of the HEC and Capital University of Science and Technology towards plagiarism. Therefore, I as an author of the above titled thesis declare that no portion of my thesis has been plagiarized and any material used as reference is properly referred/ cited.

I undertake that if I am found guilty of any formal plagiarism in the above titled thesis even after award of PhD Degree, the University reserves the right to withdraw/ revoke my PhD degree and that HEC and the University have the right to publish my name on the HEC/ University Website on which names of students are placed who submitted plagiarized thesis.



(**Touqeer Nawaz**)

Dated: *17* August, 2022

Registration No : DMT-151002

List of Publications

It is certified that following publication(s) have been made out of the research work that has been carried out for this thesis:-

1. **T. Nawaz**, M. Afzal, and R. Nawaz, “The scattering analysis of trifurcated waveguide involving structural discontinuities”, *Advances in Mechanical Engineering*, vol. 11, no. 7, pp. 1–10, 2019.
2. **T. Nawaz**, M. Afzal, and R. Nawaz, “Study of generalized planar trifurcated lined duct involving step-discontinuities and change in material properties”, Submitted to *Waves in Random and Complex Media*, 2021.
3. M. Afzal, **T. Nawaz**, and R. Nawaz, “Scattering characteristics of planar trifurcated waveguide structure containing finite discontinuities”, *Waves in Random and Complex Media*, pp. 1–20, 2020.
4. **T. Nawaz**, M. Afzal, and A. Wahab, “Scattering analysis of a flexible trifurcated lined waveguide structure with step-discontinuities”, *Physica Scripta*, vol. 96, no. 11, 115004, 2021.

(Touqeer Nawaz)

Registration No: DMT 151002

Acknowledgement

“Glory be to you, we have no knowledge except what you have taught us. Verily, it is You, the All-Knower, the All-Wise O’All-Knowing, grant me knowledge” (AL-QURAN).

First and foremost, I would like to thank Allah almighty for giving me the pui-sance, knowledge, competence, and opportunity to undertake this research study and to get it out and complete it satisfactorily. Without his benison, this achievement would not have been attainable. I had not enough wisdom and strength to conquer this milepost. It is one of His infinite benedictions that He bestowed upon me with the potential and ability to complete the present research.

I wish to show my gratitude to all the people whose abetment was a milestone in the completion of this project, especially my righteous supervisor Dr. Muhammad Afzal, for his priceless suggestions, constant support, great patience, and encouragement. I wish to express my sincere thank you to the head of department Dr. Muhammad Sagheer, for the valuable guidance and encouragement extended to me. I would like to thanks Capital University Of Science And Technology, Islamabad, Pakistan, for providing a suitable environment for research. I express my thankful feelings to Dr. Rab Nawaz for his constructive suggestions during my research time. I would also appreciate the positive concern of my all research fellows, who supported me at the time of stress when I was about to lose my heart.

Of course, at this stage, I cannot forget my whole family especially my beloved father, mother, my brothers, my sisters, sister-in-law for their prayers, continuous support, and love. Their prayers have lightened up my spirit to finish this thesis. Special thanks to my wife who encouraged me throughout to complete my degree. I would like to express my love and affection to my daughters Nisma Touqeer and Hamna Touqeer for being such good girls always cheering me up.

(Touqeer Nawaz)

Abstract

This dissertation focuses on a class of boundary value problems modeling scattering phenomena in bifurcated and trifurcated waveguides involving structural discontinuities. The study is important because of its applications in active noise control measures, especially used to control the low frequency noise and related vibrations. The physical problems are modeled to illustrate the scattering behavior of acoustic waves in the planar as well as flexible waveguides comprised of thin elastic elements with structural discontinuities along edges. The resulting problems are governed by Helmholtz's equation together with Dirichlet, Neumann, Robin, and/or higher-order boundary conditions. The Mode-Matching (MM) scheme is adopted to solve the governing boundary value problems. The solution is developed for the analysis of symmetric, uniform and non-uniform cross sections. The eigenvalue problems associated with rigid, soft, or impedance type boundary conditions fall into the Sturm-Liouville (SL) category and the eigenfunctions happen to be orthogonal. However, when higher-order boundary conditions are involved, the eigenfunctions are no more orthogonal and the resulting eigen-sub-systems turns out to be non-Sturm-Liouville. It makes the use of generalized orthogonal characteristics indispensable to guarantee the pointwise convergence of the solution. In the process of converting differential systems to linear algebraic systems, orthogonal characteristics are taken into account. Additional constants that are found through the application of appropriate edge conditions are governed by the application of the generalised orthogonality relation (OR). To describe physical attributes of the modelled structures, the systems are truncated and inverted. By analyzing the numerical solutions, we discuss the transmission of acoustic waves traveling through the prototype waveguide geometries and study the behavior of the radiated energy versus the variations of the geometric discontinuities, material contrasts, and bounding properties. It is worth mentioning that underlying structures are closely related with silencer geometries in practical context.

Contents

Author's Declaration	v
Plagiarism Undertaking	vi
List of Publications	vii
Acknowledgement	viii
Abstract	ix
List of Figures	xiii
List of Tables	xvii
Abbreviations	xviii
Symbols	xix
1 Introduction	1
1.1 Avant-garde	7
1.2 Dissertation Outline	8
2 Preliminaries	10
2.1 Physical Context	10
2.2 Boundary Conditions	13
2.2.1 Impedance Condition	14
2.2.2 Elastic Membrane Condition	15
2.3 Mathematical Formulation	17
2.3.1 Dimensional Setting	17
2.3.2 Non-dimensional Setting	18
2.3.3 Mode-matching Formulation	19
2.4 Canonical Problem	26
2.4.1 Mathematical Formulation	26
2.4.2 Eigenfunction Expansions	29
2.4.3 Mode-matching Solution	32

2.4.4	Energy Balance	34
2.4.5	Numerical Results and Discussions	35
3	Trifurcated Waveguide Scattering Analysis with Structural Discontinuities	47
3.1	Mathematical Formulation	47
3.2	Mode-matching Solution	50
3.3	Energy Balance	56
3.4	Numerical Results and Discussions	57
4	Study of Generalized Planar Trifurcated Lined Duct Involving Structural Discontinuities	65
4.1	Mathematical Formulation	65
4.2	Mode-matching Solution	67
4.3	Energy Balance	72
4.4	Numerical Results and Discussions	74
5	Scattering Attributes of Planar Trifurcated Waveguide Structure with Finite Discontinuities	86
5.1	Mathematical Formulation	87
5.2	Mode-matching Solution	88
5.3	Energy Balance	97
5.4	Numerical Results and Discussions	98
6	Analysis of Scattering in a Flexible Trifurcated Lined Waveguide with Step Discontinuities	115
6.1	Mathematical Formulation	116
6.1.1	Geometric Configuration	116
6.1.2	Governing Equations	117
6.1.3	Traveling Wave Formulations	119
6.1.3.1	Regions \mathcal{R}_1^\pm	119
6.1.3.2	Regions \mathcal{R}_2^\pm	120
6.1.3.3	Regions \mathcal{R}_3^\pm	121
6.1.3.4	Region \mathcal{R}_4	122
6.2	Mode-matching Solution	123
6.2.1	Matching Conditions at $x = -L$	123
6.2.2	Matching Conditions at $x = L$	126
6.2.3	Energy Balance	128
6.3	Numerical Investigation and Discussion	130
6.3.1	Validation of the Mode-matching Scheme	130
6.3.2	Analysis of Reflected and Absorbed Powers	133
6.3.2.1	Influence of Reactance on Power	134
6.3.2.2	Influence of Resistance on Power	143
7	Conclusions and Future Recommendations	145

7.1	Conclusions	145
7.2	Future Recommendations	149
	Bibliography	150

List of Figures

2.1	Geometry of the proposed model.	27
2.2	Reflected energy (\mathcal{E}_1) versus frequency (f) with RR conditions in \mathcal{R}_1 and \mathcal{R}_2 , and RI , RR and RS conditions in \mathcal{R}_3 (a) with step-discontinuous ($a \neq b$) (b) without step-discontinuous ($a = b$), where $\bar{a} = 0.24m$, $\bar{b} = 3\bar{a}$ and $N = 10$	37
2.3	Reflected energy (\mathcal{E}_2) versus frequency (f) with RR conditions in \mathcal{R}_1 and \mathcal{R}_2 , and RI , RR and RS conditions in \mathcal{R}_3 (a) with step-discontinuous ($a \neq b$) (b) without step-discontinuous ($a = b$), where $\bar{a} = 0.24m$, $\bar{b} = 3\bar{a}$ and $N = 10$	39
2.4	Transmitted energy (\mathcal{E}_3) versus frequency (f) with RR conditions in \mathcal{R}_1 and \mathcal{R}_2 , and RI , RR and RS conditions in \mathcal{R}_3 (a) with step-discontinuous ($a \neq b$) (b) without step-discontinuous ($a = b$), where $\bar{a} = 0.24m$, $\bar{b} = 3\bar{a}$ and $N = 10$	40
2.5	The real (a) and imaginary (b) parts of pressures against duct heights, at interface, with step-discontinuities and rigid-impedance boundaries, where, $\bar{a} = 0.24m$, $\bar{b} = 3\bar{a}$ and $N = 80$	41
2.6	The real (a) and imaginary (b) parts of normal velocities against duct heights, at interface, with step-discontinuities and RI boundaries, where, $\bar{a} = 0.24m$, $\bar{b} = 3\bar{a}$ and $N = 80$	42
3.1	Geometry of the proposed model.	48
3.2	The energy flux/power components against frequency in discontinuous waveguide, with (a) rigid-rigid (b) rigid-soft boundaries, where, $\bar{a} = 0.05m$, $\bar{b} = 0.1m$, $\bar{h} = 0.15m$ and $N = 10$	58
3.3	The energy flux/power components against frequency in planer waveguide, with (a) rigid-rigid (b) rigid-soft boundaries, where, $\bar{a} = 0.05m$, $\bar{b} = 0.1m$, $\bar{h} = 0.15m$ and $N = 10$	59
3.4	The energy flux/power components against height discontinuities h , for (a) rigid-rigid (b) rigid-soft boundaries, where, $\bar{a} = 0.05m$, $\bar{b} = 0.1m$ and $N = 10$	60
3.5	The energy flux/power components against b , for (a) rigid-rigid (b) rigid-soft boundaries, where, $\bar{a} = 0.05m$, $\bar{h} = \bar{b}$ and $N = 10$	61
3.6	The real (a) and imaginary (b) parts of pressures against duct heights, at interface, with step-discontinuities and rigid-rigid boundaries, where, $\bar{a} = 0.05m$, $\bar{b} = 0.1m$, $\bar{h} = 0.15m$ and $N = 80$	62

3.7	The real (a) and imaginary (b) parts of normal velocities against duct heights, at interface, with step-discontinuities and rigid-rigid boundaries, where, $\bar{a} = 0.05m$, $\bar{b} = 0.1m$, $\bar{h} = 0.15m$ and $N = 80$.	63
3.8	The scattering energies plotted against number of terms N for discontinuous structure where $\bar{a} = 0.05m$, $\bar{b} = 0.1m$, $\bar{h} = 0.15m$ and $f = 530Hz$.	64
4.1	The geometry of the problem	67
4.2	Reflected energy in region $\mathcal{R}_1(\mathcal{E}_1)$ versus frequency (f) for Hard, Soft and Impedance outer bounding walls (a) with step-discontinuous ($b \neq h$) (b) without step-discontinuous ($b = h$) where $\bar{a} = 0.24m$, $\bar{b} = 3\bar{a}$ and $N = 10$.	75
4.3	Reflected energy in region $\mathcal{R}_1(\mathcal{E}_1)$ versus frequency (f) for Hard, Soft and Impedance outer bounding walls (a) with step-discontinuous ($b \neq h$) (b) without step-discontinuous ($b = h$) where $\bar{a} = 0.24m$, $\bar{b} = \frac{3\bar{a}}{2}$ and $N = 10$.	76
4.4	Reflected energy in region $\mathcal{R}_1(\mathcal{E}_1)$ versus $k \times \bar{a}$ for Hard, Soft and Impedance outer bounding walls (a) with step-discontinuous ($b \neq h$) (b) without step-discontinuous ($b = h$) where, $f = 230Hz$, $\bar{b} = 3\bar{a}$ and $N = 10$.	77
4.5	Reflected energy in region $\mathcal{R}_1(\mathcal{E}_1)$ versus $k \times \bar{a}$ for Hard, Soft and Impedance outer bounding walls (a) with step-discontinuous ($b \neq h$) (b) without step-discontinuous ($b = h$) where, $f = 230Hz$, $\bar{b} = \frac{3\bar{a}}{2}$ and $N = 10$.	78
4.6	The reflected flux/power components against frequency containing compressible fluid in (a) discontinuous (b) continuous waveguides for $\bar{a} = 0.24m$, $\bar{b} = 3\bar{a}$, $\xi = 0.5$, $p = r = 1$, $q = s = i\zeta$ and $N = 10$.	79
4.7	The reflected flux/power components against $k \times \bar{a}$ containing compressible fluid in (a) discontinuous (b) continuous waveguides for $f = 230Hz$, $\bar{b} = 3\bar{a}$, $\xi = 0.5$, $p = r = 1$, $q = s = i\zeta$ and $N = 10$.	80
4.8	The radiated energy flux/power components against frequency containing compressible fluid in discontinuous waveguide for (a) $\bar{b} = 3\bar{a}$ (b) $\bar{b} = \frac{3\bar{a}}{2}$, $\bar{a} = 0.24m$, $p = q = r = s = 1$ and $N = 10$.	81
4.9	The radiated energy flux/power components against $k \times \bar{a}$ containing compressible fluid in discontinuous waveguide for (a) $\bar{b} = 3\bar{a}$ (b) $\bar{b} = \frac{3\bar{a}}{2}$, $\bar{a} = 0.24m$, $p = q = r = s = 1$ and $N = 10$.	82
4.10	The real (a) and imaginary (b) parts of pressure at interface for $\bar{a} = 0.24m$, $\bar{b} = 3\bar{a}$, $\bar{h} = 5\bar{a}$, $\mu = \kappa = 1$ and $N = 120$.	83
4.11	The real (a) and imaginary (b) parts of normal velocity at interface for $\bar{a} = 0.24m$, $\bar{b} = 3\bar{a}$, $\bar{h} = 5\bar{a}$, $\mu = \kappa = 1$ and $N = 120$.	84
4.12	The scattering energies plotted against number of terms N for discontinuous structure where $\bar{a} = 0.24m$, $\bar{b} = 3\bar{a}$, $\bar{h} = 5\bar{a}$ and $f = 530Hz$.	85

5.1	The geometry of the problem	87
5.2	Radiated energy versus frequency (f) for all Robin type (mixed) bounding walls (a) with step-discontinuity ($b \neq h$) (b) without step-discontinuity ($b = h$) where $\bar{a} = 0.24m, \bar{b} = 3\bar{a}, p = q = r = s = \mu = \kappa = 1$ and $N = 10$	99
5.3	Radiated energy versus ($k \times \bar{a}$) for all Robin type (mixed) bounding walls (a) with step-discontinuity ($b \neq h$) (b) without step-discontinuity ($b = h$) where $\bar{a} = 0.24m, \bar{b} = 3\bar{a}, p = q = r = s = \mu = \kappa = 1$ and $N = 10$	101
5.4	The reflected energy versus frequency (f) containing compressible fluid (a) with step-discontinuity ($b \neq h$) (b) without step-discontinuity ($b = h$), when all the outer boundaries are Impedance, Rigid and Soft respectively, for $\bar{a} = 0.24m, \bar{b} = 3\bar{a}, \bar{h} = 5\bar{a}$ and $N = 10$	105
5.5	The reflected energy versus ($k \times \bar{a}$) containing compressible fluid (a) with step-discontinuity ($b \neq h$) (b) without step-discontinuity ($b = h$), when all the outer boundaries are Impedance, Rigid and Soft respectively, for $\bar{a} = 0.24m, \bar{b} = 3\bar{a}, \bar{h} = 5\bar{a}$ and $N = 10$	107
5.6	The reflected flux/power components against frequency containing compressible fluid in (a) discontinuous (b) continuous waveguides for $\bar{a} = 0.24m, \bar{b} = 3\bar{a}, \xi = 0.5, p = r = 1, q = s = i\zeta$ and $N = 10$	108
5.7	The reflected flux/power components against frequency containing compressible fluid in (a) discontinuous (b) continuous waveguides for $\bar{a} = 0.24m, \bar{b} = 3\bar{a}, \xi = 1, p = r = 1, q = s = i\zeta$ and $N = 10$	109
5.8	The real (a) and imaginary (b) parts of pressure at $x = -L$, for $\bar{a} = 0.24m, \bar{b} = 3\bar{a}, \bar{h} = 5\bar{a}, p = q = r = s = \mu = \kappa = 1$ and $N = 20$	110
5.9	The real (a) and imaginary (b) parts of normal velocity at $x = -L$, for $\bar{a} = 0.24m, \bar{b} = 3\bar{a}, \bar{h} = 5\bar{a}, p = q = r = s = \mu = \kappa = 1$ and $N = 20$	111
5.10	The real (a) and imaginary (b) parts of pressure at $x = L$, for $\bar{a} = 0.24m, \bar{b} = 3\bar{a}, \bar{h} = 5\bar{a}, p = q = r = s = \mu = \kappa = 1$ and $N = 20$	112
5.11	The real (a) and imaginary (b) parts of normal velocity at $x = L$, for $\bar{a} = 0.24m, \bar{b} = 3\bar{a}, \bar{h} = 5\bar{a}, p = q = r = s = \mu = \kappa = 1$ and $N = 20$	113
5.12	The scattering energies plotted against number of terms N for discontinuous structure where $\bar{a} = 0.24m, \bar{b} = 3\bar{a}, \bar{h} = 5\bar{a}, \bar{L} = 0.25m$, and $f = 530Hz$	114
6.1	The geometry of the problem	117
6.2	The real and imaginary components of the pressure at $x = -L$ when $\bar{a} = 0.05m, \bar{b} = 0.1m, \chi = 0.5 + 0.5i, \bar{h} = 0.15m$, and $f = 350Hz$	131
6.3	The real and imaginary components of the pressure at $x = L$ when $\bar{a} = 0.05m, \bar{b} = 0.1m, \chi = 0.5 + 0.5i, \bar{h} = 0.15m$, and $f = 350Hz$	132
6.4	The real and imaginary components of the normal velocity at $x = -L$ when $\bar{a} = 0.05m, \bar{b} = 0.1m, \chi = 0.5 + 0.5i, \bar{h} = 0.15m$, and $f = 350Hz$	133

6.5	The real and imaginary components of the normal velocity at $x = L$ when $\bar{a} = 0.05m$, $\bar{b} = 0.1m$, $\chi = 0.5 + 0.5i$, $\bar{h} = 0.15m$, and $f = 350Hz$	134
6.6	Energy versus frequency with fibrous lining along the walls of the expansion chamber when $\bar{a} = 0.05m$, $\bar{b} = 0.1m$, and $N = 10$	135
6.7	Energy versus frequency with fibrous lining along the walls of the expansion chamber when $\bar{a} = 0.05m$, $\bar{b} = 0.1m$, and $N = 10$	136
6.8	Energy versus duct height ($k \times \bar{a}$) with fibrous lining along the walls of the expansion chamber when $f = 1000Hz$, $\bar{b} = 0.1m$, and $N = 10$	137
6.9	Energy versus duct height ($k \times \bar{a}$) with fibrous lining along the walls of the expansion chamber when $f = 1000Hz$, $\bar{b} = 0.1m$, and $N = 10$	138
6.10	Energy versus frequency with perforated lining along the walls of the expansion chamber when $\bar{a} = 0.05m$, $\bar{b} = 0.1m$, and $N = 10$	139
6.11	Energy versus frequency with perforated lining along the walls of the expansion chamber when $\bar{a} = 0.05m$, $\bar{b} = 0.1m$, and $N = 10$	140
6.12	Energy versus duct height ($k \times \bar{a}$) with perforated lining along the walls of the expansion chamber when $f = 1000Hz$, $\bar{b} = 0.1m$, and $N = 10$	141
6.13	Energy versus duct height ($k \times \bar{a}$) with perforated lining along the walls of the expansion chamber when $f = 1000Hz$, $\bar{b} = 0.1m$, and $N = 10$	142

List of Tables

2.1	Propagating modes of regions \mathcal{R}_j , $j = 1, 2, 3 \dots$ for discontinuous waveguides	38
2.2	Propagating modes of regions \mathcal{R}_j , $j = 1, 2, 3 \dots$ for planar waveguides	38
2.3	Discontinuous bifurcated waveguide for RI case, when $\bar{a} = 0.24m$ and $\bar{b} = 3\bar{a}$ by varying frequency	43
2.4	Continuous bifurcated waveguide for RI case, when $\bar{a} = \bar{b} = 0.24m$ by varying frequency	44
2.5	Discontinuous bifurcated waveguide for RR case, when $\bar{a} = 0.24m$ and $\bar{b} = 3\bar{a}$ by varying frequency	45
2.6	Continuous bifurcated waveguide for RR case, when $\bar{a} = \bar{b} = 0.24m$ by varying frequency	45
2.7	Discontinuous bifurcated waveguide for RS case, when $\bar{a} = 0.24m$ and $\bar{b} = 3\bar{a}$ by varying frequency	46
2.8	Continuous bifurcated waveguide for RS case, when $\bar{a} = \bar{b} = 0.24m$ by varying frequency	46
5.1	Discontinuous trifurcated waveguide, when $\bar{a} = 0.24m$, $\bar{b} = 3\bar{a}$, $\bar{h} = 5\bar{a}$, $p = q = r = s = \mu = \kappa = 1$ and $\bar{L} = 0.25m$ by varying frequency.	103
5.2	Planar trifurcated waveguide, when $\bar{a} = 0.24m$, $\bar{b} = \bar{h} = 3\bar{a}$, $p = q = r = s = \mu = \kappa = 1$ and $\bar{L} = 0.25m$ by varying frequency.	103
5.3	Discontinuous trifurcated waveguide, when $f = 230Hz$, $\bar{b} = 3\bar{a}$, $\bar{h} = 5\bar{a}$, $p = q = r = s = \mu = \kappa = 1$ and $\bar{L} = 0.25m$ by varying height ($k \times \bar{a}$).	104
5.4	Planar trifurcated waveguide, when $f = 230Hz$, $\bar{b} = \bar{h} = 3\bar{a}$, $p = q = r = s = \mu = \kappa = 1$ and $\bar{L} = 0.25m$ by varying height ($k \times \bar{a}$).	104

Abbreviations

HVAC	Heating Ventilation and Air-Conditioning
MM	Mode-Matching
OR	Orthogonality Relation
RR	Rigid-Rigid
RI	Rigid-Impedance
RS	Rigid-Soft
SL	Sturum Liouville
STP	Standard Temperature Pressure
WH	Wiener-Hopf

Symbols

p'	Acoustic pressure
ρ_0	Density in equilibrium state
\mathbf{u}	Velocity vector
f	Frequency
ω	Angular frequency
c	Speed of sound
k	Wave number
\hat{n}	Unit normal vector
δ_{mn}	Kronecker delta
N	Truncation number
$W(x, y, t)$	Membrane displacement
c_m	Speed of sound on membrane
ρ_m	Mass density
\mathcal{P}_{inc}	Power incident
μ	Membrane wavenumber in <i>vacuo</i>
α	Membrane fluid loading parameter
t	Time
N	Truncation number
ψ_{inc}	Incident scalar field potential
ψ_{ref}	Reflected scalar field potential
ψ_{tran}	Transmitted scalar field potential
Z	Specific impedance in dimensionless form
ς	Specific impedance in dimensionless form

Chapter 1

Introduction

The theory of noise reduction has become a dynamic area of research because of industrial advancements at a large scale. This study is essential regarding exhaust systems, steam valves, vehicles, turbofan engines, ducts, and pipes. Generally, the guided wave systems are more efficient carriers of acoustic energy curtailing lateral diffusion that ultimately resists decaying sound waves according to *inverse square law*. The remarkable interest in the field is thriving due to the necessity to plane and defined structures in which underlying vibrations and the transmission of related noise can be controlled. One type of noise, for instance, is wave scattering at a discontinuity in an object's or structure's material properties.

Over the years, a range of interesting and challenging problems that involve wave scattering analysis in bifurcated and trifurcated waveguide channels have been discussed by many researchers. The interest to minimize the noise pollution impending from the heating ventilation and air conditioning (HVAC) system of structures or automotive exhaust systems of vehicles or aircraft has stipulated the continued interest. The dissipative silencers containing complex geometrical shapes and bulk reacting materials have been modeled to attenuate the broad-band noise. To incorporate these theoretical models, several analytical and numerical techniques have been established thus far. The objective of these experiments is to see how different channel designs and material properties affect sound attenuation in numerous contexts. [1–4].

Many authors have studied how to reduce unwanted noise by aligning walls in a parallel plate configuration and using rigid, soft, or impedance-type boundary features. For example, the studies [5–8] include the acoustic scattering in planar trifurcated waveguides containing rigid, soft, or porous lining along with stationary and moving compressible fluid medium. The duct segments in all of these cases have constant geometrical and physical features, so the single field model is still appropriate.

The Wiener-Hopf (WH) solution is obtained by using integral formulations in the Fourier domain. Unfortunately, the WH approach is ineffective for more complex geometrical and physical features when the wavenumber spectrum in the waveguide is not continuous. Many researchers contributed to the study of acoustic wave diffraction in a planar trifurcated waveguide with various bounding characteristics; see, for example, [9–12]. Despite these achievements, no attempt has been made to investigate trifurcated waveguides in more practical scenarios by taking step discontinuities into account. The classical WH technique fails to provide scattered fields for such ducting systems. However, so-called mode-matching (MM) techniques have proven to be extremely beneficial for situations involving more complex geometries, as well as a variety of media and material properties.

These methods were initially designed to manage canonical problems represented by Laplace or Helmholtz equations and the ducts or channel boundaries described by Dirichlet, Neumann, or Robin boundary conditions. Matching modes are widely used to identify the reflection and transmission of waves across interfaces at discontinuities in pipes and ducts; see, for example, [13–16].

The key challenge is to deal with geometric discontinuities at duct segment plane connections (junctions). Even while it has generally been possible to investigate at a simple non-uniform geometry with modest dimensions, the study of acoustic radiation from structural discontinuities goes back to Rayleigh[17].

However, Bostrom [18] and Miles [19], and more recently, Nawaz and Lawrie [20] and Nawaz et al. [21], discussed the sound scattering from structural discontinuities together with obstacles at a finite junction. To match the scattering modes,

continuity conditions of pressures and normal velocities at aperture are applied. In normal velocity fields, geometric discontinuities are observed, and various modes are allowed to propagate.

Many scientists and engineers addressed the issue of noise reduction by considering different material properties of ducts together with diverse geometrical designs. Rawlins [22] was among the first ones who discussed noise reduction through a duct having a thin acoustical absorbent lining.

Demir and Buyukaksoy [23] noted that covering a duct's walls with acoustically absorbent material can considerably increase the duct's acoustic performance. Morse [24] investigated the attenuation of sound in infinite closed ducts using acoustically absorbent liners. Later, it is confirmed through experiments that lining a waveguide with an acoustically absorbent material creates an additional sound absorption.

Jones [25] addressed the problem of scattering of plane waves from three parallel soft semi-infinite and equidistant plates and computed the far-field and near-zone solutions. Later, Asghar et al. [26] extended Jones' analysis for the case of a line source and a point source scattering in still air when the medium is convective. On the other hand, the studies [27–30] dealt with the acoustic scattering in planar trifurcated waveguides containing rigid, soft, or porous linings together with stationary and moving compressible fluid medium. In all such cases, the wavenumber observed a continuous spectrum and thus, the use of Fourier transform remained suitable.

The wave scattering of bifurcated and trifurcated waveguide structures is a subject of great interest for many researchers. The primary goal is to control the noise emanated from different unwanted sources placed in large industrial zones. The dissipative silencers containing complex geometrical shapes and bulk reacting materials have been modeled to attenuate the broad-band noise. To date, a variety of analytical and numerical techniques have been used to investigate different theoretical models. The major goal of these investigations was to look into the sound attenuation region in relation to various channel designs and material properties

The design of the geometry of the expansion chamber is imperative in reducing noise levels in mechanical systems such as ducts, pipes, and compressors. Selamat and Radavich [33] studied the effect of chamber length on the non-planar wave propagation in concentric expansion chambers. Selamat and Ji [34] discussed the acoustical attenuation performances of circular expansion chamber silencers with an extended inlet and outlet and a circular dual-chamber silencer. They observed that, as the length of the chamber increases, the number of domes increases but remains the same as the simple expansion chambers. Similarly, as the length of the extended ducts is increased, the number of resonant peaks increases, and the resonant frequencies decrease.

Abom [35] studied the effects of higher-order modes to evaluate the acoustical performance of an expansion chamber with an extended inlet and outlet. Bouykoksi and Polat [36] utilized the WH approach immersed with MM analysis to discuss the acoustic scattering in a bifurcated waveguide with rigid/soft boundary conditions. Rawlins [37] proved that by using acoustically absorbent linings, the unwanted noise within a waveguide can be reduced. He discussed that the acoustic performance of a duct can be increased by lining its walls with acoustically absorbent material.

Huang [38] developed the so-called plate silencers with side-branch cavities covered by flexible plates, which give rise to noise attenuation through wave reflection towards the upstream. The work was later on extended to sandwich plates to facilitate practical implementations [39]. Afterwards, Lapin [40] examined the sound attenuation and presented fundamental relations in the analysis of the propagation of acoustic waves in waveguides with liners, moving filler media, and reflectors.

Recent studies include the acoustic scattering in two planar trifurcated waveguides comprised of an expansion chamber containing rigid, soft, or porous lining together with stationary and moving compressible fluid medium. The well-known WH technique has been used to solve most canonical problems. However, the complication of such underlying structures created essential difficulties in the application of the WH technique.

Numerous authors contributed to the study of acoustic wave diffraction in planar trifurcated waveguides with different boundary conditions. Yet, no attempt has been made to analyze trifurcated waveguides in more practical contexts by considering expansion chambers with multiple step-discontinuities. It is important to mention that diffraction in waveguides, with different combinations of the boundary conditions with and without structural discontinuities, is the topic of current interest [41–44].

The study of the impacts of unwanted noise has been an active area of research because of its technological importance. This study is significant regarding exhaust systems, steam valves, internal combustion engines of aircraft and vehicles, ducts, and pipes. The analysis of wave scattering by different structures is an important area of noise reduction. Specifically, Rawlins [45, 46] took the lead and showed that a duct with a thin acoustically absorbent lining is an effective method that can be utilized to reduce the unwanted noise inside a waveguide.

Koch [47] discussed the analytical solution of the problem of sound radiation from the open end of a semi-infinite two-dimensional duct that is lined on inner side walls with a locally reacting sound-absorbing material of finite length. The problem was tackled analytically with the assistance of the WH technique. The acquired analytical outcomes were also discussed numerically for several parameters involved.

Different physical models and theories are available in the literature to study the mechanism of wave propagation. The envisaged boundary value problems are governed usually by Helmholtz and Laplace type differential equations together with rigid, soft, or impedance type boundary conditions. A range of such boundary value problems has been addressed by using the WH technique.

Keller [48] depicted the mathematical hypothesis of diffraction in the high-frequency limit that provides the complete sound field at any time in space as the sum of all the scattered waves. He considered a wide range of issues that are canonical to the diffraction hypothesis. Noble [49] explained the WH technique in detail to demonstrate that this method is an amazing and adaptable apparatus. He

gave analytical solutions to a variety of issues including the scattering of sound waves from the edges or sharp discontinuities. Candel [50] explored the radiation of acoustic modes from the end of a duct submerged in a consistently moving medium by applying the WH technique. Brazier-Smith [51] addressed a complex geometry comprising of two co-planar semi-infinite plates of different thicknesses that are joined along one edge. He obtained solutions in various cases by applying the WH technique. Lining a duct with sound-absorbing material, mostly porous, has been very common and often the most reliable engineering solution. For chemical or other reasons, the use of a porous material is not desirable within the exhaust gas, alternative sound-absorbing structures are used [52].

Huang and Choy [53] investigated the propagation of sound in a flexible duct theoretically and experimentally. They performed the experiment on a duct with a finite section of tense membrane and compared the propagating modes with the relevant modes of the infinite membrane model.

Lawrie and Abraham [54] discussed the generalized orthogonal properties of the boundary value problems involving higher-order boundary conditions. They applied the proposed scheme on prototype problems to explain acoustic scattering in membrane-bounded ducts. Wang [55] analyzed a single-pass perforated absorbing silencer by using a one-dimensional decoupling approach to account for the acoustic characteristics of absorbing material.

Delany and Bazley [56] suggested empirical expressions for the characteristic impedance and wave number for fibrous absorbing material as a function of frequency and flow resistance. They also found that the flow resistance is determined by fiber size and bulk density. The characteristic impedance and wave number estimated by the transfer matrix method agree with the empirical expressions of Delany and Bazley. Recently, Peake and Abraham [57] presented the WH solution for the radiation properties of a pair of semi-infinite, parallel-plate ducts in which the inner duct is buried inside the outer duct.

The sudden changes in geometry and/or material properties greatly affect the scattering energies. For example, the acoustic configuration including the porous

coating of walls and/or the abrupt geometric changes in bounding surfaces are useful to optimize the noise transmission. Likewise, the silencer cavities reduce the noise produced by an auto exhaust system thanks to the cavity resonance mechanism. In the situations wherein the physical problems contain geometric discontinuities and/or more complex bounding properties, the use of the WH technique is inappropriate. Thus, a new technique is required that may handle more complicated physical situations together with mathematical ease. Recently, the MM approach has been adopted to solve more complex geometries with different material properties. Warren et al. [58] applied the MM technique to analyze the acoustic scattering from step-discontinuity in the membrane-bounded waveguides.

The main purpose of this research is by using a hybrid matching scheme to analyse acoustics scattering in non-uniform and/or uniform trifurcated waveguides with compressible fluid in the duct sections with various bounding wall conditions. The modal field representation is formulated for the duct region with constant physical and geometrical characteristics.

In this dissertation, the MM scheme is explored to solve a trifurcated waveguide problem involving geometric discontinuities. The inside of the waveguide regions contains compressible fluid with different bounding wall conditions. It is worth mentioning that Hassan [59] and Hassan et al. [60, 61] applied the MM technique to discuss the acoustic scattering in planar trifurcated and pentafurcated waveguides containing compressible fluid in the absence of step-discontinuities.

1.1 Avant-garde

The current study illustrates the MM analysis of acoustic scattering and attenuation through planar and flexible waveguides having different material properties and structural discontinuities. The work is a continuation in the direction of previous studies [15, 16, 20, 21] and addresses the following problems.

1. Trifurcated waveguide scattering analysis with structural discontinuities.

2. Study of generalized planar trifurcated lined duct involving structural discontinuities.
3. Scattering attributes of planar trifurcated waveguide structure with finite discontinuities.
4. Analysis of scattering in a flexible trifurcated lined waveguide with step discontinuities.

1.2 Dissertation Outline

The outlines of the dissertation are as follows:

CHAPTER 2 provides some fundamental concepts and preliminaries that are useful for understanding the mathematical modeling of physical problems and the solution schemes.

CHAPTER 3 presents the problem involving scattering analysis of a trifurcated waveguide involving structural discontinuities. The bounding wall conditions are assumed to be both soft/rigid and the MM solution is explained.

The study of generalized planar trifurcated lined duct involving structural discontinuities is conducted in CHAPTER 4. We investigate the scattering characteristics of a trifurcated lined duct in a general context. A semi-infinite duct is symmetrically situated inside an infinite acoustic lined duct having step-discontinuities and generalized mixed boundaries. The scattered field potentials in each region are computed using the MM approach. The influence of structural discontinuities, duct size, and physical parameters on the energy of the scattered fields is studied. The currently available results for trifurcated waveguides can be recovered as special cases.

The scattering properties of a planar trifurcated waveguide structure with several discontinuities are studied in CHAPTER 5. The analysis of a planar trifurcated lined waveguide backed by a line walled cavity with several step discontinuities

is the subject of this chapter. On the x -axis, the duct arrangement is assumed to be symmetric. The study of the behaviour of distributed fields in different duct areas subject to different material properties of the walled duct is the key emphasis. The governing problem is reduced to a Sturm-Liouville (SL) eigenvalue problem, which can be solved using the conventional mode-matching approach. The scattering pattern is observed in perforated and fibrous materials, allowing for the analysis of noise effects for various underlying structures. It's worth noting that, in practice, fundamental structures are directly related to silencer geometries.

In CHAPTER 6, we present the analysis of scattering in a flexible trifurcated lined waveguide with step discontinuities. The inner walls of the chamber are coated with an acoustically absorbent lining, while the other sides are left flexible. Edge conditions are also applied to define the physical behaviour of elastic membranes at finite edges. A semi-infinite duct is symmetrically placed within an infinite acoustic lined duct with step-discontinuities and generalised mixed boundaries, which is linked to an expansion chamber. The scattered field potentials in each region are computed using the MM approach and the influence of pertinent parameters and characteristics on the energy distribution within the waveguide are discussed.

Finally, a brief summary, concluding remarks, and directions for the future work are presented in CHAPTER 7.

Chapter 2

Preliminaries

This chapter contains details of some fundamental concepts and preliminaries that are useful in understanding the physical and mathematical context of the problems undertaken in this dissertation. Helmholtz's equation governs the boundary value problem problems, which involve rigid, soft, impedance, and/or membrane types of boundary conditions. These boundary value problems are solved by using the mode-matching technique (MMT). This technique relies on the properties of propagating acoustic duct modes. Depending upon the formulation of the physical problem, the eigen-sub-system may fall in Sturm-Liouville (SL) or non-Sturm-Liouville (non-SL) category. Section 2.1 and Section 2.2 provide the details regarding governing equation and boundary conditions, respectively. Section 2.3 contains some details related to the mathematical formulation of the relevant boundary value problems. To explain the mathematical modeling, the MM procedure, and relevant terminologies, a prototype bifurcated waveguide problem is explained in Section 2.4.

2.1 Physical Context

In this dissertation, the propagation, reflection, transmission, and absorption of acoustic waves in waveguides or channels are discussed. The propagation of acoustic waves in a medium is modeled in terms of a differential equation by using the

principles of continuum mechanics. The acoustic phenomena are usually concerned with the vibrations of small amplitudes in a compressible medium like air or water and consequently linearized description of continuum equations is more appropriate. Let us obtain the equations that govern the propagation of sound by using the concept of conservation of mass, momentum, and energy on a fluid volume element in the continuum.

The Equation of Continuity

The conservation of mass can be expressed mathematically as [64]

$$\frac{\partial \rho}{\partial t} + \nabla \cdot (\rho \mathbf{u}) = 0, \quad (2.1)$$

where ρ represents the mass density of fluid volume element, \mathbf{u} stands for the velocity vector of fluid particle, and t denotes the time variable.

The Equation of Momentum

The conservation of momentum for inviscid fluids can be expressed as [64]

$$\rho \left(\frac{\partial \mathbf{u}}{\partial t} + (\mathbf{u} \cdot \nabla) \mathbf{u} \right) + \nabla p = 0, \quad (2.2)$$

where p is the pressure of the fluid. When the fluid is at rest, these quantities have the constant values, i.e $\rho = \rho_o$, $\mathbf{u} = 0$ and $p = p_o$. If we are dealing with small fluctuations in the fluid, then we can define the following approximations

$$\begin{cases} \rho(r, t) = \rho_o + \rho'(r, t) + \dots, \\ \mathbf{u}(r, t) = \mathbf{u}'(r, t) + \dots, \\ p(r, t) = p_o + p'(r, t) + \dots \end{cases} \quad (2.3)$$

For linear acoustic analysis we can neglect the higher order terms or products of the fluctuations ρ' , \mathbf{u}' and p' . On using the linear settings, Eqs. (2.1), (2.2) and

(2.3) can be written as

$$\frac{\partial \rho'}{\partial t} + \rho_o \nabla \cdot \mathbf{u}' = 0, \quad (2.4)$$

and

$$\rho_o \frac{\partial \mathbf{u}'}{\partial t} + \nabla p' = 0, \quad (2.5)$$

respectively. Differentiating (2.4) with respect to t , taking divergence of (2.5), and then comparing the resulting equations, we get

$$\frac{\partial^2 \rho'}{\partial t^2} - \nabla^2 p' = 0. \quad (2.6)$$

For barotropic fluid (In fluid dynamics, a barotropic fluid is a fluid whose density is a function of pressure only) media ($p = p(\rho)$), the pressure fluctuations p' are related to p as (see [62])

$$p' = \frac{\partial p}{\partial \rho}(\rho_o) \rho'. \quad (2.7)$$

On using (2.7) to (2.6), the homogeneous wave equation is found to be

$$\frac{1}{c^2} \frac{\partial^2 \rho'}{\partial t^2} - \nabla^2 \rho' = 0, \quad (2.8)$$

or equivalently

$$\frac{1}{c^2} \frac{\partial^2 p'}{\partial t^2} - \nabla^2 p' = 0, \quad (2.9)$$

where

$$c = \sqrt{\frac{\partial p}{\partial \rho}(\rho_o)}, \quad (2.10)$$

is the speed of sound. To determine the speed of sound, we consider equation of state under adiabatic condition, which gives [62]

$$\frac{\partial p}{\partial \rho}(\rho_o) = \frac{\gamma_c p_o}{\rho_o}, \quad (2.11)$$

where γ_c is the ratio of heat capacity.

On using (2.11) in (2.10), we get $c = \sqrt{\frac{\gamma_c p_o}{\rho_o}}$.

For air medium, on setting $p_o = 1.01325 \times 10^5 Pa$, $\rho_o = 1.21 kg m^{-3}$, $\gamma_c = 1.402$ and the speed of sound $c = 343 m s^{-1}$.

It is useful to express the wave equation (2.9) in terms of field potential $\Phi(x, y, t)$ which is related to the pressure fluctuations p' and velocity fluctuations \mathbf{u}' by

$$p' = -\rho \frac{\partial \Phi}{\partial t}, \quad (2.12)$$

and

$$\mathbf{u}' = \nabla \Phi. \quad (2.13)$$

On using (2.12) in (2.9), the linear wave equation in terms of field potential $\Phi(x, y, t)$ can be written as

$$\frac{1}{c^2} \frac{\partial^2 \Phi}{\partial t^2} - \nabla^2 \Phi = 0, \quad (2.14)$$

Throughout this dissertation, the harmonic time dependence $e^{-i\omega t}$ is assumed. Thus, the two-dimensional time dependent field potential $\Phi(x, y, t)$ can be written as

$$\Phi(x, y, t) = \psi(x, y) e^{-i\omega t}, \quad (2.15)$$

where ω is the angular frequency and $\psi(x, y)$ is the time independent field potential. On substituting (2.15) into (2.14), we obtain

$$(\nabla^2 + k^2) \psi(x, y) = 0, \quad (2.16)$$

where $k = \omega/c$ denotes the wave number.

2.2 Boundary Conditions

In acoustics, the reaction of the surface to the sound is important and can be expressed in terms of boundary conditions. The nature and types of boundary conditions depend on the physical conditions assumed while modeling the acoustic problems. Boundary conditions can be classified in the following ways.

2.2.1 Impedance Condition

The ratio of the acoustic pressure to the normal velocity is known as the acoustic impedance of the surface [63, 65]. It is denoted by Z

$$Z = \frac{\text{Acoustic pressure}}{\text{Normal velocity}}. \quad (2.17)$$

By substituting (2.12) and (2.13) into (2.17), we get

$$Z = \frac{-\rho \frac{\partial \Phi}{\partial t}}{\hat{\mathbf{n}} \cdot \nabla \Phi}, \quad (2.18)$$

or

$$\rho \frac{\partial \Phi}{\partial t} + Z \hat{\mathbf{n}} \cdot \nabla \Phi = 0,$$

or

$$\rho Z^{-1} \frac{\partial \Phi}{\partial t} + \hat{\mathbf{n}} \cdot \nabla \Phi = 0,$$

or

$$\beta c^{-1} \frac{\partial \Phi}{\partial t} + \hat{\mathbf{n}} \cdot \nabla \Phi = 0, \quad (2.19)$$

where $\hat{\mathbf{n}}$ is the unit normal vector directed in the surface.

$\beta = \rho c Z^{-1}$ denotes the dimensionless specific admittance of the surface.

On using the harmonic time dependence $e^{-i\omega t}$, (2.19) becomes

$$-i\beta c^{-1} \omega \psi + \hat{\mathbf{n}} \cdot \nabla \psi = 0. \quad (2.20)$$

The above condition is basically Robin or mixed type of boundary condition. It is important to note that:

- For acoustically absorbent linings, the values of specific impedance

$\chi = \beta^{-1} = \xi + i\eta$ are as follows [11, 22]:

a) Fibrous sheet: $\xi = 0.5, \quad -1.0 < \eta < 3.0.$

b) Perforated sheet: $0 < \xi < 3.0, \quad -1.0 < \eta < 3.0.$

- When $Z \rightarrow \infty$ in (2.20), then the given surface is acoustically rigid

$$\hat{\mathbf{n}} \cdot \nabla \psi = 0, \quad (2.21)$$

which is Neumann type of boundary condition.

- When $Z \rightarrow 0$ in (2.20), then the given surface is acoustically soft

$$\psi = 0, \quad (2.22)$$

which is Dirichlet type of boundary condition.

2.2.2 Elastic Membrane Condition

To formulate the elastic membrane condition it is assumed that the tensile stress is same at every point on the membrane and at every orientation of the line element perpendicular to the membrane surface. These membranes are flexible like a sheet of rubber and have wave behaviour similar to that of waves on a string assemblage. Therefore, the tensile stress of the membrane can be referred as tension (T), and the wave equation for membrane can be found in many text, for instance, see [62, 65].

For membrane condition coupled with compressible fluid, the non-dimensional displacement $W(x, y, t)$ satisfies the equation of motion

$$\frac{\partial^2 W}{\partial x^2} - \frac{1}{c_m^2} \frac{\partial^2 W}{\partial t^2} = \frac{1}{T} [p']_{-}^{+}, \quad (2.23)$$

where $c_m = \sqrt{T/\rho_m}$ defines the sound's speed on membrane having mass density ρ_m . The quantity $[p']_{-}^{+} = [p']^{+} - [p']^{-}$ on the right hand side of the (2.23) denotes the fluid pressure difference across the membrane surface.

On using (2.12) in (2.23), we get

$$\frac{\partial^2 W}{\partial x^2} - \frac{1}{c_m^2} \frac{\partial^2 W}{\partial t^2} = \frac{-\rho}{T} \left[\frac{\partial \Phi}{\partial t} \right]_{-}^{+}. \quad (2.24)$$

Now using (2.15) in (2.24), we have

$$\frac{\partial^2 W}{\partial x^2} - \frac{1}{c_m^2} \frac{\partial^2 W}{\partial t^2} = \frac{i\omega\rho}{T} [\psi e^{-i\omega t}]_-^+. \quad (2.25)$$

Assuming the harmonic time dependence, it is convenient to express the membrane displacement W by

$$W(x, t) = w(x)e^{-i\omega t}. \quad (2.26)$$

Using (2.26) in (2.25), we get

$$\frac{\partial^2 w}{\partial x^2} + \frac{\omega^2}{c_m^2} w = \frac{i\omega\rho}{T} [\psi]_-^+. \quad (2.27)$$

As the membrane displacement W is related to field potential through the relation

$$\frac{\partial W}{\partial t} = \frac{\partial \Phi}{\partial y}. \quad (2.28)$$

Use (2.26) and (2.15) in (2.28), which for harmonic time dependence reveals

$$w = \frac{i}{\omega} \frac{\partial \psi}{\partial y}. \quad (2.29)$$

After substituting (2.29) in (2.27), we get

$$\left[\frac{\partial^2}{\partial x^2} + \frac{\omega^2}{c_m^2} \right] \frac{\partial \psi}{\partial y} = \frac{\omega^2 \rho}{T} [\psi]_-^+. \quad (2.30)$$

Edge Conditions:

The role of edge conditions is fundamental in deciding the remarkable mathematical solution of the problem as well as to depict the type of physical connection. In the case of elastic membrane, the edges or physical connections can be fixed, free or spring-like etc. Following two types of edge conditions are used in this thesis.

Fixed Edges:

For the fixed edge, the displacement of the membrane is assumed to be zero, that is

$$\frac{\partial \psi(0, a)}{\partial y} = 0. \quad (2.31)$$

Free Edges:

In this case, the gradient is assumed to be zero, that is

$$\frac{\partial^2 \psi(0, a)}{\partial xy} = 0. \quad (2.32)$$

It is also named as simply supported edge condition.

2.3 Mathematical Formulation

The current thesis investigates acoustic propagation, scattering, and absorption through a waveguide with compressible fluid inside and various wall conditions. Physical issues including rigid, soft, impedance, and/or higher order boundary conditions are governed by the Helmholtz equation. The dimensional form of differential system is explained in the subsequent subsections.

2.3.1 Dimensional Setting

The dimensional form of Helmholtz's equation is

$$\left\{ \frac{\partial^2}{\partial \bar{x}^2} + \frac{\partial^2}{\partial \bar{y}^2} + k^2 \right\} \bar{\psi}(\bar{x}, \bar{y}) = 0, \quad (2.33)$$

subject to the boundary conditions in the dimensional formulation

- Impedance Condition

$$\bar{Q}\bar{\psi} + \bar{\mathbf{n}} \cdot \nabla \bar{\psi} = 0, \quad (2.34)$$

where $\bar{Q} = \beta c^{-1}$.

- Rigid Condition

$$\bar{\mathbf{n}} \cdot \nabla \bar{\psi} = 0. \quad (2.35)$$

- Soft Condition

$$\bar{\psi} = 0. \quad (2.36)$$

- Membrane Condition

$$\left[\frac{\partial^2}{\partial \bar{x}^2} + \frac{\omega^2}{c_m^2} \right] \frac{\partial \bar{\psi}}{\partial \bar{y}} = \frac{\omega^2 \rho}{T} [\bar{\psi}]_-. \quad (2.37)$$

The overbars here and henceforth denote the dimensional setting of variables.

2.3.2 Non-dimensional Setting

We non-dimensionalize the governing differential system with the length scale k^{-1} and the time scale ω^{-1} under the transformations

$$x = k\bar{x}, \quad y = k\bar{y}, \quad t = \omega\bar{t} \quad \text{and} \quad \bar{\psi}(\bar{x}, \bar{y}) = \frac{1}{k^2} \psi(x, y), \quad (2.38)$$

which imply

$$\frac{\partial^2}{\partial \bar{x}^2} = k^2 \frac{\partial^2}{\partial x^2} \quad \text{and} \quad \frac{\partial^2}{\partial \bar{y}^2} = k^2 \frac{\partial^2}{\partial y^2}. \quad (2.39)$$

The dimensionless form of (2.33)-(2.37) is as follows:

- Helmholtz Equation

$$\left\{ \frac{\partial^2}{\partial x^2} + \frac{\partial^2}{\partial y^2} + 1 \right\} \psi(x, y) = 0. \quad (2.40)$$

- Impedance Condition

$$\mathcal{Q}\psi + \mathbf{n} \cdot \nabla \psi = \mathbf{0}, \quad (2.41)$$

where $\mathcal{Q} = -i\beta c^{-1}\omega$.

- Rigid Condition

$$\mathbf{n} \cdot \nabla \psi = \mathbf{0}. \quad (2.42)$$

- Soft Condition

$$\psi = 0. \quad (2.43)$$

- Membrane Condition

$$\left\{ \frac{\partial^2}{\partial x^2} + \mu^2 \right\} \frac{\partial \psi}{\partial y} - \alpha [\psi]_-^+ = 0, \quad (2.44)$$

where $\mu = c/c_m$ and $\alpha = c^2 \rho / (kT)$ denote the membrane wave number and fluid loading parameters, respectively.

2.3.3 Mode-matching Formulation

The problems considered in the thesis are analyzed with mode-matching technique. Generally, there are two possible approaches to deal with modelling finite-length dissipative silencers (mass reaction): the problem can be analyzed numerically, which obviously involves the use of the finite element method or the boundary element method; on the other hand, the problem can be solved analytically, which commonly involves finding roots of the dispersion relationship and using an orthogonality relationship to equalize the pressure and sound velocity fields on the inlet and outlet planes of the silencer. Taking a numerical approach, such as the finite element method, it is possible to study a silencer of any shape or size. However, with increasing excitation frequency and silencer dimensions, the number of degrees of freedom in the problem increases rapidly and, even for a relatively small automobile muffler, the subsequent CPU overhead quickly becomes restrictive [31].

An analytical approach is apparently desirable rather than a numerical one, and for automobile mufflers the mode matching approach has been shown to work well, albeit only in the case of zero mean flow. However, the analytical coincidence of the continuity conditions in the inlet/outlet planes of the silencer requires that a sufficient number of roots have been found in the dispersion relationship to achieve a convergent solution of the problem [32]. The technique is as follows; we determine the eigenfunction expansion form of propagating modes by using the separation of variable technique as given below

$$\psi(x, y) = \sum_{n=0}^{\infty} \mathcal{A}_n \mathcal{Y}_n(y) e^{\pm i \zeta_n x}. \quad (2.45)$$

Here, $\mathcal{Y}_n(y); n = 0, 1, 2, \dots$ are eigenfunctions and are found from the bounding wall conditions, \mathcal{A}_n are the mode amplitudes.

The associated eigenvalues linked with the mode wave numbers $\mathfrak{T}_n; n = 0, 1, 2, \dots$ are the roots of some dispersion relation.

Depending upon the associated eigenvalue problem, the eigenfunction may be orthogonal or non-orthogonal. The derivations of orthogonality relations (OR's) incorporated in this thesis can be explained as follows:

Orthogonality Relation with Impedance Boundary Conditions

Consider a wave propagating in a duct bounded by impedance boundary wall conditions at $y = a, b$ where $-\infty < x < \infty$.

On using (2.45) in the governing equations (2.40)-(2.41), the eigenvalue problem can be formulated as

$$\frac{\partial^2 \mathcal{Y}_n(y)}{\partial y^2} + \beta_n^2 \mathcal{Y}_n(y) = 0, \quad (2.46)$$

$$\mathcal{Q}_1 \mathcal{Y}_n(y) - \frac{\partial \mathcal{Y}_n(y)}{\partial y} = 0, \quad \text{at } y = a, \quad (2.47)$$

$$\mathcal{Q}_2 \mathcal{Y}_n(y) + \frac{\partial \mathcal{Y}_n(y)}{\partial y} = 0, \quad \text{at } y = b, \quad (2.48)$$

where $\beta_n = \sqrt{1 - \mathfrak{T}_n^2}$ denotes the eigenvalues and $\mathcal{Y}_n(y)$ are the eigenfunctions that satisfy orthogonality conditions.

The appropriation OR can be derived using (2.46)-(2.48), and is explained as follows:

On multiplying $\mathcal{Y}_m(y); m = 0, 1, 2, \dots$ with (2.46) and integrating over $a \leq y \leq b$, we get

$$\int_a^b \mathcal{Y}_m(y) \frac{\partial^2 \mathcal{Y}_n(y)}{\partial y^2} dy + \beta_n^2 \int_a^b \mathcal{Y}_m(y) \mathcal{Y}_n(y) dy = 0. \quad (2.49)$$

Applying integration by parts on first part of (2.49), we find

$$\int_a^b \mathcal{Y}_m(y) \frac{\partial^2 \mathcal{Y}_n(y)}{\partial y^2} dy = \left[\mathcal{Y}_m(y) \frac{\partial \mathcal{Y}_n(y)}{\partial y} \right]_a^b - \int_a^b \frac{\partial \mathcal{Y}_m(y)}{\partial y} \frac{\partial \mathcal{Y}_n(y)}{\partial y} dy. \quad (2.50)$$

Applying limits of integration, we get

$$\int_a^b \mathcal{Y}_m(y) \frac{\partial^2 \mathcal{Y}_n(y)}{\partial y^2} dy = \mathcal{Y}_m(b) \frac{\partial \mathcal{Y}_n}{\partial y}(b) - \mathcal{Y}_m(a) \frac{\partial \mathcal{Y}_n}{\partial y}(a) - \int_a^b \frac{\partial \mathcal{Y}_m(y)}{\partial y} \frac{\partial \mathcal{Y}_n(y)}{\partial y} dy. \quad (2.51)$$

Using (2.47) and (2.48) in (2.51), we find

$$\int_a^b \mathcal{Y}_m(y) \frac{\partial^2 \mathcal{Y}_n(y)}{\partial y^2} dy = -\mathcal{Y}_m(b)\mathcal{Y}_n(b) - \mathcal{Y}_m(a)\mathcal{Y}_n(a) - \int_a^b \frac{\partial \mathcal{Y}_m(y)}{\partial y} \frac{\partial \mathcal{Y}_n(y)}{\partial y} dy. \quad (2.52)$$

Use of (2.52) in (2.49) gives

$$\begin{aligned} & -\mathcal{Y}_m(b)\mathcal{Y}_n(b) - \mathcal{Y}_m(a)\mathcal{Y}_n(a) - \int_a^b \frac{\partial \mathcal{Y}_m(y)}{\partial y} \frac{\partial \mathcal{Y}_n(y)}{\partial y} dy \\ & \quad + \beta_n^2 \int_a^b \mathcal{Y}_m(y)\mathcal{Y}_n(y) dy = 0. \end{aligned} \quad (2.53)$$

On interchanging the indices m and n of (2.53), we get

$$\begin{aligned} & -\mathcal{Y}_n(b)\mathcal{Y}_m(b) - \mathcal{Y}_n(a)\mathcal{Y}_m(a) - \int_a^b \frac{\partial \mathcal{Y}_n(y)}{\partial y} \frac{\partial \mathcal{Y}_m(y)}{\partial y} dy \\ & \quad + \beta_m^2 \int_a^b \mathcal{Y}_n(y)\mathcal{Y}_m(y) dy = 0. \end{aligned} \quad (2.54)$$

On subtracting (2.54) from (2.53), we find

$$(\beta_n^2 - \beta_m^2) \int_a^b \mathcal{Y}_n(y)\mathcal{Y}_m(y) dy = 0, \quad (2.55)$$

which yields

$$\int_a^b \mathcal{Y}_m(y)\mathcal{Y}_n(y) dy = D_n \delta_{mn}, \quad (2.56)$$

where

$$D_n = \int_a^b \mathcal{Y}_n^2(y) dy, \quad (2.57)$$

and

$$\delta_{mn} = \begin{cases} 1, & m = n, \\ 0, & m \neq n, \end{cases} \quad (2.58)$$

is the Kronecker delta. Note that the value of D_n is linked with the formulation

of \mathcal{Y}_n that depends upon what conditions on the bounding walls are assumed.

Case-1:

With impedance walls, the value \mathcal{Y}_n is found by solving (2.46) subject to (2.47)-(2.48) as

$$\mathcal{Y}_n(y) = \sin[\beta_n(y - a)] + \beta_n \cos[\beta_n(y - a)], \quad (2.59)$$

where β_n are the roots of dispersion relation

$$(\mathcal{Q}_1 \mathcal{Q}_2 - \beta_n^2) \sin[\beta_n(b - a)] + (1 + \mathcal{Q}_1) \beta_n \cos[\beta_n(b - a)] = 0. \quad (2.60)$$

These roots can be found numerically and serve as eigenvalues of the assumed formulation. On using (2.59) in (2.57) we get

$$D_n = \frac{1}{4} \left\{ 2 - 2(a - b)(1 + \beta_n^2) - 2 \cos[2(-a + b)\beta_n] + \left(-\frac{1}{\beta_n} + \beta_n \right) \sin[2(-a + b)\beta_n] \right\}. \quad (2.61)$$

- When $\mathcal{Q}_1 \rightarrow 0$ and $\mathcal{Q}_2 \rightarrow 0$, the eigenvalue problem (2.46)-(2.48) can be formulated as

$$\frac{\partial^2 \mathcal{Y}_n(y)}{\partial y^2} + \beta_n^2 \mathcal{Y}_n(y) = 0, \quad (2.62)$$

$$\frac{\partial \mathcal{Y}_n(y)}{\partial y} = 0, \quad \text{at } y = a, \quad (2.63)$$

$$\frac{\partial \mathcal{Y}_n(y)}{\partial y} = 0, \quad \text{at } y = b. \quad (2.64)$$

Case-2:

With rigid walls, on solving (2.62)-(2.64), the value of \mathcal{Y}_n is found to be

$$\mathcal{Y}_n(y) = \cos[\beta_n(y - a)], \quad (2.65)$$

where

$$\beta_n = \frac{n\pi}{b - a}, \quad n = 0, 1, 2, \dots \quad (2.66)$$

On using (2.65) in (2.57) we get

$$D_n = \frac{b-a}{2}. \quad (2.67)$$

- When $\mathcal{Q}_1 \rightarrow \infty$ and $\mathcal{Q}_2 \rightarrow \infty$, (2.46)-(2.48) lead to the following eigenvalue problem

$$\frac{\partial^2 \mathcal{Y}_n(y)}{\partial y^2} + \beta_n^2 \mathcal{Y}_n(y) = 0, \quad (2.68)$$

$$\mathcal{Y}_n(y) = 0, \quad \text{at} \quad y = a, \quad (2.69)$$

$$\mathcal{Y}_n(y) = 0, \quad \text{at} \quad y = b. \quad (2.70)$$

Case-3:

With soft walls, on solving (2.68)-(2.70), the value of \mathcal{Y}_n is found to be

$$\mathcal{Y}_n(y) = \sin[\beta_n(y-a)], \quad (2.71)$$

where

$$\beta_n = \frac{n\pi}{b-a}, \quad n = 1, 2, \dots \quad (2.72)$$

On using (2.71), (2.57) yields

$$D_n = \frac{b-a}{2}. \quad (2.73)$$

Orthogonality Condition with Rigid-membrane Boundary Condition

Consider a wave propagating in a duct bounded by rigid boundary wall condition at $y = a$ and membrane wall condition at $y = b$ respectively, where $-\infty < x < \infty$.

On using (2.45) in the governing equations (2.40) subject to the boundary conditions (2.42) and (2.44), the eigenvalue problem can be formulated as

$$\frac{\partial^2 \mathcal{Y}_n(y)}{\partial y^2} - \gamma_n^2 \mathcal{Y}_n(y) = 0, \quad (2.74)$$

$$\frac{\partial \mathcal{Y}_n(y)}{\partial y} = 0, \quad \text{at} \quad y = a, \quad (2.75)$$

$$(\gamma_n^2 + 1 - \mu^2) \frac{\partial \mathcal{Y}_n(y)}{\partial y} - \alpha \mathcal{Y}_n(y) = 0, \quad \text{at} \quad y = b. \quad (2.76)$$

where $\mathcal{Y}_n(y); n = 0, 1, 2, \dots$ are the eigenfunctions having eigenvalues $\gamma_n = \sqrt{\mathfrak{I}_n^2 - 1}$. The eigenfunctions $\mathcal{Y}_n(y); n = 0, 1, 2, \dots$ satisfy orthogonality relation which is different from the usual OR (2.56), and that can be referred as generalized orthogonality.

To develop generalized OR, we multiply (2.76) with $\frac{\partial \mathcal{Y}_m}{\partial y}(b)$ to get

$$(\gamma_n^2 + 1 - \mu^2) \frac{\partial \mathcal{Y}_n}{\partial y}(b) \frac{\partial \mathcal{Y}_m}{\partial y}(b) - \alpha \mathcal{Y}_n(b) \frac{\partial \mathcal{Y}_m}{\partial y}(b) = 0. \quad (2.77)$$

On interchanging the indices m and n of (2.77), that yields

$$(\gamma_m^2 + 1 - \mu^2) \frac{\partial \mathcal{Y}_m}{\partial y}(b) \frac{\partial \mathcal{Y}_n}{\partial y}(b) - \alpha \mathcal{Y}_m(b) \frac{\partial \mathcal{Y}_n}{\partial y}(b) = 0. \quad (2.78)$$

Subtracting (2.78) from (2.77) leads to

$$(\gamma_n^2 - \gamma_m^2) \frac{\partial \mathcal{Y}_n}{\partial y}(b) \frac{\partial \mathcal{Y}_m}{\partial y}(b) - \alpha \left[\mathcal{Y}_n(b) \frac{\partial \mathcal{Y}_m}{\partial y}(b) - \mathcal{Y}_m(b) \frac{\partial \mathcal{Y}_n}{\partial y}(b) \right] = 0. \quad (2.79)$$

Eq. (2.79) together with (2.75) gives

$$(\gamma_n^2 - \gamma_m^2) \frac{\partial \mathcal{Y}_n}{\partial y}(b) \frac{\partial \mathcal{Y}_m}{\partial y}(b) - \alpha \int_a^b \left[\mathcal{Y}_n(y) \frac{\partial^2 \mathcal{Y}_m(y)}{\partial y^2} - \mathcal{Y}_m(y) \frac{\partial^2 \mathcal{Y}_n(y)}{\partial y^2} \right] dy = 0. \quad (2.80)$$

Consequently, from (2.74) that finally yields

$$(\gamma_n^2 - \gamma_m^2) \left\{ \frac{\partial \mathcal{Y}_n}{\partial y}(b) \frac{\partial \mathcal{Y}_m}{\partial y}(b) + \alpha \int_a^b \mathcal{Y}_n(y) \mathcal{Y}_m(y) dy \right\} = 0. \quad (2.81)$$

The generalized orthogonality relation is as follows

$$\alpha \int_a^b \mathcal{Y}_n(y) \mathcal{Y}_m(y) dy + \frac{\partial \mathcal{Y}_n}{\partial y}(b) \frac{\partial \mathcal{Y}_m}{\partial y}(b) = F_n \delta_{mn}, \quad (2.82)$$

where

$$F_n = \left[\frac{\partial \mathcal{Y}_n}{\partial y}(b) \right]^2 + \alpha \int_a^b \mathcal{Y}_n^2(y) dy. \quad (2.83)$$

Interface Conditions:

The eigen expansion of propagating modes (2.45) involves unknown model coefficients that are determined by utilizing the matching interface conditions.

- At aperture interface of two duct regions, the pressures and normal components of velocities are assumed continuous, that gives

$$p'_{left}|_{\Omega} = p'_{right}|_{\Omega}, \quad (2.84)$$

$$\mathbf{u}'_{left} \cdot \mathbf{n}|_{\Omega} = \mathbf{u}'_{right} \cdot \mathbf{n}|_{\Omega}, \quad (2.85)$$

where Ω denotes the aperture domain.

- At surface interface, the normal velocity is related through the surface impedance Z , that gives

$$\mathbf{u}' \cdot \mathbf{n}|_{\Omega_1} = \pm Z^{-1} p'|_{\Omega_1}, \quad (2.86)$$

where Ω_1 is the domain of surface lying at interface.

Energy Flux:

The energy flux or power (\mathcal{P}) provides the understanding about the physical aspect of scattering as well as a check on the accuracy of performed algebra.

The formula to obtain energy flux through fluid medium is [44]

$$\mathcal{P}]_{fluid} = \text{Re} \left\{ i \int_a^b \psi \left(\frac{\partial \psi}{\partial x} \right)^* dy \right\}, \quad (2.87)$$

where superposed asterisk (*) specifies for complex conjugate. Accordingly, the mathematical form of energy flux propagating via elastic membrane is given by [44]

$$\mathcal{P}]_{memb} = \text{Re} \left\{ \frac{i}{\alpha} \left(\frac{\partial \psi}{\partial y} \right) \left(\frac{\partial^2 \psi}{\partial x \partial y} \right)^* \right\}. \quad (2.88)$$

Note that by using (2.87) and (2.88), we may construct a conserve power identity based upon the law of conservation of energy and that may serve as a physical check on the accuracy of truncated solution.

2.4 Canonical Problem

A bifurcated boundary value problem is presented in this section. The main purpose behind this section is to formulate a boundary value problem involving structural discontinuities for rigid-impedance (RI), rigid-rigid (RR) and rigid-soft (RS) boundaries and obtain the solution by MM technique.

2.4.1 Mathematical Formulation

In this problem, we consider a two dimensional infinite bifurcated waveguide structure. This bifurcated waveguide is divided in three semi infinite duct regions $\mathcal{R}_j, j = 1, 2, 3$. The inside of the regions $\mathcal{R}_j, j = 1, 2, 3$ are filled with compressible fluid of density ρ and sound speed c .

The bounding wall conditions of the regions \mathcal{R}_1 and \mathcal{R}_2 are acoustically rigid while \mathcal{R}_3 are impedance.

The outside of the waveguide is set in *vacou*. At $\bar{x} = 0$, there lies two rigid vertical step discontinuities aligned along with $-\bar{b} \leq \bar{y} \leq -\bar{a}$ and $\bar{a} \leq \bar{y} \leq \bar{b}$.

The BVP is described in terms of field potential $\bar{\Phi}(\bar{x}, \bar{y}, \bar{t})$ which satisfies the wave equation

$$\frac{\partial^2 \bar{\Phi}}{\partial \bar{x}^2} + \frac{\partial^2 \bar{\Phi}}{\partial \bar{y}^2} = \frac{1}{c^2} \frac{\partial^2 \bar{\Phi}}{\partial \bar{t}^2}, \quad (2.89)$$

where $\bar{\Phi}(\bar{x}, \bar{y}, \bar{t})$ is dimensional and time-harmonic dependent field potential in the waveguide which may be written in the form

$$\bar{\Phi}(\bar{x}, \bar{y}, \bar{t}) = \bar{\psi}(\bar{x}, \bar{y}) e^{-i\omega \bar{t}}, \quad (2.90)$$

where, $\bar{\psi}(\bar{x}, \bar{y})$ satisfies Helmholtz's equation as derived in many reference texts like Crighton et al. (1992), that is

$$\left\{ \frac{\partial^2}{\partial \bar{x}^2} + \frac{\partial^2}{\partial \bar{y}^2} + k^2 \right\} \bar{\psi}(\bar{x}, \bar{y}) = 0. \quad (2.91)$$

On non-dimensionalizing the boundary value problem with respect to the length scale k^{-1} and the time scale ω^{-1} under the transformations $x = k\bar{x}$, $y = k\bar{y}$ and

$t = \omega\bar{t}$. An overbar has hitherto indicated a dimensional quantity and henceforth its un-barred counterpart is non-dimensional.

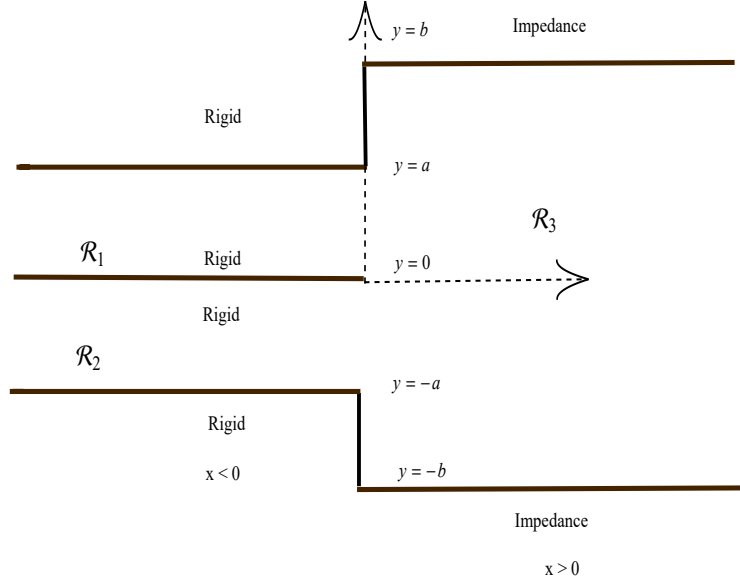


FIGURE 2.1: Geometry of the proposed model.

Thus, the non-dimensionalised field potential is given in terms of its dimensional counterpart as

$$\bar{\psi}(\bar{x}, \bar{y}) = \frac{1}{k^2} \psi(x, y), \quad (2.92)$$

and the second order derivatives with respect to \bar{x} and \bar{y} are found to be

$$\frac{\partial^2}{\partial \bar{x}^2} = k^2 \frac{\partial^2}{\partial x^2}, \quad \frac{\partial^2}{\partial \bar{y}^2} = k^2 \frac{\partial^2}{\partial y^2}. \quad (2.93)$$

Using (2.92) and (2.93) in (2.91), we get

$$\left\{ \frac{\partial^2}{\partial x^2} + \frac{\partial^2}{\partial y^2} + 1 \right\} \psi(x, y) = 0. \quad (2.94)$$

Consider an incident wave propagating in \mathcal{R}_1 from negative x -direction towards $x = 0$.

At $x = 0$, it will scatter in infinite number of reflected and transmitted modes.

The physical configuration of the problem is shown in Figure 2.1.

The non-dimensional field potentials that characterize the scattering fields in different duct regions may be written as:

$$\psi(x, y) = \begin{cases} \psi_1(x, y), & (x, y) \in \mathcal{R}_1, \\ \psi_2(x, y), & (x, y) \in \mathcal{R}_2, \\ \psi_3(x, y), & (x, y) \in \mathcal{R}_3. \end{cases} \quad (2.95)$$

In \mathcal{R}_j ; $j = 1, 2, 3$, the non-dimensional form of rigid boundary conditions are:

$$\frac{\partial \psi_1}{\partial y} = 0, \quad y = 0, a, \quad x < 0, \quad (2.96)$$

$$\frac{\partial \psi_2}{\partial y} = 0, \quad y = -a, 0, \quad x < 0, \quad (2.97)$$

$$\frac{\partial \psi_3}{\partial x} = 0, \quad x = 0, \quad \text{for } -b \leq y \leq -a \text{ and } a \leq y \leq b. \quad (2.98)$$

Here, (2.98) represents the rigid conditions for two vertical step discontinuities. Similarly, the impedance type conditions for \mathcal{R}_3 are

$$p\psi_3 \pm q \frac{\partial \psi_3}{\partial y} = 0, \quad y = \pm b, \quad x > 0. \quad (2.99)$$

Moreover, the continuity conditions of the fluid pressures and normal velocities at matching interface are

$$\psi_2 = \psi_3, \quad x = 0, \quad -a \leq y \leq 0, \quad (2.100)$$

$$\psi_1 = \psi_3, \quad x = 0, \quad 0 \leq y \leq a, \quad (2.101)$$

and

$$\psi_{3x} = \begin{cases} 0 & x = 0, & -b \leq y < -a, \\ \psi_{2x} & x = 0, & -a \leq y \leq 0, \\ \psi_{1x} & x = 0, & 0 \leq y \leq a, \\ 0 & x = 0, & a \leq y < b. \end{cases} \quad (2.102)$$

The subscript x here denotes differentiation with respect to x .

2.4.2 Eigenfunction Expansions

In this section, we use separation of variables to find the field potentials (ψ_1, ψ_2 and ψ_3) of respective regions. The dimensionless field potential ψ_1 can be written as

$$\psi_1 = \psi_{inc} + \psi_{ref}. \quad (2.103)$$

Consider the incident wave $\psi_{inc} = e^{ix}$ and the reflected field ψ_{ref} as an infinite sum of reflected duct modes, written in the form

$$\psi_{ref} = \sum_{n=0}^{\infty} A_n \psi_{1n}. \quad (2.104)$$

We can determine ψ_{1n} , $n = 0, 1, 2, \dots$ using separation of variables method.

In the usual manner ψ_{1n} is written as

$$\psi_{1n}(x, y) = X_1(x)Y_1(y). \quad (2.105)$$

Using (2.105) in (2.94), we have

$$\frac{X_1''}{X_1} = -\frac{Y_1''}{Y_1} - 1 = -\eta^2. \quad (2.106)$$

Thus

$$X_1(x) = a_1 e^{i\eta x} + b_1 e^{-i\eta x}, \quad (2.107)$$

$$Y_1(y) = c_1 \cos(\tau y) + d_1 \sin(\tau y), \quad (2.108)$$

where a_1, b_1, c_1 and d_1 are arbitrary constants.

Since reflected waves propagate in the negative x -direction then $a_1 = 0$ and since all duct surfaces are rigid, $d_1 = 0$ and $\tau_n = \frac{n\pi}{a}$.

It follows that

$$\psi_{1n}(x, y) = Y_{1n}(y)e^{-i\eta_n x}. \quad (2.109)$$

The quantity $\eta_n = \sqrt{1 - \tau_n^2}$ be the n^{th} reflected mode wave number in which τ_n ; $n = 0, 1, 2, \dots$ are the eigenvalues and $Y_{1n}(y) = \cos\left(\frac{n\pi}{a}y\right)$ is the eigenfunction.

Thus, ψ_1 gets the form

$$\psi_1(x, y) = e^{ix} + \sum_{n=0}^{\infty} A_n Y_{1n}(y) e^{-i\eta_n x}, \quad (2.110)$$

where, A_n are the unknown amplitudes of eigenfunction expansion ψ_1 .

The quantity η_n is the reflected mode wave number in which τ_n ; $n = 0, 1, 2, \dots$ are the eigenvalues satisfying the dispersion relation

$$\sin(\tau_n a) = 0, \text{ for } n = 0, 1, 2, \dots \quad (2.111)$$

The corresponding eigenfunctions $Y_{1n}(y)$ satisfy the orthogonality relation

$$\int_0^a Y_{1m}(y) Y_{1n}(y) dy = \frac{a}{2} \delta_{mn} \epsilon_m, \quad (2.112)$$

where, δ_{mn} is Kronecker delta and $\epsilon_m = 2$ for $m = 0$ and 1 otherwise.

Note that, the first term in (2.110) denotes the incident wave while the second term represent the reflected field in which A_n , $n = 0, 1, 2, \dots$, are the reflected mode coefficients and are unknowns. These unknowns will be found later from matching conditions. The field potential, ψ_2 is made up of reflected waves and so in similar manner

$$\psi_{2n}(x, y) = X_2(x) Y_2(y). \quad (2.113)$$

Using (2.113) in (2.94), we get

$$\frac{X_2''}{X_2} = -\frac{Y_2''}{Y_2} - 1 = -\xi^2. \quad (2.114)$$

After solving, we get

$$X_2(x) = a_2 e^{i\xi x} + b_2 e^{-i\xi x}, \quad (2.115)$$

$$Y_2(y) = c_2 \cos(\nu y) + d_2 \sin(\nu y), \quad (2.116)$$

where a_2 , b_2 , c_2 and d_2 are arbitrary constants.

Since reflected waves propagate in the negative x -direction therefore $a_2 = 0$ and as all duct surfaces are rigid, $d_2 = 0$ and $\nu_n = \frac{n\pi}{a}$.

It follows that

$$\psi_{2n}(x, y) = Y_{2n}(y)e^{-i\xi_n x}. \quad (2.117)$$

The quantity $\xi_n = \sqrt{1 - \nu_n^2}$ is the reflected mode wave number in which ν_n ; $n = 0, 1, 2, \dots$ are the eigenvalues and $Y_{2n}(y) = \cos\left(\frac{n\pi}{a}y\right)$ is the eigenfunction.

Thus, the eigenfunction expansion ψ_2 becomes

$$\psi_2(x, y) = \sum_{n=0}^{\infty} B_n Y_{2n}(y) e^{-i\xi_n x}, \quad (2.118)$$

where B_n are the unknown amplitudes of eigenfunction expansion ψ_2 and the eigenvalues ν_n ; $n = 0, 1, 2, \dots$ satisfy the dispersion relation

$$\sin(\xi_n a) = 0, \text{ for } n = 0, 1, 2, \dots \quad (2.119)$$

The corresponding eigenfunctions $Y_{2n}(y)$, $n = 0, 1, 2, \dots$, satisfy the orthogonality relation

$$\int_{-a}^0 Y_{2m}(y) Y_{2n}(y) dy = \frac{a}{2} \delta_{mn} \epsilon_m. \quad (2.120)$$

Similarly, the field potential ψ_3 is made up purely of transmitted waves and so

$$\psi_{3n}(x, y) = X_3(x) Y_3(y). \quad (2.121)$$

Using (2.121) in (2.94), we get

$$\frac{X_3''}{X_3} = -\frac{Y_3''}{Y_3} - 1 = -\kappa^2. \quad (2.122)$$

Thus, we have

$$X_3(x) = a_3 e^{i\kappa x} + b_3 e^{-i\kappa x}, \quad (2.123)$$

$$Y_3(y) = c_3 \cos(\lambda y) + d_3 \sin(\lambda y), \quad (2.124)$$

where, a_3 , b_3 , c_3 and d_3 are arbitrary constants. Since transmitted waves propagate in the positive x -direction then $b_3 = 0$ and as both surfaces have the impedance type boundary conditions, it follows that

$$\psi_{3n}(x, y) = Y_{3n}(y)e^{i\kappa_n x}, \quad (2.125)$$

where

$$Y_{3n}(y) = p \sin [\lambda_n(y + b)] + q\lambda_n \cos [\lambda_n(y + b)], \quad (2.126)$$

and

$$\kappa_n = \sqrt{1 - \lambda_n^2}. \quad (2.127)$$

Thus, ψ_3 has the form

$$\psi_3(x, y) = \sum_{n=0}^{\infty} C_n Y_{3n}(y)e^{i\kappa_n x}, \quad (2.128)$$

where C_n are the unknown amplitudes of eigenfunction expansion ψ_3 and κ_n is the wave number of the transmitted mode and $\lambda_n; n = 0, 1, 2, \dots$ are the eigenvalues.

Thus, these eigenvalues satisfy the dispersion relation

$$2pq\lambda_n \cos(2\lambda_n b) + (p^2 - q^2\lambda_n^2) \sin(2\lambda_n b) = 0, \text{ for } n = 0, 1, 2, \dots \quad (2.129)$$

The corresponding eigenfunctions $Y_{3n}(y); n = 0, 1, 2, \dots$ are orthogonal and satisfy the usual orthogonality relation

$$\int_{-b}^b Y_{3m}(y)Y_{3n}(y)dy = E_n\delta_{mn}, \quad (2.130)$$

where

$$E_n = \frac{1}{4} \left(2pq - 2pq \cos(4b\lambda_n) + 4b(p^2 + q^2\lambda_n^2) + \frac{(-p^2 + q^2\lambda_n^2) \sin(4b\lambda_n)}{\lambda_n} \right). \quad (2.131)$$

2.4.3 Mode-matching Solution

The unknown coefficients $\{A_n, B_n, C_n\}; n = 0, 1, 2, \dots$ involved in eigenfunction expansions ψ_1, ψ_2 and ψ_3 are found by using the matching conditions (2.100)-(2.102).

On using (2.110) and (2.128) in (2.101), we get

$$1 + \sum_{n=0}^{\infty} A_n Y_{1n}(y) = \sum_{n=0}^{\infty} C_n Y_{3n}(y). \quad (2.132)$$

On multiplying (2.132) with $Y_{1m}(y)$, integrating from 0 to a and then using the orthogonality relation (2.112), we get

$$A_m = \frac{-2\delta_{m0}}{\epsilon_m} + \frac{2}{a\epsilon_m} \sum_{n=0}^{\infty} C_n R_{mn}, \quad (2.133)$$

where

$$R_{mn} = \int_0^a Y_{1m}(y) Y_{3n}(y) dy. \quad (2.134)$$

On using (2.111) and (2.128) in (2.100), we get

$$\sum_{n=0}^{\infty} B_n Y_{2n}(y) = \sum_{n=0}^{\infty} C_n Y_{3n}(y). \quad (2.135)$$

Multiplying (2.135) with $Y_{2m}(y)$, integrating from $-a$ to 0 and then using the orthogonality relation (2.120), we get

$$B_m = \frac{2}{a\epsilon_m} \sum_{n=0}^{\infty} C_n P_{mn}, \quad (2.136)$$

where

$$P_{mn} = \int_{-a}^0 Y_{2m}(y) Y_{3n}(y) dy. \quad (2.137)$$

To determine the transmitted modes coefficients, we use (2.110), (2.118), and (2.128) in (2.102) to obtain

$$\sum_{n=0}^{\infty} C_n \kappa_n Y_{3n}(y) = \begin{cases} 0, & -b \leq y < -a, \\ -\sum_{n=0}^{\infty} B_n v_n Y_{2n}(y), & -a \leq y < 0, \\ 1 - \sum_{n=0}^{\infty} A_n \eta_n Y_{1n}(y), & 0 \leq y < a, \\ 0, & a \leq y \leq b. \end{cases} \quad (2.138)$$

On multiplying with $Y_{3m}(y)$, integrating from $-b$ to b and then using the orthogonality relation (2.130), we get

$$C_m = \frac{R_{0m}}{\kappa_m E_m} - \frac{1}{\kappa_m E_m} \sum_{n=0}^{\infty} A_n \eta_n R_{nm} - \frac{1}{\kappa_m E_m} \sum_{n=0}^{\infty} B_n v_n P_{nm}. \quad (2.139)$$

In this way (2.139) leads to a system of infinite equations in which $C_m; m = 0, 1, 2, \dots$, are unknowns. These are truncated and inverted to determine the unknown model coefficients. Once obtained $C_m; m = 0, 1, 2, \dots$, the quantities $\{A_m, B_m\}; m = 0, 1, 2, \dots$ are found easily by using (2.133) and (2.136).

2.4.4 Energy Balance

In this section, we determine the expressions of energy flux in the inlet and outlet duct regions of waveguide. As the boundaries of the waveguide are assumed rigid, soft and impedance type so it is considered that no power will be lost and so the law of conservation holds. Hence, it will be shown that incident power will be equal to sum of the reflected and transmitted powers.

The energy flux/power inside the duct regions in terms of non-dimensional time harmonic fluid velocity potential is defined by

$$\frac{\partial \mathcal{E}}{\partial t} = \frac{1}{2} \text{Re} \left\{ i \int_{\Omega} \psi \left(\frac{\partial \psi}{\partial x} \right)^* dy \right\}, \quad (2.140)$$

where, superscript asterisk (*) denotes the complex conjugate.

From the definition of energy flux/power, the incident field takes the form of a wave with unit amplitude and so, \mathcal{P}_{inc} the power fed in the system per unit length is given by

$$\mathcal{P}_{inc} = \frac{1}{2} \text{Re} \left\{ \int_0^a i e^{ix} (-i e^{-ix}) dy \right\} = \frac{a}{2}. \quad (2.141)$$

Likewise, the power/energy flux components in duct region $\mathcal{R}_j; j = 1, 2, 3$ are:

$$\mathcal{P}_1 = \frac{a}{4} \text{Re} \left\{ \sum_{n=0}^{\infty} |A_n|^2 \eta_n \epsilon_n \right\}, \quad (2.142)$$

$$\mathcal{P}_2 = \frac{a}{4} \text{Re} \left\{ \sum_{n=0}^{\infty} |B_n|^2 \nu_n \epsilon_n \right\}, \quad (2.143)$$

and

$$\mathcal{P}_3 = \frac{1}{2} \text{Re} \left\{ \sum_{n=0}^{\infty} |C_n|^2 \kappa_n E_n \right\}. \quad (2.144)$$

Now, it is important to note that the power fed in the system will be equal to the sum of scattering powers in different duct regions, that is:

$$\mathcal{P}_{inc} = \mathcal{P}_1 + \mathcal{P}_2 + \mathcal{P}_3, \quad (2.145)$$

which is conserved power identity.

For analysis purpose, we may scale the incident power at unity.

For this, we divide (2.145) by $\frac{a}{2}$ to get

$$\mathcal{E}_T = \sum_{j=1}^3 \mathcal{E}_j,$$

where,

$$\mathcal{E}_j = \frac{\mathcal{P}_j}{\mathcal{P}_{inc}} \quad j = 1, 2, 3$$

denote the power/energy flux components in duct regions R_j ; $j = 1, 2, 3$ for which the incident power is being scaled at unity.

2.4.5 Numerical Results and Discussions

This section provides graphical illustration of the scattered fields. For this purpose, we truncate the system upto N terms and solve the infinite system given by equations defined by (2.139) to compute unknown coefficients to be used in eigenfunction expansion of respective field potentials. The truncated solution can be used to check the accuracy of presented algebra and distribution of power or energy flux.

The purpose of the graphical results herein, is to analyze the scattering of powers or energies versus frequency (in hertz).

The presented graphical figures are obtained for a fixed choice of rigid boundary conditions of all walls of the duct sections \mathcal{R}_1 and \mathcal{R}_2 , whilst upper and lower boundaries of the outlet duct section \mathcal{R}_3 are varying with following types of boundary conditions.

- Impedance Type:

For this type, the parameters are fixed as $p = q = 1$.

- Rigid Type:

For this type, the parameters are fixed as $p = 0$ and $q = 1$.

- Soft Type:

For this type, the parameters are fixed as $p = 1$ and $q = 0$.

Figures 2.2(a) and 2.2(b) are plotted to see the behavior of reflected power (\mathcal{E}_1) against frequency regime ($1Hz - 750Hz$), with ($a \neq b$) and without step-discontinuities ($a = b$) respectively.

It is noted that for Figure 2.2(a), the reflected energy goes to its minimum value (for all impedance, rigid and soft cases) at higher frequencies and fluctuation in power reflection goes maximum in the presence of step-discontinuities. On the other hand, Figure 2.2(b) depicts the reflected powers (\mathcal{E}_1) scattering results in the absence of step-discontinuities by assuming the parameters $\bar{a} = \bar{b} = 0.24m$.

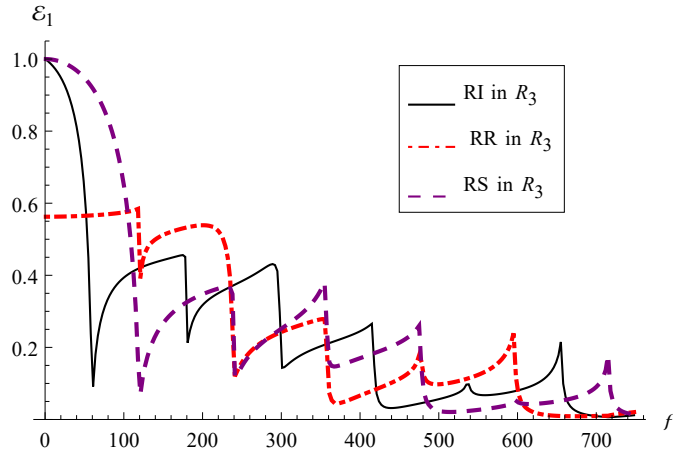
Tables 2.1 and 2.2 show a list of cut-on modes vs frequency for different duct regions.

- Rigid-impedance Case:

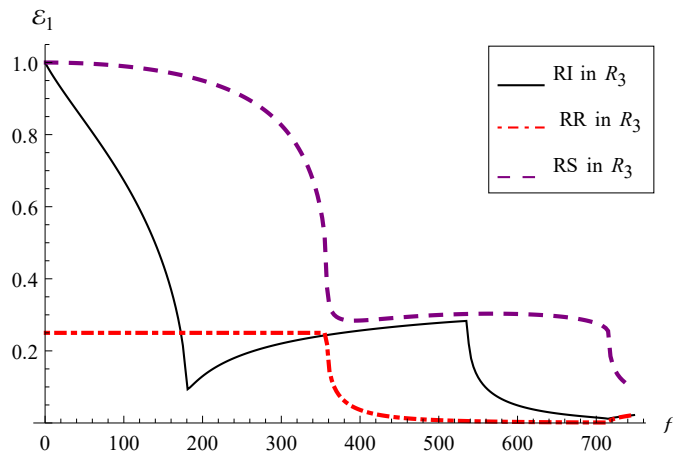
It is noted that for RI case, seven duct modes are cut-on in the presence of step-discontinuities at frequencies (61, 179, 299, 418, 537, 656, 716)Hz but in planar case, four duct modes are cut-on at frequencies (179, 358, 537, 716)Hz.

- Rigid-rigid Case:

For RR case, seven duct modes are cut-on involving step-discontinuities at frequencies (1, 120, 239, 358, 478, 597, 716)Hz but in planar case, four duct modes are cut-on at frequencies (1, 358, 716)Hz.



(a)



(b)

FIGURE 2.2: Reflected energy (\mathcal{E}_1) versus frequency (f) with RR conditions in \mathcal{R}_1 and \mathcal{R}_2 , and RI , RR and RS conditions in \mathcal{R}_3 (a) with step-discontinuous ($a \neq b$) (b) without step-discontinuous ($a = b$), where $\bar{a} = 0.24m$, $\bar{b} = 3\bar{a}$ and $N = 10$.

- Rigid-soft Case:

For RS case, seven duct modes are cut-on involving step-discontinuities at frequencies $(1, 120, 239, 358, 478, 597, 716)Hz$ while in planar case, four duct modes are cut-on at frequencies $(1, 358, 716)Hz$.

These cut-on modes are obtained for RI, RR and RS type outer bounding walls. It is noted that less fluctuations are observed for continuous case and cut-on modes reduce in number (see Table 2.2).

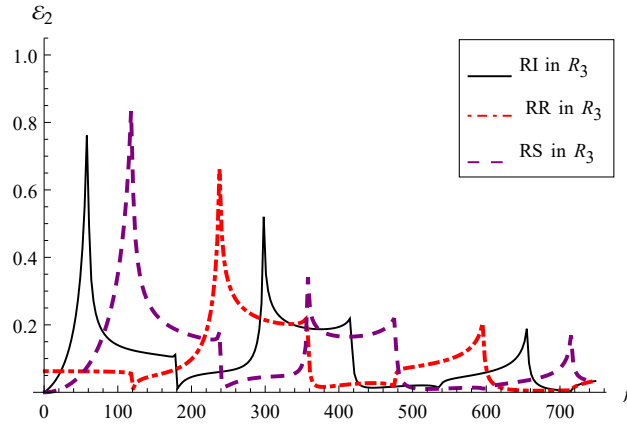
TABLE 2.1: Propagating modes of regions \mathcal{R}_j , $j = 1, 2, 3 \dots$ for discontinuous waveguides

Cut-on frequency(Hz)	No. of cut-ons in \mathcal{R}_1	No. of cut-ons in \mathcal{R}_2	No. of cut-ons in \mathcal{R}_3		
			RR	RS	RI
1	1	1	1	1	0
61	1	1	1	1	1
120	1	1	2	2	1
179	1	1	2	2	2
239	1	1	3	3	2
299	1	1	3	3	3
358	1	1	4	4	3
418	1	1	4	4	4
478	1	1	5	5	4
537	1	1	5	5	5
597	1	1	6	6	5
656	1	1	6	6	6
716	2	2	7	7	6

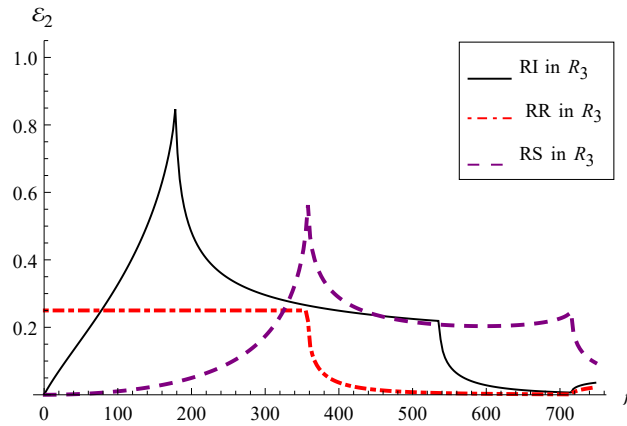
TABLE 2.2: Propagating modes of regions \mathcal{R}_j , $j = 1, 2, 3 \dots$ for planar waveguides

Cut-on frequency(Hz)	No. of cut-ons in \mathcal{R}_1	No. of cut-ons in \mathcal{R}_2	No. of cut-ons in \mathcal{R}_3		
			RR	RS	RI
1	1	1	1	1	0
179	1	1	1	1	1
358	1	1	2	2	1
537	1	1	2	2	2
716	2	2	3	3	2

More cut-on modes are observed for discontinuous waveguide indicates that more energy is absorbed whereas, less amount of energy is absorbed when step of discontinuity is removed due to small number of cut-on modes (see Table 2.1).



(a)



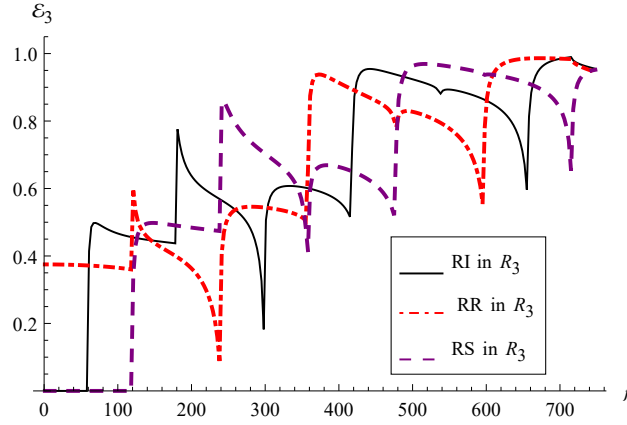
(b)

FIGURE 2.3: Reflected energy (\mathcal{E}_2) versus frequency (f) with RR conditions in \mathcal{R}_1 and \mathcal{R}_2 , and RI , RR and RS conditions in \mathcal{R}_3 (a) with step-discontinuous ($a \neq b$) (b) without step-discontinuous ($a = b$), where $\bar{a} = 0.24m$, $\bar{b} = 3\bar{a}$ and $N = 10$.

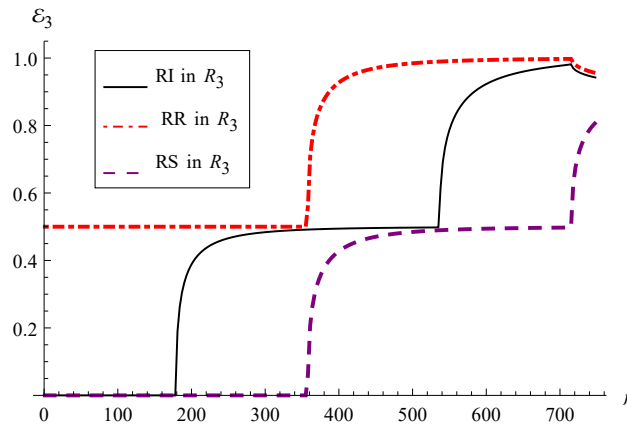
Figures 2.3(a) and 2.3(b) are plotted between reflected power (\mathcal{E}_2) versus frequency f , with and without multiple step-discontinuities respectively. Two situations are considered that is; measure of reflected energy due to (a) step-discontinuities and (b) without step-discontinuities. Again, a similar behavior in the reflected energy is observed.

For discontinuous cases, there are more fluctuations in the reflected energy, which gradually diminishes as the frequency increases. The reflected energy for all impedances, rigid and soft cases, drops to zero at higher frequencies. Figure 2.3(b)

shows a smooth behaviour when $f < 361$ is rigid and goes to its minimum value for higher frequencies.



(a)

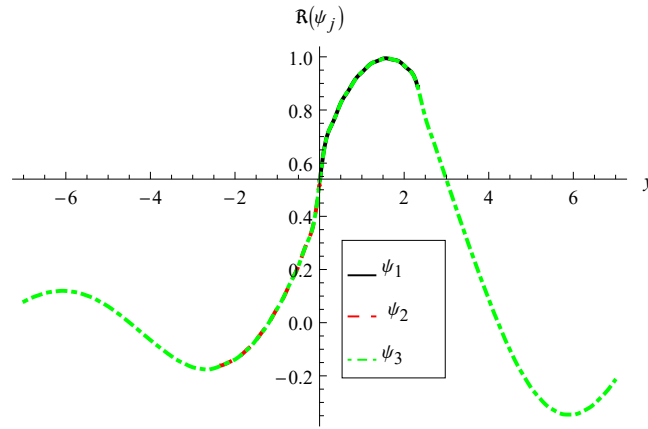


(b)

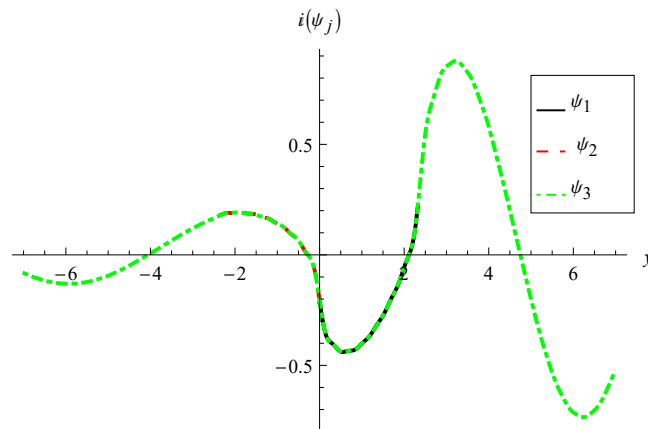
FIGURE 2.4: Transmitted energy (\mathcal{E}_3) versus frequency (f) with RR conditions in \mathcal{R}_1 and \mathcal{R}_2 , and RI , RR and RS conditions in \mathcal{R}_3 (a) with step-discontinuous ($a \neq b$) (b) without step-discontinuous ($a = b$), where $\bar{a} = 0.24m$, $\bar{b} = 3\bar{a}$ and $N = 10$.

Figures 2.4(a) and 2.4(b) are plotted to observe the behavior of the transmitted energy (\mathcal{E}_3) by varying the frequency by letting $\bar{a} = 0.24m$ and $\bar{b} = 3\bar{a}$. More fluctuations in transmitted energy (for all impedance, rigid and soft cases) are noticed for discontinuous case when compared results in the absence of step-discontinuities. We see that the transmitted energy increases remarkably by increasing the frequency regime. Further, in Figure 2.4(b), it is observed that at certain level of

frequency in regime, say ($1Hz - 180Hz$), the curve pattern of the transmitted energy (for all impedance, rigid and soft case) is quite smooth. It is also noticed that the transmitted field coefficient is maximum at certain cut-on frequencies of different regions.



(a)



(b)

FIGURE 2.5: The real (a) and imaginary (b) parts of pressures against duct heights, at interface, with step-discontinuities and rigid-impedance boundaries, where, $\bar{a} = 0.24m$, $\bar{b} = 3\bar{a}$ and $N = 80$.

Figures 2.5 and 2.6 show that the real and imaginary parts of pressures and normal velocities conditions exactly coincide in their respective regions. As a result, the normal velocities and pressure matching conditions are entirely satisfied. It is useful to reconstruct the matching conditions by using the truncated form of MM solution.

It confirms the accuracy of performed algebra and validates the truncated solution as well.

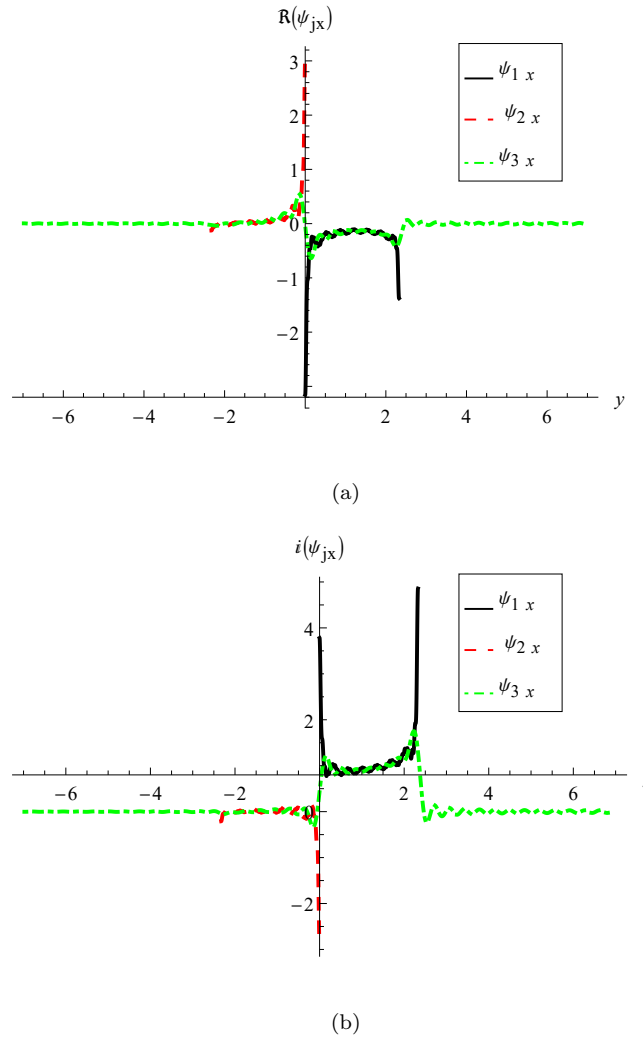


FIGURE 2.6: The real (a) and imaginary (b) parts of normal velocities against duct heights, at interface, with step-discontinuities and RI boundaries, where, $\bar{a} = 0.24m$, $\bar{b} = 3\bar{a}$ and $N = 80$.

Furthermore, the radiated energies \mathcal{E}_i ; $i = 1, 2, 3$, in different duct regions of the bifurcated duct against the variation of frequency (f) are presented in tabular form (2.1 – 2.6). To collect the data of all of these tables, the dimensional variables are fixed as: $\bar{a} = 0.24m$ and $\bar{b} = 3\bar{a}$, for discontinuous case and $\bar{a} = \bar{b} = 0.24m$ for continuous case respectively.

A brief description of the power propagating in different duct regions, \mathcal{R}_j ; $j = 1, 2, 3$ for RI, RR and RS cases with discontinuous and continuous waveguide of

the bifurcated duct is presented in tabular form (see Tables : 2.3–2.8) for different frequencies. It is observed that the scattering components converge appropriately whereas overall sum remains unity.

The RI case with discontinuous and planar waveguides of the bifurcated duct is presented in Tables 2.3 and 2.4, respectively. The scattering energies converge up to two and three decimal places, as can be observed. Moreover, the sum of reflected energies (\mathcal{E}_1 and \mathcal{E}_2) and transmitted energy (\mathcal{E}_3) remains unity for different values of f .

TABLE 2.3: Discontinuous bifurcated waveguide for RI case, when $\bar{a} = 0.24m$ and $\bar{b} = 3\bar{a}$ by varying frequency

f	\mathcal{E}_1	\mathcal{E}_2	\mathcal{E}_3	$\mathcal{E}_T = 1$
10	0.980163	0.0198368	0	1
100	0.393622	0.139772	0.466606	1
160	0.448309	0.109522	0.442169	1
220	0.350381	0.0551765	0.594442	1
310	0.156048	0.256548	0.587405	1
400	0.244699	0.193833	0.561468	1
550	0.0688701	0.0377801	0.89335	1
640	0.125583	0.0998704	0.774547	1
700	0.00934893	0.00614507	0.984506	1
745	0.0110413	0.0323672	0.956591	1

Likewise, the results for the reflected powers in inlet (\mathcal{E}_1 and \mathcal{E}_2) and the transmitted power in outlet (\mathcal{E}_3) for RR case with discontinuous and planar waveguide for different values of frequencies are shown in Table 2.5 and Table 2.6.

Note that the sum of scattering energies for different values of f remain unity. It clearly, authenticates the accuracy of algebra for both discontinuous (Table 2.5) and planar (Table 2.6) configurations of the RR waveguide structure.

It essentially referred to the conservation of energies when no dissipation is involved.

Similarly, Table 2.7 and Table 2.8 present the scattering analysis for different values of frequencies that how power law of conservation hold for RS case with discontinuous and continuous waveguide respectively.

It is shown that total energy remains conserved in both cases.

TABLE 2.4: Continuous bifurcated waveguide for RI case, when $\bar{a} = \bar{b} = 0.24m$ by varying frequency

f	\mathcal{E}_1	\mathcal{E}_2	\mathcal{E}_3	$\mathcal{E}_T = 1$
10	0.962846	0.0371539	0	1
100	0.67269	0.32731	0	1
160	0.36999	0.63001	0	1
220	0.158805	0.404238	0.436957	1
310	0.225228	0.289083	0.485689	1
400	0.256406	0.249296	0.494298	1
550	0.126498	0.0863152	0.787186	1
640	0.0296258	0.0156923	0.954682	1
700	0.0151364	0.00771409	0.977149	1
745	0.0212139	0.034907	0.943879	1

TABLE 2.5: Discontinuous bifurcated waveguide for RR case, when $\bar{a} = 0.24m$ and $\bar{b} = 3\bar{a}$ by varying frequency

f	\mathcal{E}_1	\mathcal{E}_2	\mathcal{E}_3	$\mathcal{E}_T = 1$
10	0.5626	0.0624869	0.374913	1
100	0.57464	0.0603541	0.365006	1
160	0.520582	0.0553577	0.42406	1
220	0.522984	0.179017	0.297999	1
310	0.251143	0.208358	0.540498	1
400	0.0662835	0.0203184	0.913398	1
550	0.123822	0.0983298	0.777849	1
640	0.0116479	0.00662039	0.981732	1
700	0.00967206	0.00535226	0.984976	1
745	0.0195783	0.0328495	0.947572	1

TABLE 2.6: Continuous bifurcated waveguide for RR case, when $\bar{a} = \bar{b} = 0.24m$ by varying frequency

f	\mathcal{E}_1	\mathcal{E}_2	\mathcal{E}_3	$\mathcal{E}_T = 1$
10	0.2	0.25	0.5	1
100	0.2	0.25	0.5	1
160	0.2	0.25	0.5	1
220	0.2	0.25	0.5	1
310	0.2	0.25	0.5	1
400	0.0362895	0.0362895	0.927421	1
550	0.00458072	0.00458072	0.990839	1
640	0.00211769	0.00211769	0.995765	1
700	0.00137444	0.00137444	0.997251	1
745	0.0212272	0.0212272	0.957546	1

TABLE 2.7: Discontinuous bifurcated waveguide for RS case, when $\bar{a} = 0.24m$ and $\bar{b} = 3\bar{a}$ by varying frequency

f	\mathcal{E}_1	\mathcal{E}_2	\mathcal{E}_3	$\mathcal{E}_T = 1$
10	0.998134	0.00186597	0	1
100	0.650637	0.349363	0	1
160	0.292124	0.211985	0.495891	1
220	0.363176	0.158174	0.47865	1
310	0.267136	0.0467276	0.686136	1
400	0.170069	0.166125	0.663806	1
550	0.0266363	0.0116339	0.96173	1
640	0.0469763	0.0298466	0.923177	1
700	0.0902981	0.071982	0.83772	1
745	0.0149262	0.034464	0.95061	1

TABLE 2.8: Continuous bifurcated waveguide for RS case, when $\bar{a} = \bar{b} = 0.24m$ by varying frequency

f	\mathcal{E}_1	\mathcal{E}_2	\mathcal{E}_3	$\mathcal{E}_T = 1$
10	0.999902	0.0000976237	0	1
100	0.989676	0.0103239	0	1
160	0.970949	0.0290514	0	1
220	0.935796	0.0642042	0	1
310	0.800592	0.199408	0	1
400	0.284239	0.28834	0.427421	1
550	0.302974	0.206187	0.490839	1
640	0.298056	0.20618	0.495765	1
700	0.276693	0.226056	0.497251	1
745	0.100329	0.0988936	0.800777	1

Chapter 3

Trifurcated Waveguide Scattering Analysis with Structural Discontinuities

A trifurcated boundary value problem is presented in this chapter. This problem comprises of waveguide whose boundary walls are considered to be either rigid or soft in the presence of discontinuous waveguide structure. The purpose behind this chapter is to formulate a boundary value problem with structural discontinuities for RR and RS boundaries and obtain the solution by MM technique.

3.1 Mathematical Formulation

To formulate the boundary value problem, we consider an infinitely stretched trifurcated waveguide occupying the regions

$$\mathcal{R}_1 := \{\bar{x} < \bar{0}, -\bar{a} \leq \bar{y} \leq \bar{a}\}, \quad \mathcal{R}_2 := \{\bar{x} < \bar{0}, -\bar{b} \leq \bar{y} \leq -\bar{a}\},$$

$$\mathcal{R}_3 := \{\bar{x} < \bar{0}, \bar{a} \leq \bar{y} \leq \bar{b}\}, \quad \text{and} \quad \mathcal{R}_4 := \{\bar{x} > \bar{0}, -\bar{h} \leq \bar{y} \leq \bar{h}\},$$

where the dimensional setting of coordinates is shown by the over-bar.

On the interior, these regions are filled with compressible fluid that has a density of ρ and a sound speed of c . The bounding wall conditions of the region may vary; (a) each of the region $\mathcal{R}_j, j = 1, 2, 3, 4$ is bounded by acoustically rigid boundaries, and

(b) the regions \mathcal{R}_2 and \mathcal{R}_3 comprise soft boundaries at $\bar{y} = \pm\bar{b}$.

The outside of these waveguide is set into *vacou*. At $\bar{x} = 0$, there lies two rigid vertical step discontinuities aligned along with $-\bar{h} \leq \bar{y} \leq -\bar{b}$ and $\bar{b} \leq \bar{y} \leq \bar{h}$.

Figure 3.1 depicts the physical layout of the problem as follows:

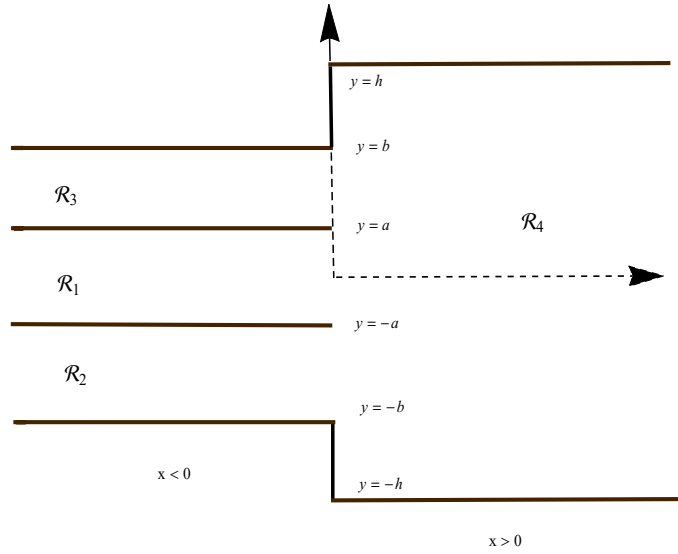


FIGURE 3.1: Geometry of the proposed model.

Consider an incident wave with time-harmonic dependence travelling in the direction of \mathcal{R}_1 from negative x -direction to $\bar{x} = 0$. It will scatter into an infinite number of reflected and transmitted modes when $\bar{x} = 0$. The dimensional field potentials that characterize the scattering fields in different duct regions may be written as:

$$\bar{\psi}(\bar{x}, \bar{y}) = \begin{cases} \bar{\psi}_1(\bar{x}, \bar{y}), & (\bar{x}, \bar{y}) \in \mathcal{R}_1, \\ \bar{\psi}_2(\bar{x}, \bar{y}), & (\bar{x}, \bar{y}) \in \mathcal{R}_2, \\ \bar{\psi}_3(\bar{x}, \bar{y}), & (\bar{x}, \bar{y}) \in \mathcal{R}_3, \\ \bar{\psi}_4(\bar{x}, \bar{y}), & (\bar{x}, \bar{y}) \in \mathcal{R}_4. \end{cases} \quad (3.1)$$

Now, we presume the harmonic time dependence of $e^{-i\omega\bar{t}}$ in which $\omega = ck$ is the angular frequency and $k = 2\pi f/c$ is the wave number with frequency f .

Under the transformations

$$x = k\bar{x}, \quad y = k\bar{y} \quad \text{and} \quad t = \omega\bar{t},$$

the boundary value problem is non-dimensionalized with respect to the length scale k^{-1} and the time scale ω^{-1} .

Thus, the Helmholtz equation is satisfied by the dimensionless fluid velocity potential $\psi(x, y)$

$$(\nabla^2 + 1) \psi(x, y) = 0. \tag{3.2}$$

In all of the above regions, the dimensionless form of rigid boundary conditions are:

$$\frac{\partial\psi_1}{\partial y} = 0, \quad y = \pm a, \quad x < 0, \tag{3.3}$$

$$\frac{\partial\psi_2}{\partial y} = 0, \quad y = -b, -a, \quad x < 0, \tag{3.4}$$

$$\frac{\partial\psi_3}{\partial y} = 0, \quad y = a, b, \quad x < 0, \tag{3.5}$$

$$\frac{\partial\psi_4}{\partial y} = 0, \quad y = \pm h, \quad x > 0, \tag{3.6}$$

$$\frac{\partial\psi_4}{\partial x} = 0, \quad x = 0, \quad \text{for} \quad -h \leq y \leq -b \quad \text{and} \quad b \leq y \leq h. \tag{3.7}$$

Here, (3.7) represents the rigid conditions for two vertical step discontinuities.

However, the acoustically soft wall condition for \mathcal{R}_2 and \mathcal{R}_3 are

$$\psi_2 = 0, \quad y = -b, \quad x < 0, \tag{3.8}$$

$$\psi_3 = 0, \quad y = b, \quad x < 0. \tag{3.9}$$

Furthermore, the continuity conditions of pressure and velocity at the interface are

$$\psi_2 = \psi_4, \quad x = 0, \quad -b \leq y \leq -a, \tag{3.10}$$

$$\psi_1 = \psi_4, \quad x = 0, \quad -a \leq y \leq a, \quad (3.11)$$

$$\psi_3 = \psi_4, \quad x = 0, \quad a \leq y \leq b, \quad (3.12)$$

and

$$\psi_{4x} = \begin{cases} 0 & x = 0, & -h \leq y < -b, \\ \psi_{2x} & x = 0, & -b \leq y \leq -a, \\ \psi_{1x} & x = 0, & -a \leq y \leq a, \\ \psi_{3x} & x = 0, & a \leq y \leq b, \\ 0 & x = 0, & b \leq y < h. \end{cases} \quad (3.13)$$

The subscript x here denotes differentiation with respect to x .

The MM technique is used to tackle the boundary value problem in the next section.

3.2 Mode-matching Solution

To use the MM technique to solve the boundary value problem, firstly we determine the eigenfunction expansions and orthogonality criteria in each duct section.

These can be found in various duct regions as

- Region $\mathcal{R}_1 := \{x < 0, \quad -a \leq y \leq a\}$

In this region, (3.2) and (3.3) yields the eigen expansion form of field potential as:

$$\psi_1(x, y) = e^{ix} + \sum_{n=0}^{\infty} A_n \cos[\tau_n(y + a)]e^{-i\eta_n x}. \quad (3.14)$$

The quantity $\eta_n = \sqrt{1 - \tau_n^2}$ is the n^{th} reflected mode wave number, where τ_n ; $n = 0, 1, 2, \dots$ are the eigenvalues, which fulfill the dispersion relation

$$\sin[2\tau_n a] = 0, \quad \text{for } n = 0, 1, 2, \dots \quad (3.15)$$

The orthogonality relation is satisfied by the respective eigenfunctions $\cos[\tau_n(y + a)]$, $n = 0, 1, 2, \dots$

$$\int_{-a}^a \cos[\tau_m(y + a)] \cos[\tau_n(y + a)] dy = \epsilon_m a \delta_{mn}, \quad (3.16)$$

where $\epsilon_m = 2$ for $m = 0$ and 1 otherwise, and δ_{mn} is Kronecker delta.

The incident wave is represented by the first term in (3.14), while the reflected field is given by the second term, in which A_n , $n = 0, 1, 2, \dots$ are the reflected mode coefficients and are unknowns. These unknowns will be found later through the use of matching conditions.

- Region $\mathcal{R}_2 := \{x < 0, \quad -b \leq y \leq -a\}$

From (3.2), (3.4) and (3.8), the eigen expansion form is obtained as:

$$\psi_2(x, y) = \sum_{n=0}^{\infty} B_n \cos[\xi_n(y + a)] e^{-i\nu_n x}, \quad (3.17)$$

where $\nu_n = \sqrt{1 - \xi_n^2}$ is the n^{th} reflected mode wave number, wherein ξ_n , $n = 0, 1, 2, \dots$ are the eigenvalues.

These satisfy the dispersion relation for rigid boundary conditions at $y = -b$

$$\sin[\xi_n(b - a)] = 0, \text{ for } n = 0, 1, 2, \dots \quad (3.18)$$

However, for soft boundary condition at $y = -b$, these satisfy

$$\cos[\xi_n(b - a)] = 0, \text{ for } n = 0, 1, 2, \dots \quad (3.19)$$

The analogous eigenfunctions $\cos[\xi_n(y + a)]$, $n = 0, 1, 2, \dots$ satisfy the orthogonality relation

$$\int_{-b}^{-a} \cos[\xi_m(y + a)] \cos[\xi_n(y + a)] dy = \frac{\Theta(\xi_n)(b - a)\delta_{mn}}{2}, \quad (3.20)$$

where

$$\Theta(\xi_n) = \begin{cases} \varepsilon_n, & \text{for } \xi_n = \frac{n\pi}{b-a} : n = 0, 1, 2, \dots \\ 1, & \text{for } \xi_n = \frac{(2n+1)\pi}{2(b-a)} : n = 0, 1, 2, \dots \end{cases} \quad (3.21)$$

- **Region** $\mathcal{R}_3 := \{x < 0, \quad a \leq y \leq b\}$

From (3.2), (3.5) and (3.9), the eigen expansion form is found to be as:

$$\psi_3(x, y) = \sum_{n=0}^{\infty} C_n \cos[\lambda_n(y-a)] e^{-i\kappa_n x}, \quad (3.22)$$

where, $\kappa_n = \sqrt{1 - \lambda_n^2}$ is the wave number of the n^{th} reflected mode and λ_n ; $n = 0, 1, 2, \dots$ are the eigenvalues. For rigid surface at $y = b$, these eigenvalues satisfy the dispersion relation

$$\sin[\lambda_n(b-a)] = 0, \quad \text{for } n = 0, 1, 2, \dots \quad (3.23)$$

whereas, for the soft surface at $y = b$ these satisfy

$$\cos[\lambda_n(b-a)] = 0, \quad \text{for } n = 0, 1, 2, \dots \quad (3.24)$$

The eigenfunctions $\cos[\lambda_n(y-a)]$; $n = 0, 1, 2, \dots$ are orthogonal and assure the usual orthogonality relation

$$\int_a^b \cos[\lambda_m(y-a)] \cos[\lambda_n(y-a)] dy = \frac{\Theta(\lambda_n)(b-a)\delta_{mn}}{2}. \quad (3.25)$$

- **Region** $\mathcal{R}_4 := \{x > 0, \quad -h \leq y \leq h\}$

From (3.2) and (3.6), the eigen expansion form of transmitted field is revealed as:

$$\psi_4(x, y) = \sum_{n=0}^{\infty} D_n \cos[\gamma_n(y+h)] e^{i\kappa_n x}, \quad (3.26)$$

where, $s_n = \sqrt{1 - \gamma_n^2}$ is the wave number of n^{th} transmitted mode and γ_n ; $n = 0, 1, 2, \dots$ are the eigenvalues which fulfil the dispersion relation

$$\sin[2\gamma_n h] = 0, \text{ for } n = 0, 1, 2, \dots \quad (3.27)$$

The related eigenfunctions $\cos[\gamma_n(y + h)]$; $n = 0, 1, 2, \dots$ satisfy the orthogonality relation:

$$\int_{-h}^h \cos[\gamma_m(y + h)] \cos[\gamma_n(y + h)] dy = h \epsilon_m \delta_{mn}. \quad (3.28)$$

Now, the unknown coefficients $\{A_n, B_n, C_n, D_n\}$ $n = 0, 1, 2, \dots$ are calculated by applying the matching conditions (3.11)-(3.13).

On using (3.14) and (3.26) in (3.11), we get

$$1 + \sum_{n=0}^{\infty} A_n \cos[\tau_n(y + a)] = \sum_{n=0}^{\infty} D_n \cos[\gamma_n(y + h)]. \quad (3.29)$$

On multiplying (3.29) with $\cos[\tau_m(y + a)]$, integrating from $-a$ to a and then applying the orthogonality relation (3.16), we found

$$A_m = -\delta_{m0} + \frac{1}{a \epsilon_m} \sum_{n=0}^{\infty} D_n R_{mn}, \quad (3.30)$$

where

$$R_{mn} = \begin{cases} 2a \delta_{mn} & n = 0, m = 0, 1, 2, \dots \\ \frac{\gamma_n}{\tau_m^2 - \gamma_n^2} E_{mn} & n \neq 0, m = 0, 1, 2, \dots \end{cases} \quad (3.31)$$

$$E_{mn} = (-1)^{m+1} \sin[(a + h)\gamma_n] - \sin[(a - h)\gamma_n]. \quad (3.32)$$

On using (3.17) and (3.26) in (3.10), we get

$$\sum_{n=0}^{\infty} B_n \cos[\xi_n(y + a)] = \sum_{n=0}^{\infty} D_n \cos[\gamma_n(y + h)]. \quad (3.33)$$

On multiplying (3.33) with $\cos[\xi_m(y + a)]$, integrating the result from $-b$ to $-a$ and afterwards using the OR (3.20), we get

$$B_m = \frac{2}{(b - a)\Theta(\xi_m)} \sum_{n=0}^{\infty} D_n P_{mn}. \quad (3.34)$$

For all rigid-rigid cases:

$$P_{mn} = \begin{cases} \delta_{mn}(b-a) & n = 0, m = 0, 1, 2, \dots \\ \frac{\gamma_n}{m^2\pi^2} F_{mn} & n \neq 0, m = 0, 1, 2, \dots \\ \frac{1}{(b-a)^2 - \gamma_n^2} & \end{cases} \quad (3.35)$$

where

$$F_{mn} = (-1)^{m+1} \sin[(h-a)\gamma_n] + \sin[(h-b)\gamma_n]. \quad (3.36)$$

For all rigid-soft cases:

$$P_{mn} = \begin{cases} \frac{2(b-a)}{\pi} & n = 0, m = 0, 1, 2, \dots \\ \frac{1}{(2m+1)^2\pi^2} G_{mn} & n \neq 0, m = 0, 1, 2, \dots \\ \frac{1}{4(b-a)^2 - \gamma_n^2} & \end{cases} \quad (3.37)$$

where

$$G_{mn} = (-1)^{m+1} \gamma_n \sin[(h-a)\gamma_n] + \frac{(2m+1)\pi}{2(b-a)} \cos[(h-b)\gamma_n]. \quad (3.38)$$

On using (3.22) and (3.26) into (3.12), we get

$$\sum_{n=0}^{\infty} C_n \cos[\lambda_n(y-a)] = \sum_{n=0}^{\infty} D_n \cos[\gamma_n(y+h)]. \quad (3.39)$$

On multiplying (3.39) with $\cos[\lambda_m(y-a)]$, integrating the result from a to b and afterwards imposing the orthogonality relation (3.25), we get

$$C_m = \frac{2}{(b-a)\Theta(\lambda_m)} \sum_{n=0}^{\infty} D_n Q_{mn}. \quad (3.40)$$

For all rigid-rigid cases:

$$Q_{mn} = \begin{cases} \delta_{mn}(b-a) & n = 0, m = 0, 1, 2, \dots \\ \frac{\gamma_n}{m^2\pi^2} H_{mn} & n \neq 0, m = 0, 1, 2, \dots \\ \frac{1}{(b-a)^2 - \gamma_n^2} & \end{cases} \quad (3.41)$$

where

$$H_{mn} = (-1)^{m+1} \sin[(b+h)\gamma_n] + \sin[(a+h)\gamma_n]. \quad (3.42)$$

For all rigid-soft cases:

$$Q_{mn} = \begin{cases} \frac{2(b-a)}{\pi} & n = 0, m = 0, 1, 2, \dots \\ \frac{1}{\frac{(2m+1)^2\pi^2}{4(b-a)^2} - \gamma_n^2} I_{mn} & n \neq 0, m = 0, 1, 2, \dots \end{cases} \quad (3.43)$$

where

$$I_{mn} = (-1)^{m+1} \frac{(2m+1)\pi}{2(b-a)} \cos[(b+h)\gamma_n] + \gamma_n \sin[(a+h)\gamma_n]. \quad (3.44)$$

Now, to determine the transmitted modes coefficients, we use (3.17), (3.14), (3.22) and (3.26) into (3.13) to obtain

$$\sum_{n=0}^{\infty} D_n s_n \cos[\gamma_n(y+h)] = \begin{cases} 0, & -h \leq y < -b, \\ -\sum_{n=0}^{\infty} B_n v_n \cos[\xi_n(y+a)], & -b \leq y < -a, \\ 1 - \sum_{n=0}^{\infty} A_n \eta_n \cos[\tau_n(y+a)], & -a \leq y < a, \\ -\sum_{n=0}^{\infty} C_n \varkappa_n \cos[\lambda_n(y-a)], & a \leq y < b, \\ 0, & b \leq y \leq h. \end{cases} \quad (3.45)$$

After multiplying with $\cos[\gamma_m(y+h)]$, integrating from $-h$ to h , and lastly using the orthogonality relation (3.45), we get

$$D_m = \frac{R_{0m}}{s_m \epsilon_m h} - \frac{1}{s_m \epsilon_m h} \sum_{n=0}^{\infty} A_n \eta_n R_{nm} - \frac{1}{s_m \epsilon_m h} \sum_{n=0}^{\infty} B_n v_n P_{nm} - \frac{1}{s_m \epsilon_m h} \sum_{n=0}^{\infty} C_n \varkappa_n Q_{nm}. \quad (3.46)$$

Now, by means of (3.30), (3.34) and (3.40), it is straightforward to obtain (3.46) in terms of unknown $D_m, m = 0, 1, 2, \dots$, that is:

$$D_m s_m \epsilon_m h + \sum_{n=0}^{\infty} \sum_{p=0}^{\infty} \frac{D_p \eta_n R_{np} R_{nm}}{\epsilon_n a} + \sum_{n=0}^{\infty} \sum_{q=0}^{\infty} \frac{2D_q v_n P_{nq} P_{nm}}{(b-a)\Theta(\xi_n)} + \sum_{n=0}^{\infty} \sum_{l=0}^{\infty} \frac{2D_l \varkappa_n Q_{nl} Q_{nm}}{(b-a)\Theta(\lambda_m)} = 2R_{0m}. \quad (3.47)$$

In this manner, (3.47) leads to a set of infinite equations in which the unknown are $D_m; m = 0, 1, 2, \dots$. To find the unknown modal coefficients, these are truncated and inverted. Once obtained $D_m; m = 0, 1, 2, \dots$, the quantities $\{A_m, B_m, C_m\}; m = 0, 1, 2, \dots$ are found easily by using (3.30), (3.34) and (3.40).

3.3 Energy Balance

The energy flux/power inside the duct regions in terms of dimensionless time harmonic fluid velocity potential is defined by

$$\frac{\partial \mathcal{E}}{\partial t} = \frac{1}{2} Re \left\{ i \int_{\Omega} \psi \left(\frac{\partial \psi}{\partial x} \right)^* dy \right\}, \quad (3.48)$$

where, superscript asterisk (*) denotes the complex conjugate. From the definition of energy flux/power, the incident power is found to be $\mathcal{P}_{inc} = a$. Likewise, the power/energy flux components in duct region $\mathcal{R}_j; j = 1, 2, 3, 4$ are:

$$\mathcal{P}_1 = \frac{1}{2} Re \left\{ \sum_{n=0}^{\infty} |A_n|^2 \eta_n \epsilon_n \right\}, \quad (3.49)$$

$$\mathcal{P}_2 = \frac{b-a}{4a} Re \left\{ \sum_{n=0}^{\infty} |B_n|^2 v_n \Theta(\xi_n) \right\}, \quad (3.50)$$

$$\mathcal{P}_3 = \frac{b-a}{4a} Re \left\{ \sum_{n=0}^{\infty} |C_n|^2 \varkappa_n \Theta(\lambda_n) \right\}, \quad (3.51)$$

and

$$\mathcal{P}_4 = \frac{h}{2a} Re \left\{ \sum_{n=0}^{\infty} |D_n|^2 s_n \epsilon_n \right\}. \quad (3.52)$$

It's significant to mention that the generated power into the system equals the sum of scattering powers in different duct regions, that is:

$$\mathcal{P}_{inc} = \mathcal{P}_1 + \mathcal{P}_2 + \mathcal{P}_3 + \mathcal{P}_4, \quad (3.53)$$

which is conserved power identity. We can scale the incident power to unity for analysis purposes. For this, we divide (3.53) by a to get

$$\mathcal{E}_T = \sum_{j=1}^4 \mathcal{E}_j,$$

where

$$\mathcal{E}_j = \mathcal{P}_j/a; \quad j = 1, 2, 3, 4,$$

denote the power/energy flux components in duct regions R_j ; $j = 1, 2, 3, 4$ for which the incident power is being scaled at unity.

3.4 Numerical Results and Discussions

To discuss the radiated energy flux/power in duct regions and to reconstruct the matching conditions at interface, we truncate the system of equations defined by (3.47) up to N terms and then solve the retained system numerically.

Here, two types of bounding wall conditions for various duct sections R_j , $j = 1, 2, 3, 4$ are assumed:

- (a) all are acoustically rigid (Figures 3.2 – 3.5(a)),
- (b) rigid-soft for R_2 and R_3 only (Figures 3.2 – 3.5(b)).

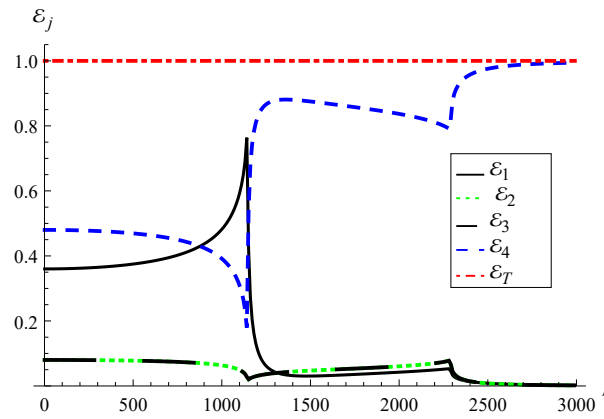
For numerical computations the compressible fluid of density (air) $\rho = 1.2043kgm^{-3}$ sound speed $c = 343ms^{-1}$ are taken from Kaye and Laby [68].

The radiated power in different duct regions against frequency from $1Hz$ to $3000Hz$ is shown in Figure 3.2.

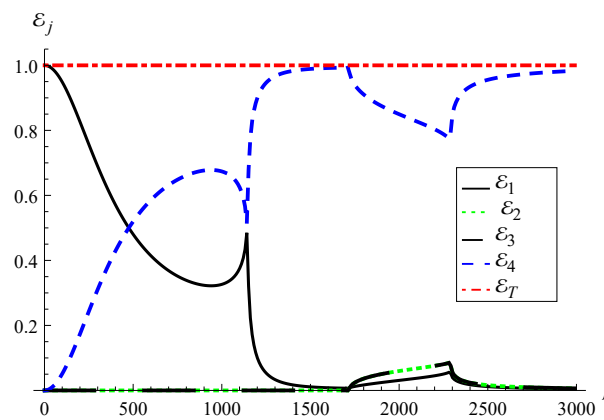
The considered configuration comprises structural discontinuities at interface and fixed dimensions: $\bar{a} = 0.05m$, $\bar{b} = 0.1m$ and $\bar{h} = 0.15m$.

Note that, the radiated energy against frequency depicted in Figure 3.2 contains sharp edges and the variation in radiated energy is more noticeable before and after these edges. These edges basically specify the cut-on position of duct modes.

For the structural discontinuities case along with rigid bounding characteristics (Figure 3.2(a)), the two duct modes are cut-on at $f = 1441Hz$ and $f = 2281Hz$. However for the rigid-soft case (Figure 3.2(b)), three modes are cut-on at $f = 1441Hz$, $f = 1711Hz$ and $f = 2281Hz$. The more manifest radiated energy is of region R_1 and R_4 .



(a)



(b)

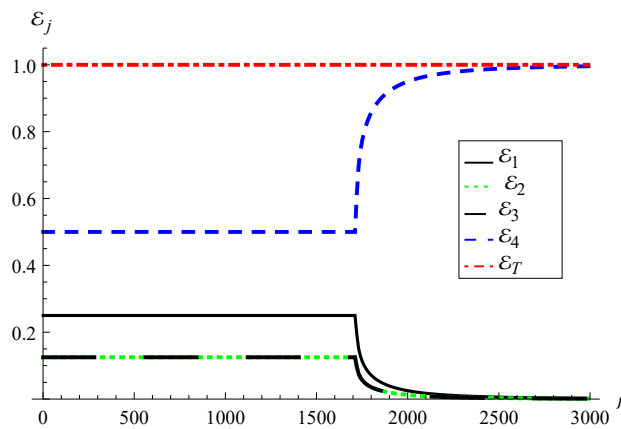
FIGURE 3.2: The energy flux/power components against frequency in discontinuous waveguide, with (a) rigid-rigid (b) rigid-soft boundaries, where, $\bar{a} = 0.05m$, $\bar{b} = 0.1m$, $\bar{h} = 0.15m$ and $N = 10$.

For rigid case (Figure 3.2(a)), by increasing frequency, the energy flux in R_4 decreases, and which goes to its maximum at cut-on limit of the next duct mode. But once the next, and so on higher modes start propagating, this power varies inversely to its highest and, vice versa for energy flux in R_1 .

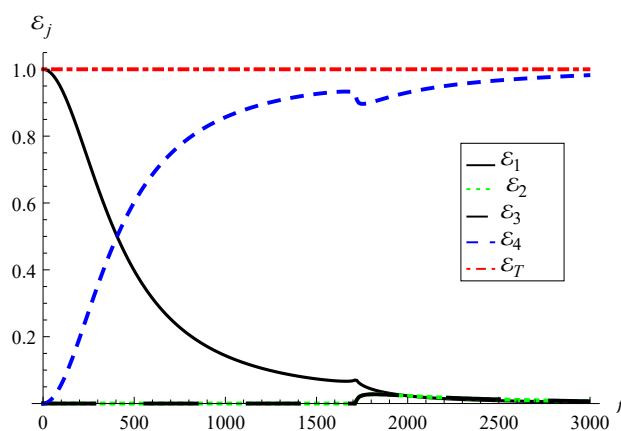
However, in later rigid-soft case (Figure 3.2(b)), this behavior is opposite upto the first cut-on point, while remains similar to previous case for higher order modes.

In the next Figure 3.3, we assume the planar waveguide configuration (without structural discontinuity) by taking $\bar{a} = 0.05m$ and $\bar{b} = \bar{h} = 0.1m$.

Note that, only the first duct mode is cut-on at $f = 1711Hz$ in given regime for both rigid (Figure 3.3(a)) and rigid-soft (Figure 3.3(b)) bounding properties.



(a)



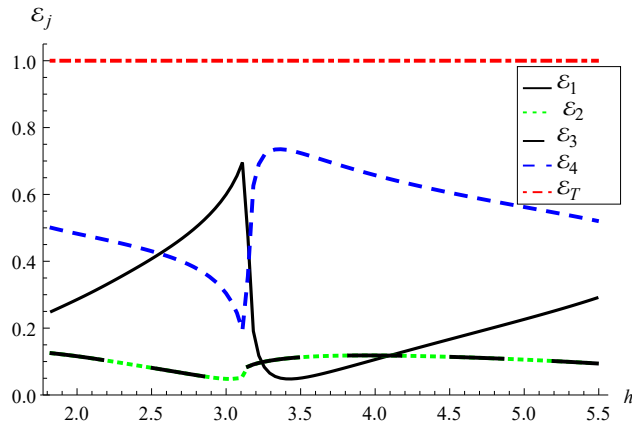
(b)

FIGURE 3.3: The energy flux/power components against frequency in planer waveguide, with (a) rigid-rigid (b) rigid-soft boundaries, where, $\bar{a} = 0.05m$, $\bar{b} = 0.1m$, $\bar{h} = 0.15m$ and $N = 10$.

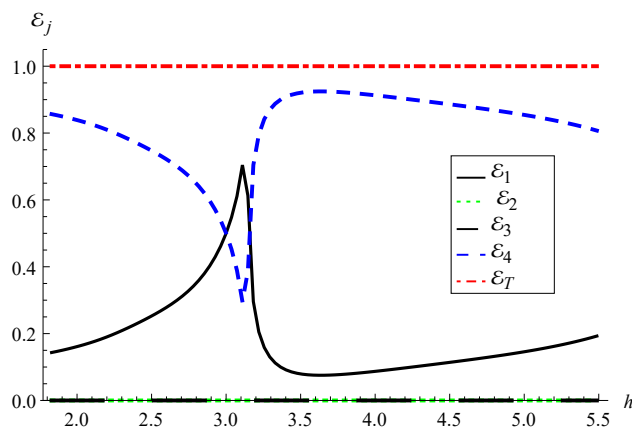
In rigid case, the radiated power in different duct regions remain constant against frequency upto their first cut-on and then goes to its largest (see Figure 3.3(a)). But in the rigid-soft case, the energy radiated in regions R_1 and R_4 varies inversely.

Figure 3.4 depicts the effect of symmetric height discontinuity on radiated energy. For the fixed frequency $f = 1000Hz$ and dimensions $\bar{a} = 0.05m$, $\bar{b} = 0.1m$, the dimensionless height discontinuity $h = k \times \bar{h}$ is changed symmetrically from $\bar{h} = \bar{b}$ to $\bar{h} = 0.2m$.

The first duct mode is cut-on at $k \times \bar{h} \approx 3.11$, while the other cut-on modes are beyond the chosen domain.



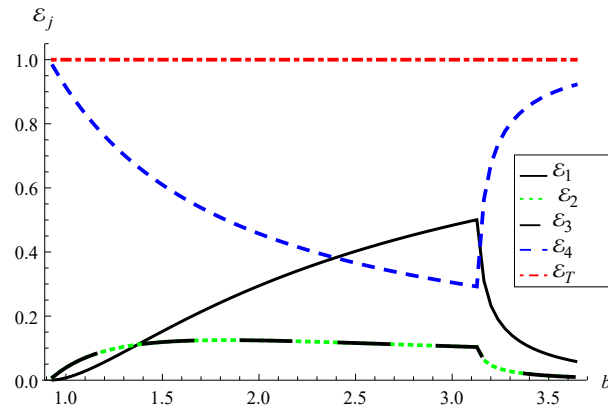
(a)



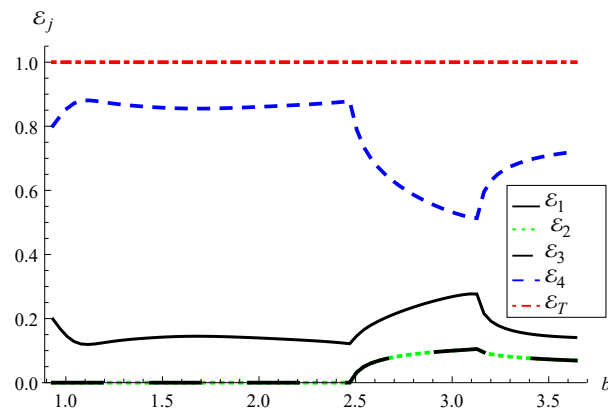
(b)

FIGURE 3.4: The energy flux/power components against height discontinuities h , for (a) rigid-rigid (b) rigid-soft boundaries, where, $\bar{a} = 0.05m$, $\bar{b} = 0.1m$ and $N = 10$.

From Figure 3.4, it is noted that the variation in height discontinuity significantly affects the reflection in R_1 and transmission in R_4 , for both rigid case and rigid-soft case. There is no radiated power in R_2 and R_3 for rigid-soft setting, which is consistent with the transmission loss in these regions.



(a)



(b)

FIGURE 3.5: The energy flux/power components against b , for (a) rigid-rigid (b) rigid-soft boundaries, where, $\bar{a} = 0.05m$, $\bar{h} = \bar{b}$ and $N = 10$

Figure 3.5 shows the radiated energy in the planar waveguide against the size of the regions R_2 , R_3 and R_4 . In symmetrical setting, the vertical dimensions of the regions containing incident wave is fixed at $\bar{a} = 0.05m$ and $\bar{b} = \bar{h}$.

Now, on changing the non-dimensional height $b = k \times \bar{b}$, for $0.1m \leq \bar{b} \leq 0.15m$, the size of regions R_2 , R_3 and R_4 is changed while frequency remain fixed at $f = 1000Hz$. The cut-on duct mode for the rigid case occurs at $k \times \bar{b} \approx 3.13m$ (see Figure 3.5(a)) whilst for the rigid-soft case two cut-on duct modes exist at

$k \times \bar{b} \approx 2.18m$ and $k \times \bar{b} \approx 3.13m$ (see Figure 3.5(b)). From Figure 3.5, it is clear that the change in size of the duct regions significantly affect the radiated energy of these regions. By comparing all these four graphs, it is obvious that geometric discontinuity and change of material properties have a significant impact on the radiated energy duct modes, which are more noticeable in low frequency regime 5Hz-1200Hz. Moreover, from the geometric symmetry assumed in problems about $y = 0$, the region R_2 becomes symmetric to R_3 . Therefore, the reflected power R_2 as depicted in Figures 3.2 – 3.5, overlaps to the power reflected in R_3 . Nevertheless, this might reduced the algebra, if we consider it to two layered duct comprising only of regions R_1 and R_3 but as we have studied the trifurcated waveguide problem, so it is necessary to use R_2 region as well with R_1 and R_3 . Now, the continuity conditions of normal velocity and pressure are pieced together at interface to validate the truncated solution.

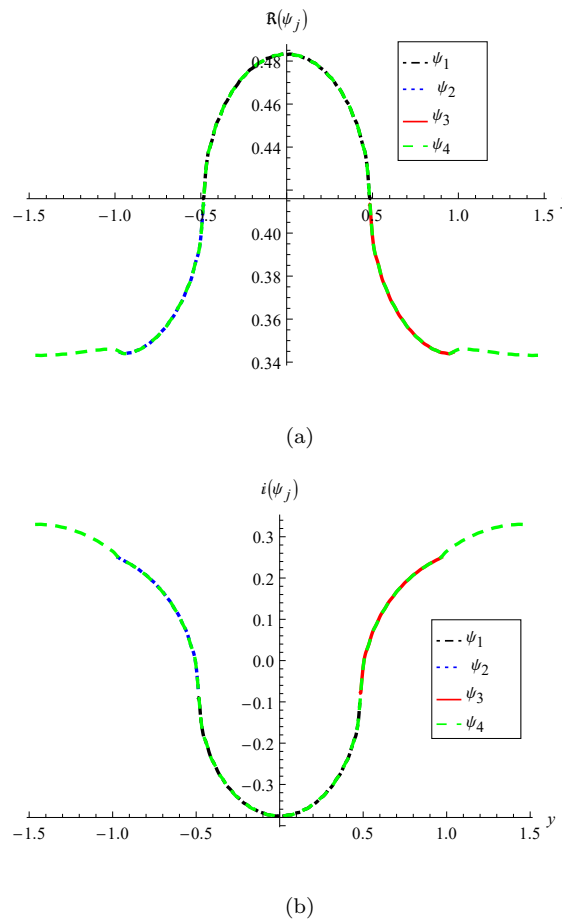


FIGURE 3.6: The real (a) and imaginary (b) parts of pressures against duct heights, at interface, with step-discontinuities and rigid-rigid boundaries, where, $\bar{a} = 0.05m$, $\bar{b} = 0.1m$, $\bar{h} = 0.15m$ and $N = 80$.

Only the results for all rigid setting of waveguide along with height discontinuities are shown in Figures 3.6 and 3.7. The vertical dimensions of symmetric waveguide, are fixed at $\bar{a} = 0.05m$, $\bar{b} = 0.1m$ and $\bar{h} = 0.15m$. At frequency $f = 1000Hz$ the real (\Re) and imaginary (\Im) parts of non-dimensional pressure and normal velocity are depicted in Figures 3.6 and 3.7.

It can be seen that the real and imaginary parts of pressures $\psi_j(0, y)$, $j = 1, 2, 3$ in their respective region match exactly to the pressure $\psi_4(0, y)$, $-b < y < b$.

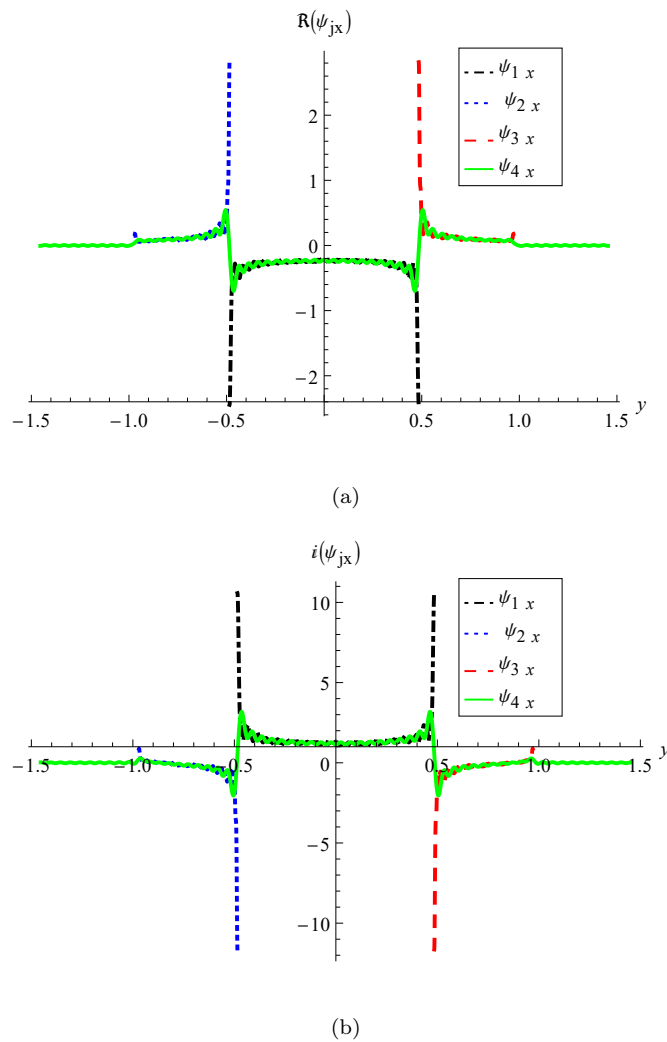


FIGURE 3.7: The real (a) and imaginary (b) parts of normal velocities against duct heights, at interface, with step-discontinuities and rigid-rigid boundaries, where, $\bar{a} = 0.05m$, $\bar{b} = 0.1m$, $\bar{h} = 0.15m$ and $N = 80$.

Likewise, the real and imaginary parts of normal velocities $\psi_{jx}(0, y)$, $j = 1, 2, 3$ in their respective regions match exactly to the normal velocity $\psi_{4x}(0, y)$, $-b < y < b$.

However, the real and imaginary parts of $\psi_{4x}(0, y)$ approach to zero in the regime $-h < y < -b$ and $b < y < h$, which is exactly the condition considered in (3.13).

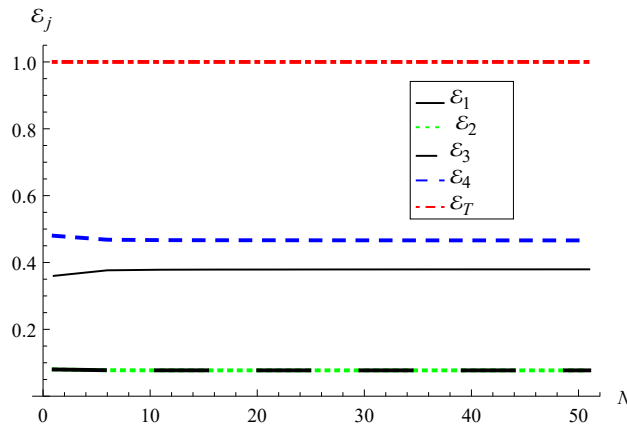


FIGURE 3.8: The scattering energies plotted against number of terms N for discontinuous structure where $\bar{a} = 0.05m$, $\bar{b} = 0.1m$, $\bar{h} = 0.15m$ and $f = 530Hz$.

The point-wise variation of energies versus number of terms N are shown in Figure 3.8, which obviously fulfill the conserve energy identity.

In this way, the truncated solution reconstruct successfully the matching conditions of pressures and velocities at interface i.e, (3.11)-(3.13). However, there appear some oscillations in normal velocity curves which lessen on increasing the number of modes.

One more physical check on accuracy of the truncated solution is the validation of conserved power identity $\mathcal{E}_T = 1$ while the inside of the waveguide contains compressible fluid. It holds even a few number of duct modes are allowed to propagate in their respective regions (see dotted line in Figures 3.2, 3.3, 3.4 and 3.5).

Chapter 4

Study of Generalized Planar Trifurcated Lined Duct Involving Structural Discontinuities

The underlying chapter investigates the scattering characteristics of a trifurcated lined duct involving structural discontinuities. A semi-infinite duct is located symmetrically within an infinite acoustic lined duct with step-discontinuities and generalised mixed boundaries. The scattered field potentials in each region are computed using mode-matching approach. Whereas the obtained energy functions of scattered fields are plotted with and without structural discontinuities and by varying the size of duct against different physical parameters. The existing results of trifurcated waveguide theory are recovered as a special case presenting thereby few additional results.

4.1 Mathematical Formulation

The physical problem under discussion is the diffraction of a fundamental incident mode propagating in the positive x -direction out of the end of a semi-infinite rigid duct. The dimensional scalar potential $\bar{\Phi}(\bar{x}, \bar{y}, \bar{t})$, which relates the acoustic

pressure and normal velocity inside the waveguide as:

$$\bar{p} = -\rho \frac{\partial \bar{\Phi}}{\partial \bar{t}} \quad \text{and} \quad \bar{v} = \overline{\nabla \Phi},$$

respectively, is introduced to define the boundary value problem. The quantity ρ here denotes the density of undisturbed compressible fluid. The time-harmonic dependence of $e^{-i\omega\bar{t}}$, where $\omega = ck$ is the angular frequency with wave number k and speed of sound c , is suppressed throughout. Thus, the time independent, dimensional fluid velocity potential $\bar{\psi}(\bar{x}, \bar{y})$ fulfils the Helmholtz equation as well as the general boundary conditions

$$\alpha \bar{\mathbf{n}} \cdot \overline{\nabla v} \pm \beta \bar{v} = 0. \quad (4.1)$$

Here α, β are some arbitrary constants chosen to assume the soft, rigid, or mixed type boundary conditions. The quantity $\bar{\mathbf{n}}$ represents the normal vector directed into the acoustic impedance of the lining represented by $\bar{Z} = \bar{p}/(\bar{v} \cdot \bar{\mathbf{n}})$. It should be noted that the quantities in the overbars represent the dimensional setting of coordinates.

As shown in Figure 4.1, an incident wave with time-harmonic dependency is considered travelling in the direction of \mathcal{R}_1 from negative x -direction to $\bar{x} = 0$. It will scatter into an infinite number of reflected and transmitted modes if $\bar{x} = 0$ is chosen.

Under the transformations $x = k\bar{x}$, $y = k\bar{y}$ and $t = \omega\bar{t}$, the governing boundary value problem can be dimensionless in relation to length scale k^{-1} and time scale ω^{-1} . The non-dimensional boundary value problem contains Helmholtz's equation and boundary conditions is modelled below:

$$(\nabla^2 + 1) \psi_j(x, y) = 0; \quad j = 1, 2, 3, 4, \quad -\infty < x < \infty, \quad (4.2)$$

$$\frac{\partial \psi_j}{\partial y} = 0, \quad y = \pm a, \quad -\infty < x < 0, \quad j = 1, 2, 3, \quad (4.3)$$

$$p\psi_2 - q \frac{\partial \psi_2}{\partial y} = 0, \quad y = -b, \quad -\infty < x < 0, \quad (4.4)$$

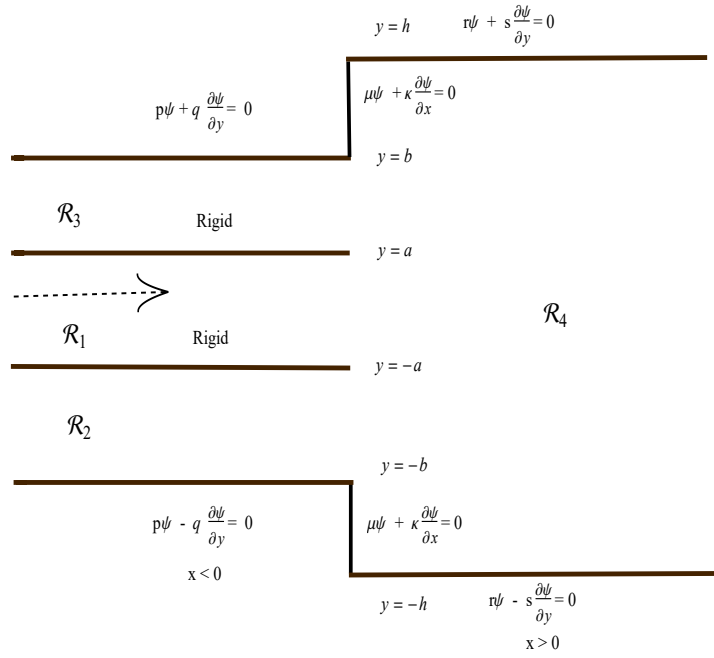


FIGURE 4.1: The geometry of the problem

$$p\psi_3 + q \frac{\partial \psi_3}{\partial y} = 0, \quad y = b, \quad -\infty < x < 0, \quad (4.5)$$

$$r\psi_4 \pm s \frac{\partial \psi_4}{\partial y} = 0, \quad y = \pm h, \quad 0 < x < \infty, \quad (4.6)$$

and

$$\mu\psi_4 + \kappa \frac{\partial \psi_4}{\partial x} = 0, \quad x = 0, \quad \text{for } -h \leq y \leq -b \text{ and } b \leq y \leq h, \quad (4.7)$$

where $\psi_j, j = 1 - 4$ denote the dimensionless field potential in $\mathcal{R}_j; j = 1 - 4$.

4.2 Mode-matching Solution

In this section, the underlined boundary value problem is solved using an MM approach. The MM procedure is based on matching pressure and normal velocity modes across interface regions. Thus, we first determine the propagating and scattering modes in various duct sections. That is

- Region $\mathcal{R}_1 := \{x < 0, \quad -a \leq y \leq a\}$

The eigen expansion form of field potential is given by equations (4.2) and (4.3)

in this region as:

$$\psi_1(x, y) = e^{ix} + \sum_{n=0}^{\infty} A_n \cos[\tau_n(y + a)]e^{-i\vartheta_n x}. \quad (4.8)$$

The reflected mode wave number is $\vartheta_n = \sqrt{1 - \tau_n^2}$, where τ_n are the eigenvalues satisfying the following dispersion relation

$$\sin [2\tau_n a] = 0, \text{ for } n = 0, 1, 2 \dots \quad (4.9)$$

The incident wave is represented by the first term in equation (4.8), while the reflected field is represented by the second term, in which A_n , are the amplitudes of unknown reflected mode. When matching conditions are applied, these unknowns will be determined. Further, the corresponding eigenfunctions $\cos[\tau_n(y + a)]$, fulfil the following OR

$$\int_{-a}^a \cos[\tau_m(y + a)] \cos[\tau_n(y + a)] dy = \epsilon_m a \delta_{mn}, \quad (4.10)$$

where $\epsilon_m = 2$ for $m = 0$ and 1 otherwise, and δ_{mn} is Kronecker delta.

- Regions $\mathcal{R}_2 := \{x < 0, \quad -b \leq y \leq -a\}$ and $\mathcal{R}_3 := \{x < 0, \quad a \leq y \leq b\}$

From equations (4.2)-(4.5), the eigen expansions of field potential in regions \mathcal{R}_2 and \mathcal{R}_3 are:

$$\psi_2(x, y) = \sum_{n=0}^{\infty} B_n \cos[\lambda_n(y + a)]e^{-i\kappa_n x}, \quad (4.11)$$

and

$$\psi_3(x, y) = \sum_{n=0}^{\infty} C_n \cos[\lambda_n(y - a)]e^{-i\kappa_n x}, \quad (4.12)$$

respectively. Here, $\kappa_n = \sqrt{1 - \lambda_n^2}$ be the wave number of n^{th} reflected mode and λ_n ; are the eigenvalues.

For Robin type (mixed) boundary conditions at $y = \pm b$, these eigenvalues address the required dispersion relation

$$p \cos[\lambda_n(b - a)] - q \lambda_n \sin[\lambda_n(b - a)] = 0. \quad (4.13)$$

The respective eigenfunctions $\cos[\lambda_n(y+a)]$ and $\cos[\lambda_n(y-a)]$ are orthogonal and fulfil the following OR's:

$$\int_{-b}^{-a} \cos[\lambda_m(y+a)] \cos[\lambda_n(y+a)] dy = \int_a^b \cos[\lambda_m(y-a)] \cos[\lambda_n(y-a)] dy = F_n \delta_{mn}, \quad (4.14)$$

where

$$F_n = \frac{2(b-a)\lambda_n + \sin[2(b-a)\lambda_n]}{4\lambda_n}. \quad (4.15)$$

- Region $\mathcal{R}_4 := \{x > 0, \quad -h \leq y \leq h\}$

From equations (4.2) and (4.6), the eigen expansion form of transmitted field is revealed as

$$\psi_4(x, y) = \sum_{n=0}^{\infty} D_n Y_n e^{i\varsigma_n x}, \quad (4.16)$$

where $\varsigma_n = \sqrt{1 - \gamma_n^2}$ is the n^{th} wave number of transmitted mode and γ_n are the eigen values, which satisfies the dispersion relation as follows:

$$(r^2 - s^2\gamma_n^2) \sin(2\gamma_n h) + 2rs\gamma_n \cos(2\gamma_n h) = 0, \quad \text{for } n = 0, 1, 2, \dots \quad (4.17)$$

Whereas, the respective eigenfunction Y_n ; satisfy the following OR's

$$\int_{-h}^h Y_m Y_n dy = G_n \delta_{mn}, \quad (4.18)$$

where

$$Y_n = r \sin[\gamma_n(y+h)] + s\gamma_n \cos[\gamma_n(y+h)], \quad (4.19)$$

and

$$G_n = \frac{1}{4\gamma_n} \{2\gamma_n(rs + 2h(r^2 + s^2\gamma_n^2)) - rs \cos(4h\gamma_n) + (-r^2 + s^2\gamma_n^2) \sin(4h\gamma_n)\}. \quad (4.20)$$

The unknown coefficients $\{A_n, B_n, C_n, D_n; n = 0, 1, 2, \dots\}$ are determined by using the matching conditions.

Thus, the continuity condition of the fluid pressure at matching interface is

$$\psi_1(0, y) = \psi_4(0, y), \quad -a \leq y \leq a. \quad (4.21)$$

On using equations (4.8) and (4.16) into (4.21), we get

$$1 + \sum_{n=0}^{\infty} A_n \cos[\tau_n(y + a)] = \sum_{n=0}^{\infty} D_n Y_n. \quad (4.22)$$

Multiplying equation (4.22) with $\cos[\tau_m(y + a)]$, integrating the result from $-a$ to a and then applying the OR (4.10), we have

$$A_m = \frac{-2\delta_{m0}}{\varepsilon_m} + \frac{1}{a\varepsilon_m} \sum_{n=0}^{\infty} D_n R_{mn}, \quad (4.23)$$

where

$$R_{mn} = \frac{\gamma_n}{\tau_m^2 - \gamma_n^2} \{(-1)^m H_n^+ - H_n^-\}, \quad (4.24)$$

and

$$H_n^{\pm} = r \cos[\gamma_n(h \pm a)] - s\gamma_n \sin[\gamma_n(h \pm a)]. \quad (4.25)$$

The continuity condition of the fluid pressure at matching interface is

$$\psi_2(0, y) = \psi_4(0, y), \quad -b \leq y \leq -a. \quad (4.26)$$

On using equations (4.11) and (4.16) into (4.26), we get

$$\sum_{n=0}^{\infty} B_n \cos[\lambda_n(y + a)] = \sum_{n=0}^{\infty} D_n Y_n. \quad (4.27)$$

By multiplying equation (4.27) with $\cos[\lambda_m(y + a)]$, integration the result from $-b$ to $-a$ and applying the OR (4.14), it is found that

$$B_m = \frac{1}{F_m} \sum_{n=0}^{\infty} D_n P_{mn}, \quad (4.28)$$

where

$$P_{mn} = \frac{1}{\gamma_n^2 - \lambda_m^2} \{ \gamma_n J_n + \gamma_n \cos[\lambda_m(b - a)] K_n - \lambda_m \sin[\lambda_m(b - a)] L_n \}, \quad (4.29)$$

and

$$J_n = -r \cos[\gamma_n(h - a)] + s\gamma_n \sin[\gamma_n(h - a)], \quad (4.30)$$

$$K_n = r \cos[\gamma_n(h - b)] - s\gamma_n \sin[\gamma_n(h - b)], \quad (4.31)$$

$$L_n = r \sin[\gamma_n(h - b)] + s\gamma_n \cos[\gamma_n(h - b)]. \quad (4.32)$$

The continuity condition of the fluid pressure at matching interface is

$$\psi_3(0, y) = \psi_4(0, y), \quad a \leq y \leq b. \quad (4.33)$$

On using equations (4.12) and (4.16) into (4.33), we get

$$\sum_{n=0}^{\infty} C_n \cos[\lambda_n(y - a)] = \sum_{n=0}^{\infty} D_n Y_n. \quad (4.34)$$

On multiplying equation (4.34) with $\cos[\lambda_m(y - a)]$, integrating the result from a to b and employing the orthogonality relation (4.14), we get

$$C_m = \frac{1}{F_m} \sum_{n=0}^{\infty} D_n Q_{mn}, \quad (4.35)$$

where

$$Q_{mn} = \frac{1}{\gamma_n^2 - \lambda_m^2} \{ \gamma_n M_n + \gamma_n \cos[\lambda_m(b - a)] N_n - \lambda_m \sin[\lambda_m(b - a)] T_n \}, \quad (4.36)$$

and

$$M_n = r \cos[\gamma_n(h + a)] - s\gamma_n \sin[\gamma_n(h + a)], \quad (4.37)$$

$$N_n = -r \cos[\gamma_n(h + b)] + s\gamma_n \sin[\gamma_n(h + b)], \quad (4.38)$$

$$T_n = r \sin[\gamma_n(h + b)] + s\gamma_n \cos[\gamma_n(h + b)]. \quad (4.39)$$

We now use the matching condition for normal velocities at the interface to get the unknown coefficient for region \mathcal{R}_4

$$\psi_{4x}(0, y) = \begin{cases} \frac{-\mu}{\kappa} \psi_4(0, y), & -h \leq y \leq -b, \\ \psi_{2x}(0, y), & -b \leq y \leq -a, \\ \psi_{1x}(0, y), & -a \leq y \leq a, \\ \psi_{3x}(0, y), & a \leq y \leq b, \\ \frac{-\mu}{\kappa} \psi_4(0, y), & b \leq y \leq h. \end{cases} \quad (4.40)$$

Therefore, using equations (4.8), (4.11), (4.12) and (4.16) into (4.40) we obtain

$$\sum_{n=0}^{\infty} D_n \varsigma_n Y_n = \begin{cases} \frac{-i\mu}{\kappa} \sum_{n=0}^{\infty} D_n Y_n, & -h \leq y \leq -b, \\ -\sum_{n=0}^{\infty} B_n \varkappa_n \cos[\lambda_n(y+a)], & -b \leq y < -a, \\ 1 - \sum_{n=0}^{\infty} A_n \vartheta_n \cos[\tau_n(y+a)], & -a \leq y < a, \\ -\sum_{n=0}^{\infty} C_n \varkappa_n \cos[\lambda_n(y-a)], & a \leq y < b, \\ \frac{-i\mu}{\kappa} \sum_{n=0}^{\infty} D_n Y_n, & b \leq y \leq h, \end{cases} \quad (4.41)$$

which on multiplying with Y_m integrating from $-h$ to h and applying the OR (4.18) yields

$$\begin{aligned} D_m = & \frac{R_{0m}}{\varsigma_m G_m} - \frac{1}{\varsigma_m G_m} \sum_{n=0}^{\infty} A_n \vartheta_n R_{nm} - \frac{1}{\varsigma_m G_m} \sum_{n=0}^{\infty} B_n \varkappa_n P_{nm} \\ & - \frac{1}{\varsigma_m G_m} \sum_{n=0}^{\infty} C_n \varkappa_n Q_{nm} + \frac{i\mu}{\kappa \varsigma_m G_m} \sum_{n=0}^{\infty} D_n (S_{mn} + H_{mn}), \end{aligned} \quad (4.42)$$

where

$$S_{mn} = \int_b^h Y_m Y_n dy \quad \text{and} \quad H_{mn} = \int_{-h}^{-b} Y_m Y_n dy.$$

Equation (4.42) initiate an infinite system of equations with unknowns

$D_m; m = 0, 1, 2, \dots$

These are inverted and reduced to find the unknown model coefficients. The quantities $\{A_n, B_n, C_n\}; n = 0, 1, 2, \dots$ may be simply calculated after getting the values of D_m using equations (4.23), (4.28) and (4.35). It is important to note that by changing $\mu = 0$ in equation (4.42), the vertical discontinuities became rigid.

4.3 Energy Balance

This section provides a graphical behavior of radiated energy in different duct regions along with reconstruction of matching conditions at interface. In prior to this, the system of equations given by equation (4.42) is truncated and solved numerically. In terms of dimensionless time-harmonic velocity potential of fluid,

the energy flux/power inside the duct regions is defined by

$$\frac{\partial \mathcal{E}}{\partial t} = \frac{1}{2} Re \left\{ i \int_{\Omega} \psi \left(\frac{\partial \psi}{\partial x} \right)^* dy \right\}, \quad (4.43)$$

where superscript asterisk (*) denotes the complex conjugate. From the definition of energy flux/power, the incident power is found to be $\mathcal{P}_{inc} = a$. Likewise, the energy flux/power components in all four duct regions are:

$$\mathcal{P}_1 = \frac{1}{2} Re \left\{ \sum_{n=0}^{\infty} |A_n|^2 \vartheta_n \varepsilon_n \right\}, \quad (4.44)$$

$$\mathcal{P}_2 = \frac{1}{2a} Re \left\{ \sum_{n=0}^{\infty} |B_n|^2 \varkappa_n F_n \right\}, \quad (4.45)$$

$$\mathcal{P}_3 = \frac{1}{2a} Re \left\{ \sum_{n=0}^{\infty} |C_n|^2 \varkappa_n F_n \right\}, \quad (4.46)$$

and

$$\mathcal{P}_4 = \frac{1}{2a} Re \left\{ \sum_{n=0}^{\infty} |D_n|^2 \zeta_n G_n \right\}. \quad (4.47)$$

It is important to note that the power fed into the system equals the sum of scattering powers in different duct regions, that is:

$$\mathcal{P}_{inc} = \mathcal{P}_1 + \mathcal{P}_2 + \mathcal{P}_3 + \mathcal{P}_4, \quad (4.48)$$

which is known as conserved power identity. For analysis purpose, we may scale the incident power at unity, which is obtained by dividing equation (4.48) by a that is

$$1 = \mathcal{E}_1 + \mathcal{E}_2 + \mathcal{E}_3 + \mathcal{E}_4, \quad (4.49)$$

where

$$\mathcal{E}_T = \sum_{j=1}^4 \mathcal{E}_j,$$

and

$$\mathcal{E}_j = \mathcal{P}_j/a, \quad j = 1, 2, 3, 4.$$

Note that \mathcal{E}_j , $j = 1, 2, 3, 4$ denote the power/energy flux components in duct sections \mathcal{R}_j ; $j = 1, 2, 3, 4$ for which the power incident is scaled to be one.

4.4 Numerical Results and Discussions

The underlying discussion is mainly focused in three ways while considering the waveguide structure with and without step-discontinuities.

In first part, the reflected energy is visualized for different material properties of outer bounding ducts.

In second part, the reflected energy is plotted by considering specific impedance for a fibrous sheet.

The results obtained in this part are compared with existing results [9] as a special case.

Whereas, the energy distribution in all regions of trifurcated ducts is analyzed in the third part. It is worth mentioning that the energy distribution in all cases is plotted against frequency regime and height of the ducts.

Part-I:

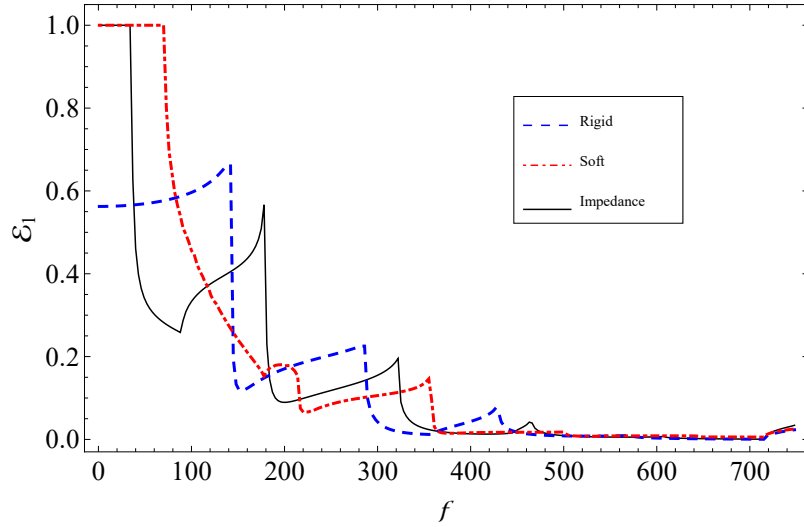
Figures 4.2 and 4.3 are plotted to see the reflected power behavior against frequency regime ($1Hz - 750Hz$) with and without step-discontinuities.

In Figure 4.2, the duct regions ($\mathcal{R}_2 - \mathcal{R}_4$) are considered to be more wider than in case of Figure 4.3.

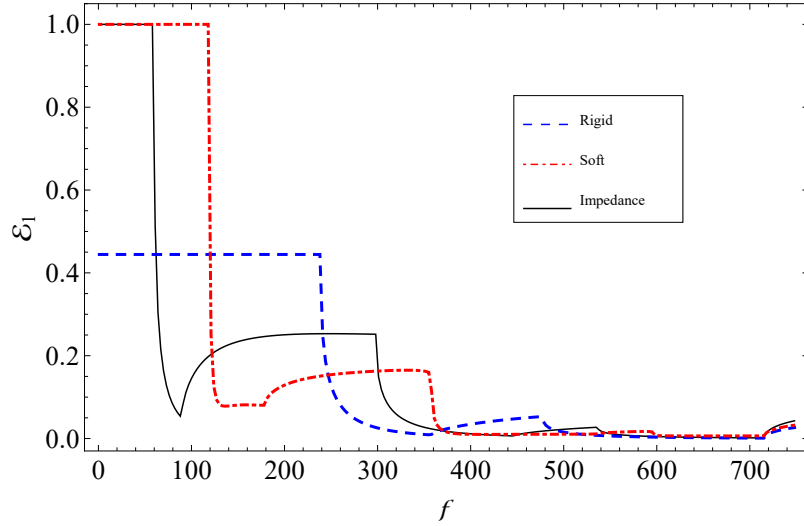
It is noted that in Figure 4.2(a), six duct modes are cut-on at frequencies $(88, 178, 322, 463, 607, 715)Hz$ while in Figure 4.2(b), four duct modes are cut-on at frequencies $(88, 298, 535, 715)Hz$ and in Figure 4.3(a), two duct modes are cut-on at frequencies $(358, 715)Hz$ while in Figure 4.3(b), three duct modes are cut-on at frequencies $(355, 595, 715)Hz$.

In Figures 4.2 and 4.3 for soft and impedance boundary conditions, it is noted that all the energy seems to be reflected.

This indicates that no energy is transferred into the region \mathcal{R}_4 at lower frequencies but for higher frequencies the real values of wave numbers are increased which indicates that sound is attenuated. More reflection predicts less transmission.



(a)

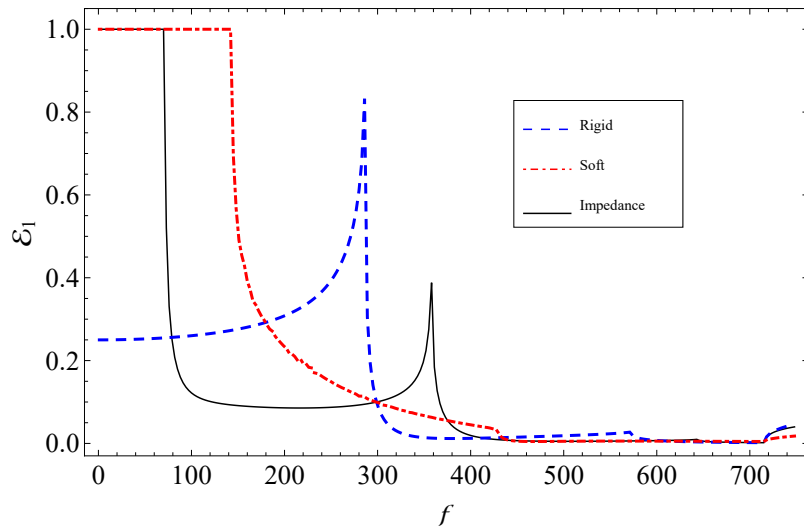


(b)

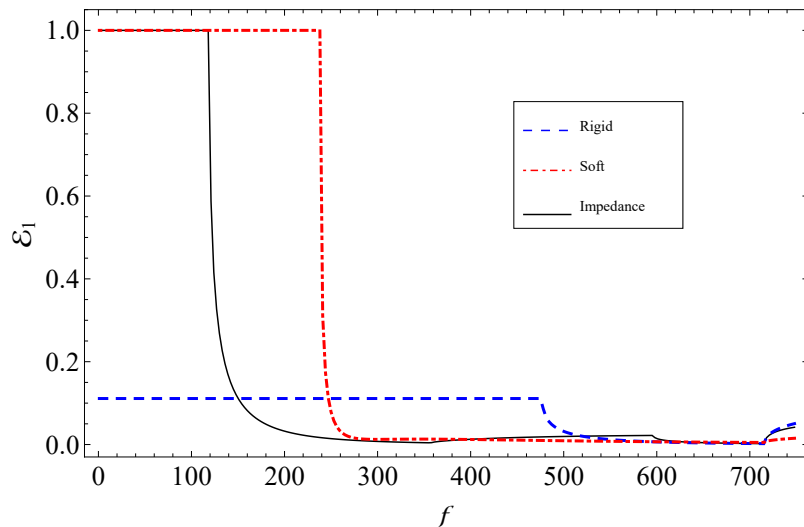
FIGURE 4.2: Reflected energy in region $\mathcal{R}_1(\mathcal{E}_1)$ versus frequency (f) for Hard, Soft and Impedance outer bounding walls (a) with step-discontinuous ($b \neq h$) (b) without step-discontinuous ($b = h$) where $\bar{a} = 0.24m$, $\bar{b} = 3\bar{a}$ and $N = 10$.

These cut-on modes are obtained for impedance outer bounding walls (for brevity). It is observed that more number of cut-on modes appeared in case of impedance walls with step-discontinuities.

However, the cut-on modes are reduced considerably when step-discontinuities are removed. The occurrence of these cut-on modes is responsible to attenuate the sound propagating through transmitted region.



(a)

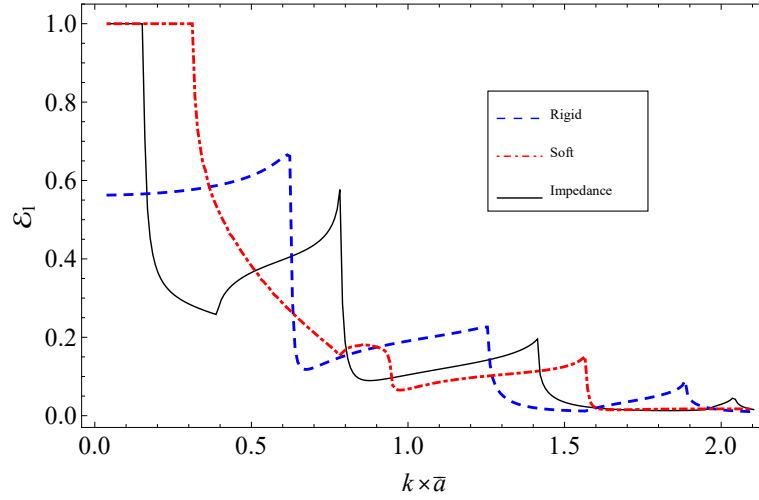


(b)

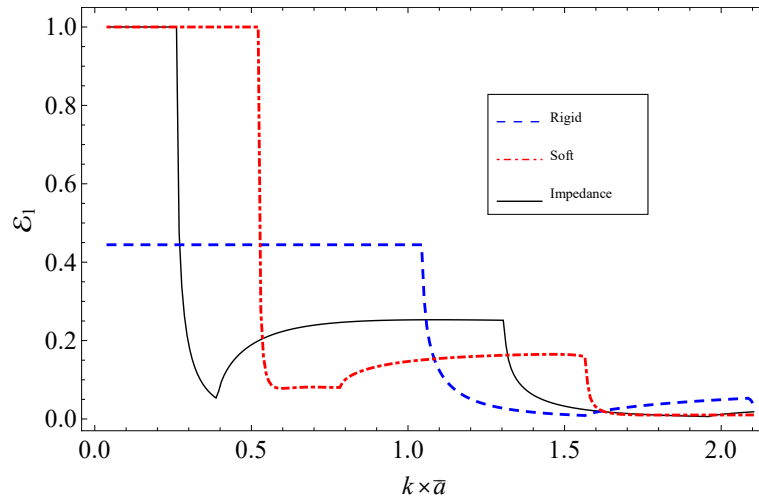
FIGURE 4.3: Reflected energy in region $\mathcal{R}_1(\mathcal{E}_1)$ versus frequency (f) for Hard, Soft and Impedance outer bounding walls (a) with step-discontinuous ($b \neq h$) (b) without step-discontinuous ($b = h$) where $\bar{a} = 0.24m$, $\bar{b} = \frac{3\bar{a}}{2}$ and $N = 10$.

Albeit, the consideration of lined duct provided more attenuation in the transmitted region when it is compared with hard or soft ducts. Figure 4.3 depicts that number of cut-on modes becomes lesser when the duct regions ($\mathcal{R}_2 - \mathcal{R}_4$) are reduced considerably which ultimately resulted a lesser attenuation. Figures 4.4 and 4.5 are plotted to observe the behavior of the reflected energy by varying the height of the inner duct by letting $\bar{b} = 3\bar{a}$ and $\bar{b} = \frac{3\bar{a}}{2}$, respectively. Two situations

are considered that, is; measure of reflected energy due to **a)** step-discontinuities and **b)** without step-discontinuities. Again, a similar behavior in the reflected energy is observed.



(a)

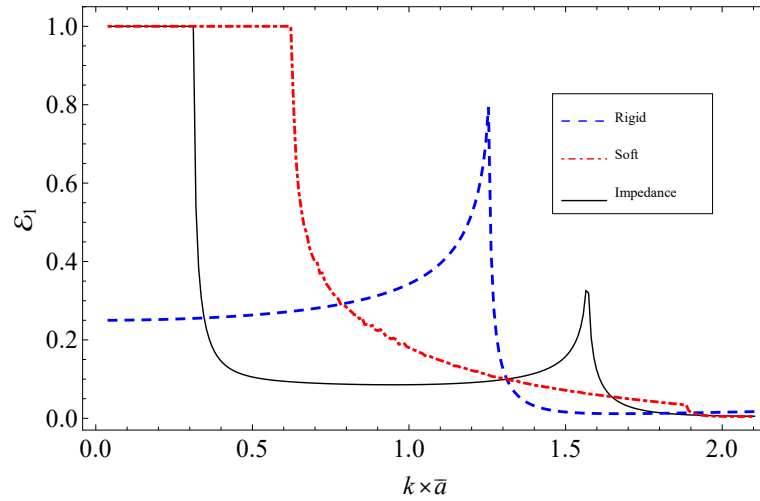


(b)

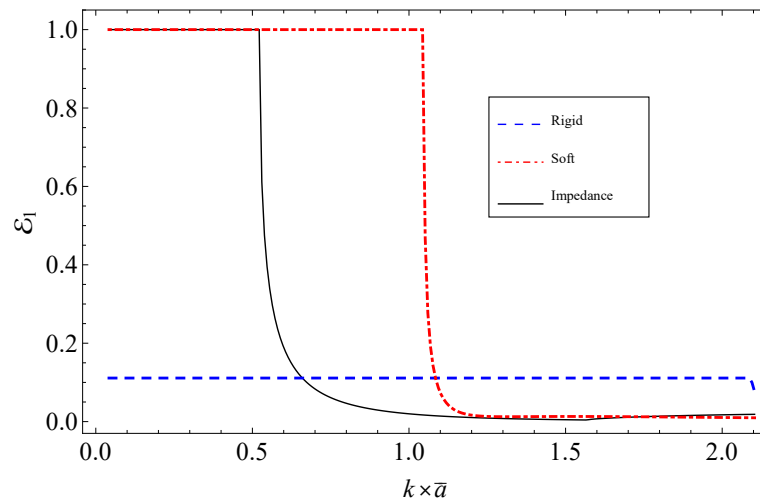
FIGURE 4.4: Reflected energy in region $\mathcal{R}_1(\mathcal{E}_1)$ versus $k \times \bar{a}$ for Hard, Soft and Impedance outer bounding walls (a) with step-discontinuous ($b \neq h$) (b) without step-discontinuous ($b = h$) where, $f = 230Hz$, $\bar{b} = 3\bar{a}$ and $N = 10$.

It is noted that in Figure 4.4(a), six duct modes are cut-on at $k \times \bar{a} \approx 0.387052m$, $0.782517m$, $0.875073m$, $1.41358m$, $1.91002m$, $2.03623m$ while in Figure 4.4(b), three duct modes are cut-on at $k \times \bar{a} \approx 0.387052m$, $1.3042m$, $1.9605m$ and the first cut-on duct mode occurs at $k \times \bar{a} \approx 1.57345m$ and $k \times \bar{a} \approx 1.56503m$ for Figures 4.5(a)

and 4.5(b) respectively, while the other cut-on modes are beyond the chosen domain. These cut-on modes are obtained for impedance outer bounding walls (for brevity).



(a)

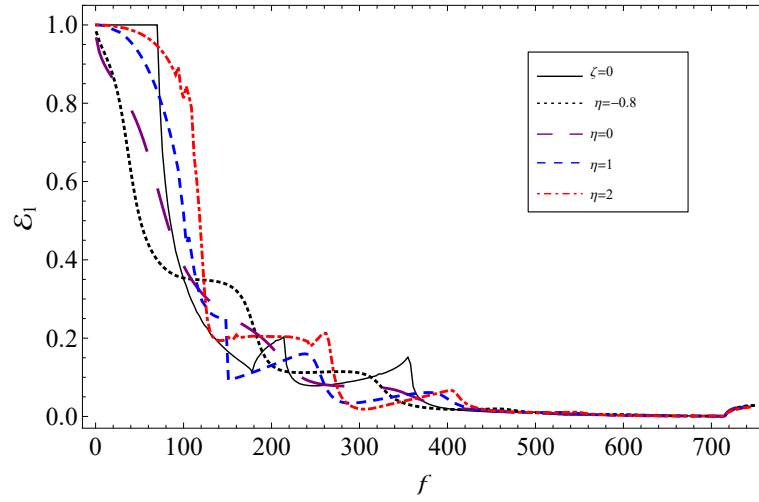


(b)

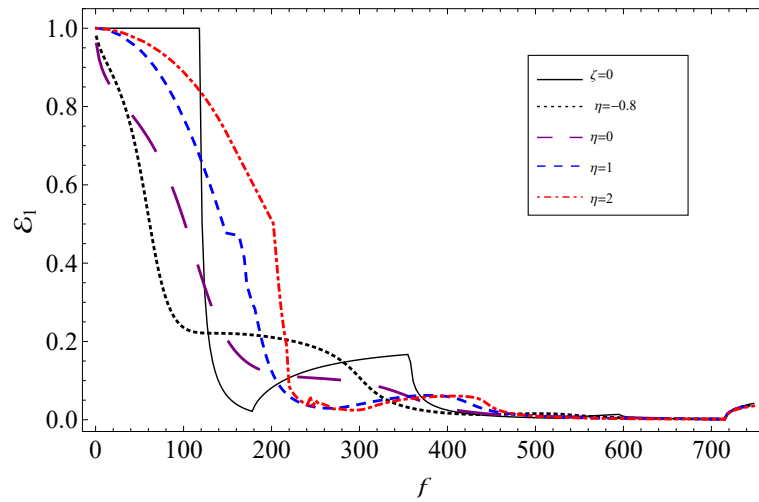
FIGURE 4.5: Reflected energy in region $\mathcal{R}_1(\mathcal{E}_1)$ versus $k \times \bar{a}$ for Hard, Soft and Impedance outer bounding walls (a) with step-discontinuous ($b \neq h$) (b) without step-discontinuous ($b = h$) where, $f = 230Hz$, $\bar{b} = \frac{3\bar{a}}{2}$ and $N = 10$.

As long as height of the inner duct becomes wider, the reflected energy reduces more rapidly. There is sharp variation in the graphs when $\bar{b} = 3\bar{a}$ as compared when $\bar{b} = \frac{3\bar{a}}{2}$ where a smooth and consistent behavior of reflected energy is observed (see Figure 4.5). We see that in Figures 4.2 – 4.5, the outer boundaries of

inlet and outlet regions are bounded by planar boundary conditions.



(a)



(b)

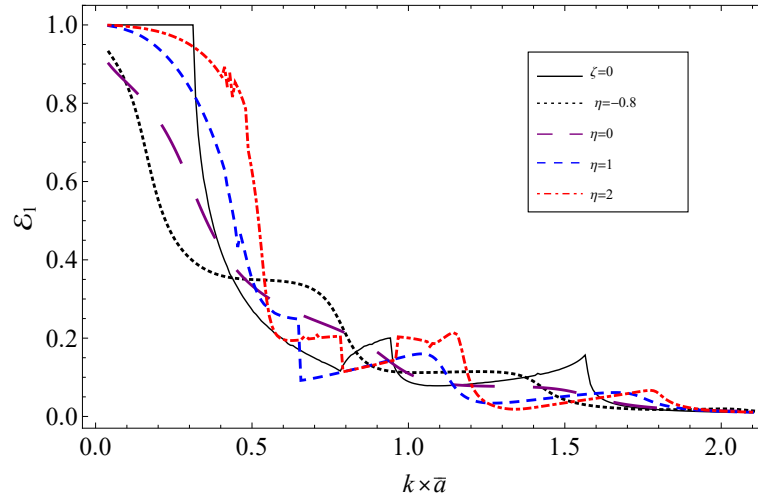
FIGURE 4.6: The reflected flux/power components against frequency containing compressible fluid in (a) discontinuous (b) continuous waveguides for $\bar{a} = 0.24m, \bar{b} = 3\bar{a}, \xi = 0.5, p = r = 1, q = s = i\xi$ and $N = 10$.

It is expected that due to soft and impedance boundaries conditions, the reflected power is almost maximum whereas transmitted power is minimum at lower frequencies and height of duct respectively.

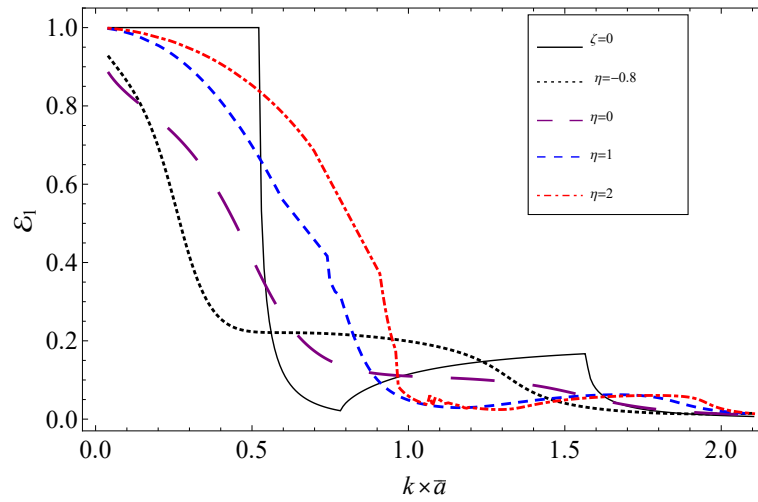
Part-II:

In this part, we are interested to observe the reflected energy by considering the

parametric setting as used by Rawlins [9].



(a)

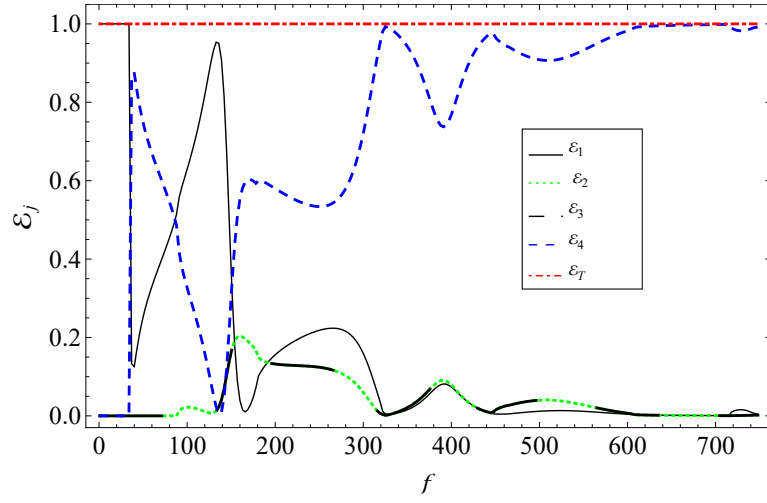


(b)

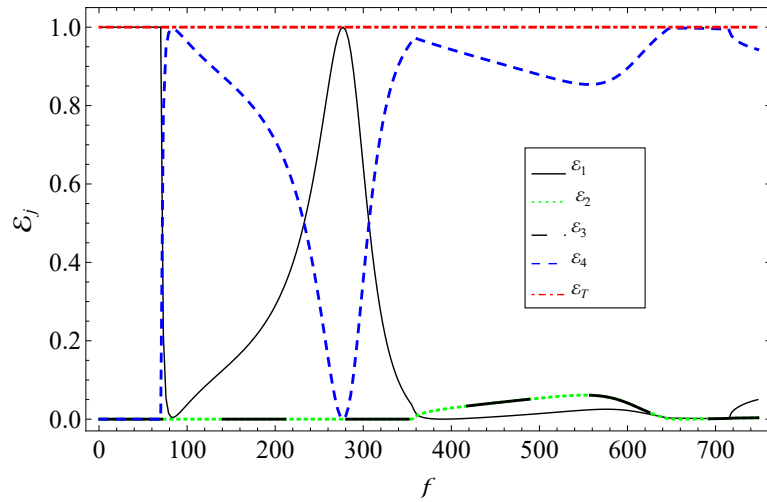
FIGURE 4.7: The reflected flux/power components against $k \times \bar{a}$ containing compressible fluid in (a) discontinuous (b) continuous waveguides for $f = 230Hz$, $\bar{b} = 3\bar{a}$, $\xi = 0.5$, $p = r = 1$, $q = s = i\zeta$ and $N = 10$.

The following values for the specific impedance ($\zeta = \xi + i\eta$) which is fibrous sheet, are used : $\xi = 0.5$, $-1.0 < \eta < 3.0$. Keeping in mind that impedance parameters used in this article are related with [9] as $p = 1$, $q = \frac{i\zeta}{k}$. Figures 4.6(a) and 4.7(a) are plotted in the presence of step-discontinuities ($b \neq h$) against frequency regime and height of the duct respectively. Whereas, Figures 4.6(b) and 4.7(b)

are plotted in the absence of step-discontinuities ($b = h$) which indeed resembled closely with the study of Rawlins [9].



(a)

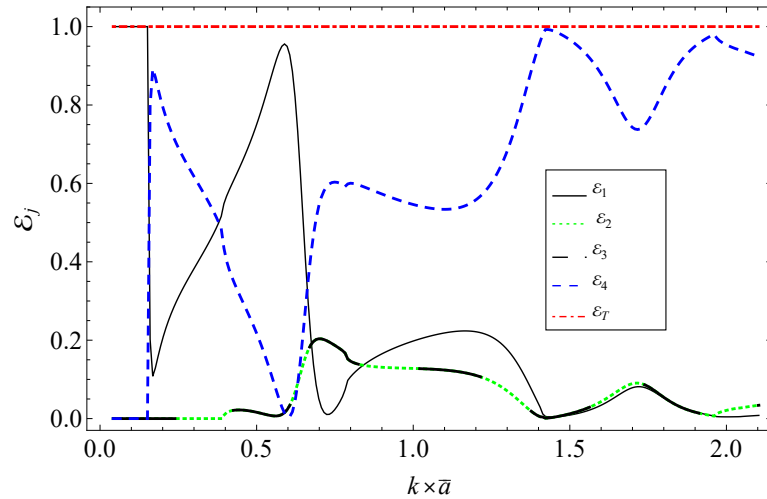


(b)

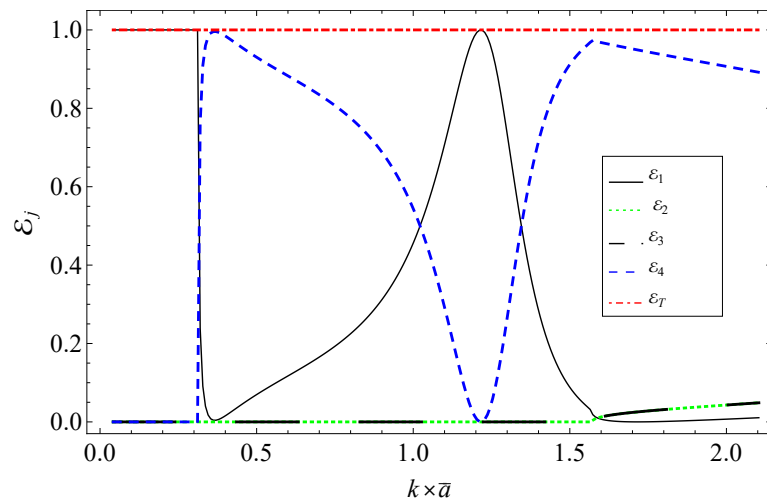
FIGURE 4.8: The radiated energy flux/power components against frequency containing compressible fluid in discontinuous waveguide for (a) $\bar{b} = 3\bar{a}$ (b) $\bar{b} = \frac{3\bar{a}}{2}$, $\bar{a} = 0.24m$, $p = q = r = s = 1$ and $N = 10$.

The cut-on modes occurred at $(178, 214, 355, 715)Hz$ and $(178, 355, 715)Hz$ for Figures 4.6(a) and 4.6(b) while, cut-on modes occurred at $k \times \bar{a} \approx 0.782517m$, $0.942386m$, $1.56503m$ and $k \times \bar{a} \approx 0.782517m$, $1.56503m$ for Figures 4.7(a) and 4.7(b) respectively. These cut-on modes are obtained for $\zeta = 0$ (for brevity).

From present analysis, it is seen that the results of Rawlins [9] are closely related to our study.



(a)

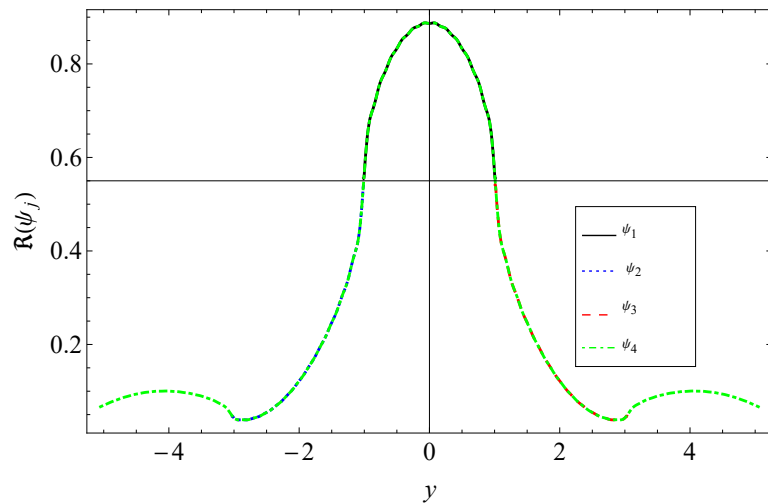


(b)

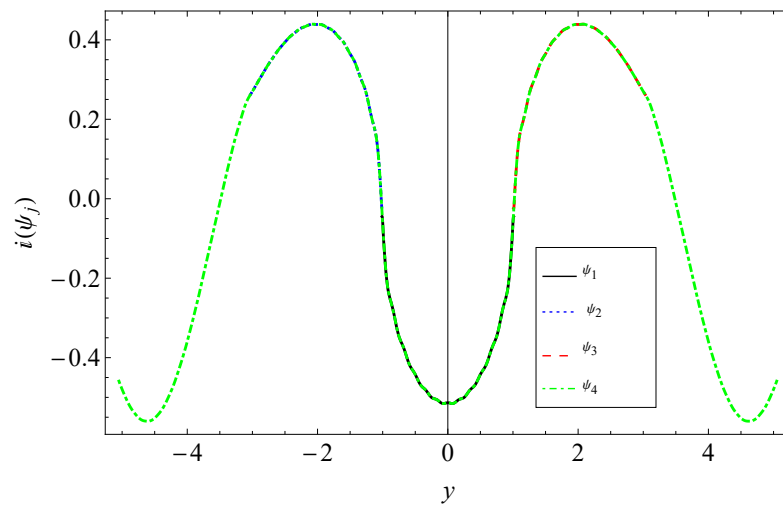
FIGURE 4.9: The radiated energy flux/power components against $k \times \bar{a}$ containing compressible fluid in discontinuous waveguide for (a) $\bar{b} = 3\bar{a}$ (b) $\bar{b} = \frac{3\bar{a}}{2}$, $\bar{a} = 0.24m$, $p = q = r = s = 1$ and $N = 10$.

We presented a qualitative comparison with Rawlins but with different values of parameters. We have used the MM technique for the same waveguide and Figure 4.7(b) is in close tie with the results obtained by Rawlins [9] using WH-Technique. It is clearly observed that more cut-on modes are propagating in the presence of step-discontinuities when compared results in the absence of step-discontinuities.

This altogether justifies the MM solution which is computed in the presence of step-discontinuities. Besides, the reflected energy reduces considerably by increasing the frequency regime and height of the duct. Further, in case of no fibrous sheet, the curve pattern is quite smooth and very few modes are cut-on. However, the increasing value of η , increases the number of cut-on modes.



(a)



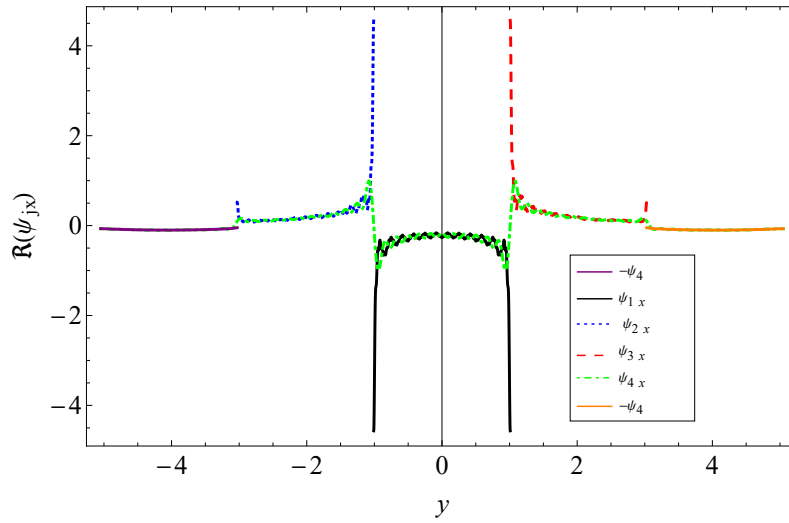
(b)

FIGURE 4.10: The real (a) and imaginary (b) parts of pressure at interface for $\bar{a} = 0.24m$, $\bar{b} = 3\bar{a}$, $\bar{h} = 5\bar{a}$, $\mu = \kappa = 1$ and $N = 120$.

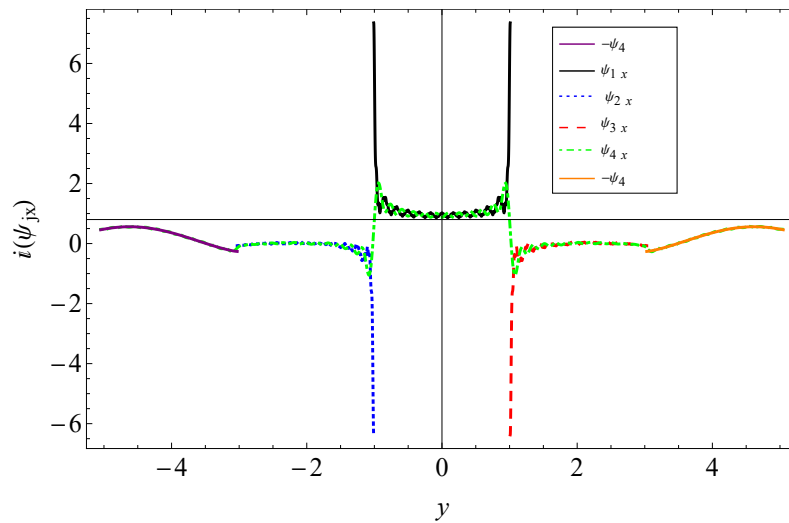
Part-III:

The energy distribution in different duct regions against frequency (f) and variation in symmetric height discontinuity $a = k \times \bar{a}$ is shown in Figures 4.8 and 4.9

respectively. Here, the distribution of energy is plotted only in the presence of step-discontinuities. Number of cut-on modes occur which show that more energy is absorbed.



(a)



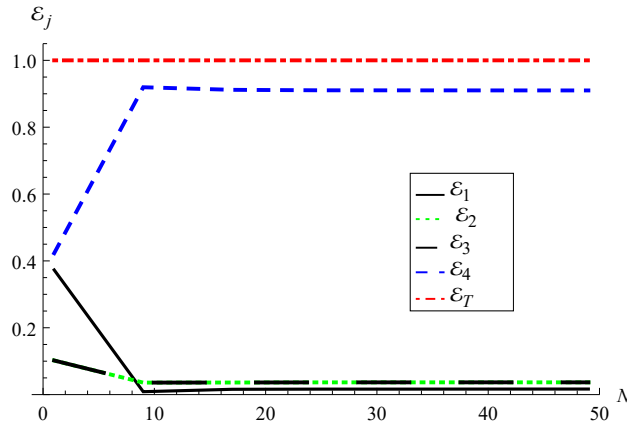
(b)

FIGURE 4.11: The real (a) and imaginary (b) parts of normal velocity at interface for $\bar{a} = 0.24m$, $\bar{b} = 3\bar{a}$, $\bar{h} = 5\bar{a}$, $\mu = \kappa = 1$ and $N = 120$.

In Figure 4.8(a), eight duct modes are cut-on at frequencies (40, 133, 166, 328, 391, 457, 523, 715)Hz while in Figure 4.8(b), four duct modes are cut-on at frequencies (82, 277, 391, 709)Hz when inner duct region \mathcal{R}_1 is condensed. Figures 4.9(a)

and 4.9(b) are sketched for energy distribution in different duct regions by varying the height of the duct. It is noted that seven cut-on modes occur at $k \times \bar{a}$ ($0.168283m, 0.588991m, 0.723618m, 1.16115m, 1.43882m, 1.71649m, 2.00257m$) and three cut-on modes occur at $k \times \bar{a}$ ($0.370223m, 1.22847m, 1.71649m$), respectively. It is observed that after certain level of frequency, most of the energy is transmitted through region \mathcal{R}_4 . In addition, the number of cut-on modes reduce to very few values when inner duct region is shortened ($\bar{b} = \frac{3\bar{a}}{2}$). Though, a sharp inversion in the energy distribution is observed yet, overall energy remains conserved.

To validate the truncated solution, the conditions of pressure and normal velocities are sketched at the interface. Figures 4.10 and 4.11 shows that the real and imaginary parts of pressures and normal velocities conditions exactly coincide in their respective regions. As a result, the normal velocities and pressure matching conditions are entirely satisfied. The point-wise variation of radiated energies verses N are shown Figure 4.12, which clearly satisfy the conserve energy identity (4.49).



(a)

FIGURE 4.12: The scattering energies plotted against number of terms N for discontinuous structure where $\bar{a} = 0.24m$, $\bar{b} = 3\bar{a}$, $\bar{h} = 5\bar{a}$ and $f = 530Hz$.

Chapter 5

Scattering Attributes of Planar Trifurcated Waveguide Structure with Finite Discontinuities

The scattering attributes of a planar trifurcated waveguide structure with numerous discontinuities are examined in this chapter. This physical problem is shaped to demonstrate the scattering behaviour of acoustic waves in a planar waveguide with structural discontinuities. After interacting with the discontinuities and edges of the underlying structure, the fluid-structure coupled waveforms scatter. The MM technique is used in accordance to calculate fluid velocity potentials. By varying the dimensions of the expansion chamber and the wave frequency, the guiding structure is then analysed and validated using scattering energy or power functional. The results are formulated and analysed using the matching conditions, expansion chamber dimension, and wave frequencies, validating the obtained solutions.

This chapter is structured as follows: The boundary value problem for the duct modes, as well as the appropriate orthogonality relations, are illustrated in Section. 5.1. These are used in Section. 5.2, where the MM technique is used to solve the boundary value problem. Energy balance is achieved in Section. 5.3. Numerical results and discussions are provided in Section. 5.4.

5.1 Mathematical Formulation

Consider a trifurcated waveguide which comprises an expansion chamber occupying the duct regions: \mathcal{R}_j ; $j = 1, 2, \dots, 7$. Inside the regions \mathcal{R}_j ; $j = 1, 2, \dots, 7$ is indeed a fluid with ρ as density and c as sound speed. The bounding wall conditions of the regions may vary:

- (a) Each of the regions \mathcal{R}_j ; $j = 1, 6$ are bounded by acoustically rigid boundaries.
- (b) The regions \mathcal{R}_j ; $j = 2, 3, 4, 5, 7$ comprise the rigid, soft as well as impedance boundaries.

The outside of the waveguide is set into *vacou*. At $\bar{x} = \pm L$, there lies two vertical step discontinuities aligned along with $-\bar{h} \leq \bar{y} \leq -\bar{b}$ and $\bar{b} \leq \bar{y} \leq \bar{h}$.

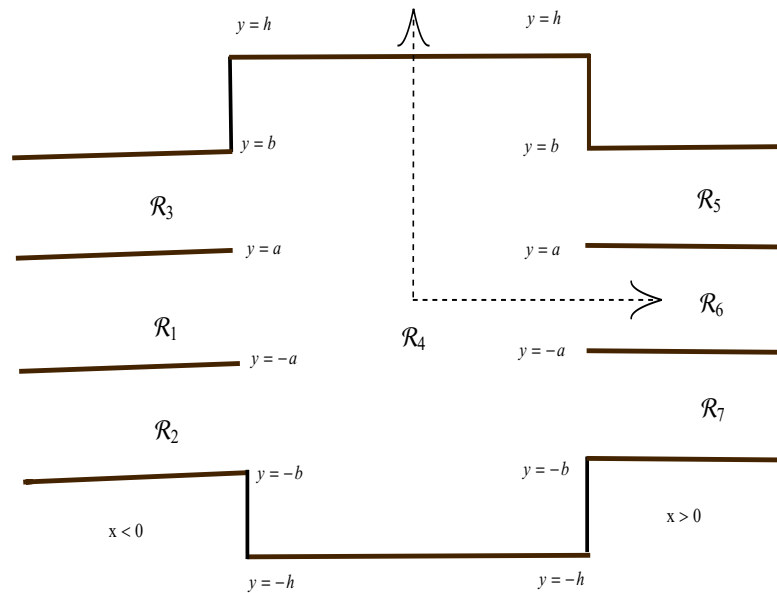


FIGURE 5.1: The geometry of the problem

An incident wave of time-harmonic dependence is propagating in \mathcal{R}_1 from negative x -direction towards $\bar{x} = 0$ as shown in Figure 5.1. At $\bar{x} = 0$, it will scatter into the infinite number of reflected and transmitted modes. For convenience, we non-dimensionalize the governing boundary value problem according to length scale

k^{-1} and time scale ω^{-1} with transformations

$$x = k\bar{x} \quad y = k\bar{y} \quad \text{and} \quad t = \omega\bar{t}.$$

The dimensionless boundary value problem contains Helmholtz's equation and boundary conditions is modeled below:

$$(\nabla^2 + 1) \psi_j(x, y) = 0; \quad j = 1, 2, \dots, 7, \quad -\infty < x < \infty, \quad (5.1)$$

$$\frac{\partial \psi_j}{\partial y} = 0, \quad y = \pm a, \quad -\infty < x < -L, \quad j = 1, 2, 3, \quad (5.2)$$

$$\frac{\partial \psi_j}{\partial y} = 0, \quad y = \pm a, \quad L < x < \infty, \quad j = 5, 6, 7, \quad (5.3)$$

$$p\psi_j \pm q \frac{\partial \psi_j}{\partial y} = 0, \quad y = \pm b, \quad -\infty < x < -L, \quad j = 3, 2, \quad (5.4)$$

$$p\psi_j \pm q \frac{\partial \psi_j}{\partial y} = 0, \quad y = \pm b, \quad L < x < \infty, \quad j = 5, 7, \quad (5.5)$$

$$r\psi_4 \pm s \frac{\partial \psi_4}{\partial y} = 0, \quad y = \pm h, \quad -L < x < L, \quad (5.6)$$

$$\mu\psi_4 \pm \kappa \frac{\partial \psi_4}{\partial x} = 0, \quad x = \mp L, \quad \text{for} \quad -h \leq y \leq -b \quad \text{and} \quad b \leq y \leq h, \quad (5.7)$$

where, ψ_j , $j = 1, 2, \dots, 7$, denote the non-dimensional field potentials in various regions $\mathcal{R}_j : j = 1, 2, \dots, 7$.

Here, p, q, r, s, μ and κ appearing in equations (5.4), (5.5), (5.6) and (5.7) are any arbitrary constants. We can change their values from 0 to 1 to acquire one of the rigid, soft, or impedance/mixed type boundary conditions.

5.2 Mode-matching Solution

This section includes a MM solution to the underlined boundary value problem. The mode-matching technique relies on the matching of normal velocity and pressure modes across the interface regions.

Thus, we first determine the propagating and scattering modes inside the regions $\mathcal{R}_j : j = 1, 2, \dots, 7$. That is:

- Region $\mathcal{R}_1 := \{x < -L, \quad -a \leq y \leq a\}$

In this region, equations (5.1) and (5.2) gives the eigen expansion form of field potential as:

$$\psi_1(x, y) = e^{i(x+L)} + \sum_{n=0}^{\infty} A_n \cos[\tau_n(y+a)]e^{-i\vartheta_n(x+L)}. \quad (5.8)$$

The quantity $\vartheta_n = \sqrt{1 - \tau_n^2}$, is the n^{th} reflected mode wave number, where τ_n , be the eigenvalues satisfying the following dispersion relation

$$\sin(2\tau_n a) = 0, \text{ for } n = 0, 1, 2, \dots \quad (5.9)$$

It is noted that the incident wave is given by the first term in equation (5.8), while the reflected field is represented by the second term, nevertheless A_n , are the reflected mode coefficients and are unknowns.

The unknowns will be determined later when matching conditions are applied. Further, the corresponding eigenfunctions $\cos[\tau_n(y+a)]$, $n = 0, 1, 2, \dots$ fulfil the concerning orthogonality relation

$$\int_{-a}^a \cos[\tau_m(y+a)] \cos[\tau_n(y+a)] dy = \epsilon_m a \delta_{mn}, \quad (5.10)$$

where $\epsilon_m = 2$ for $m = 0$ and 1 otherwise, and δ_{mn} is Kronecker delta.

- Region $\mathcal{R}_6 := \{x > L, \quad -a \leq y \leq a\}$

By using equations (5.1) and (5.3), the eigen expansions form of field potential in transmitted region \mathcal{R}_6 is:

$$\psi_6(x, y) = \sum_{n=0}^{\infty} T_n \cos[\tau_n(y+a)]e^{i\vartheta_n(x-L)}. \quad (5.11)$$

- Regions $\mathcal{R}_2 := \{x < -L, \quad -b \leq y \leq -a\}$ and $\mathcal{R}_3 := \{x < -L, \quad a \leq y \leq b\}$

From equations (5.1)-(5.5), the eigen expansions of field potential in regions \mathcal{R}_2 and \mathcal{R}_3 are;

$$\psi_2(x, y) = \sum_{n=0}^{\infty} B_n \cos[\lambda_n(y+a)]e^{-i\lambda_n(x+L)}, \quad (5.12)$$

and

$$\psi_3(x, y) = \sum_{n=0}^{\infty} C_n \cos[\lambda_n(y - a)]e^{-i\kappa_n(x+L)}, \quad (5.13)$$

respectively.

Here, $\kappa_n = \sqrt{1 - \lambda_n^2}$ be the wave number of n^{th} reflected mode and λ_n ; $n = 0, 1, 2, \dots$ are the eigenvalues.

- Regions $\mathcal{R}_5 := \{x > L, \quad a \leq y \leq b\}$ and $\mathcal{R}_7 := \{x > L, \quad -b \leq y \leq -a\}$

The eigen expansions form of field potential in transmitted regions \mathcal{R}_5 and \mathcal{R}_7 are

$$\psi_5(x, y) = \sum_{n=0}^{\infty} K_n \cos[\lambda_n(y - a)]e^{i\kappa_n(x-L)}, \quad (5.14)$$

and

$$\psi_7(x, y) = \sum_{n=0}^{\infty} M_n \cos[\lambda_n(y + a)]e^{i\kappa_n(x-L)}. \quad (5.15)$$

For Robin type (mixed) boundary conditions at $y = \pm b$, these eigenvalues fulfil the following dispersion relation

$$p \cos[\lambda_n(b - a)] - q\lambda_n \sin[\lambda_n(b - a)] = 0. \quad (5.16)$$

The corresponding eigenfunctions $\cos[\lambda_n(y + a)]$ and $\cos[\lambda_n(y - a)]$, are orthogonal and deals with the usual orthogonality relations as follows:

$$\int_{-b}^{-a} \cos[\lambda_m(y + a)] \cos[\lambda_n(y + a)] dy = \int_a^b \cos[\lambda_m(y - a)] \cos[\lambda_n(y - a)] dy = F_n \delta_{mn}, \quad (5.17)$$

where

$$F_n = \frac{2(b - a)\lambda_n + \sin[2(b - a)\lambda_n]}{4\lambda_n}. \quad (5.18)$$

- Region $\mathcal{R}_4 := \{-L < x < L, \quad -h \leq y \leq h\}$

From equations (5.1) and (5.6), $\psi_4(x, y)$ is revealed as

$$\psi_4(x, y) = \sum_{n=0}^{\infty} D_n^+ Y_n e^{-i\kappa_n x} + \sum_{n=0}^{\infty} D_n^- Y_n e^{i\kappa_n x}, \quad (5.19)$$

where, $\varsigma_n = \sqrt{1 - \gamma_n^2}$, is the wave number of n^{th} mode and γ_n are the eigenvalues and that satisfy the dispersion relation as

$$(r^2 - s^2\gamma_n^2) \sin[2\gamma_n h] + 2rs\gamma_n \cos[2\gamma_n h] = 0, \text{ for } n = 0, 1, 2, \dots \quad (5.20)$$

Whereas, the eigenfunction Y_n satisfy the following orthogonality relation

$$\int_{-h}^h Y_m Y_n dy = G_n \delta_{mn}, \quad (5.21)$$

where

$$Y_n = r \sin[\gamma_n(y + h)] + s\gamma_n \cos[\gamma_n(y + h)], \quad (5.22)$$

and

$$G_n = \frac{1}{4\gamma_n} \{ 2\gamma_n(rs + 2c(r^2 + s^2\gamma_n^2) - rs \cos[4c\gamma_n]) + (-r^2 + s^2\gamma_n^2) \sin[4c\gamma_n] \}. \quad (5.23)$$

The unknown coefficients $\{A_m, B_m, C_m, D_m^+, D_m^-, T_m, M_m, K_m; m = 0, 1, 2, \dots\}$ are found by using the matching conditions. Thus, the continuity condition of the fluid pressure at matching interface is

$$\psi_1(-L, y) = \psi_4(-L, y), \quad -a \leq y \leq a. \quad (5.24)$$

On using equations (5.8) and (5.19) in (5.24), we get

$$1 + \sum_{n=0}^{\infty} A_n \cos[\tau_n(y + a)] = \sum_{n=0}^{\infty} D_n^+ Y_n e^{i\varsigma_n L} + \sum_{n=0}^{\infty} D_n^- Y_n e^{-i\varsigma_n L}. \quad (5.25)$$

The multiplying of equation (5.25) with $\cos[\tau_m(y + a)]$ and integrating the result from $-a$ to a and after that employing the given orthogonality relation (5.10), we have

$$A_m = \frac{-2\delta_{m0}}{\varepsilon_m} + \frac{1}{a\varepsilon_m} \left(\sum_{n=0}^{\infty} D_n^+ R_{mn} e^{i\varsigma_n L} + \sum_{n=0}^{\infty} D_n^- R_{mn} e^{-i\varsigma_n L} \right), \quad (5.26)$$

where

$$R_{mn} = \frac{\gamma_n}{\tau_m^2 - \gamma_n^2} \{ (-1)^m H_n^+ - H_n^- \}, \quad (5.27)$$

and

$$H_n^\pm = r \cos[\gamma_n(h \pm a)] - s\gamma_n \sin[\gamma_n(h \pm a)]. \quad (5.28)$$

The continuity condition of the fluid pressure at matching interface is

$$\psi_2(-L, y) = \psi_4(-L, y), \quad -b \leq y \leq -a. \quad (5.29)$$

On using equations (5.12) and (5.19) in (5.29), we get

$$\sum_{n=0}^{\infty} B_n \cos[\lambda_n(y + a)] = \sum_{n=0}^{\infty} D_n^+ Y_n e^{i\kappa_n L} + \sum_{n=0}^{\infty} D_n^- Y_n e^{-i\kappa_n L}. \quad (5.30)$$

Again, multiplying equation (5.30) with $\cos[\lambda_m(y + a)]$, integration it from $-b$ to $-a$ and after that applying the orthogonality relation (5.17), it is observed that

$$B_m = \frac{1}{F_m} \left(\sum_{n=0}^{\infty} D_n^+ P_{mn} e^{i\kappa_n L} + \sum_{n=0}^{\infty} D_n^- P_{mn} e^{-i\kappa_n L} \right), \quad (5.31)$$

where

$$P_{mn} = \frac{1}{\gamma_n^2 - \lambda_m^2} \{ \gamma_n J_n + \gamma_n \cos[\lambda_m(b - a)] I_n - \lambda_m \sin[\lambda_m(b - a)] W_n \}, \quad (5.32)$$

and

$$J_n = -r \cos[\gamma_n(h - a)] + s\gamma_n \sin[\gamma_n(h - a)], \quad (5.33)$$

$$I_n = r \cos[\gamma_n(h - b)] - s\gamma_n \sin[\gamma_n(h - b)], \quad (5.34)$$

$$W_n = r \sin[\gamma_n(h - b)] + s\gamma_n \cos[\gamma_n(h - b)]. \quad (5.35)$$

The continuity condition of the fluid pressure at matching interface is

$$\psi_3(-L, y) = \psi_4(-L, y), \quad a \leq y \leq b. \quad (5.36)$$

Using equations (5.13) and (5.19) in (5.36), we get

$$\sum_{n=0}^{\infty} C_n \cos[\lambda_n(y - a)] = \sum_{n=0}^{\infty} D_n^+ Y_n e^{i\kappa_n L} + \sum_{n=0}^{\infty} D_n^- Y_n e^{-i\kappa_n L}. \quad (5.37)$$

On multiplying equation (5.37) with $\cos[\lambda_m(y - a)]$, integrating the result from a to b and employing the orthogonality relation (5.17), we obtain

$$C_m = \frac{1}{F_m} \left(\sum_{n=0}^{\infty} D_n^+ Q_{mn} e^{i\varsigma_n L} + \sum_{n=0}^{\infty} D_n^- Q_{mn} e^{-i\varsigma_n L} \right), \quad (5.38)$$

where

$$Q_{mn} = \frac{1}{\gamma_n^2 - \lambda_m^2} \{ \gamma_n U_n + \gamma_n \cos[\lambda_m(b - a)] N_n - \lambda_m \sin[\lambda_m(b - a)] V_n \}, \quad (5.39)$$

and

$$U_n = r \cos[\gamma_n(h + a)] - s\gamma_n \sin[\gamma_n(h + a)], \quad (5.40)$$

$$N_n = -r \cos[\gamma_n(h + b)] + s\gamma_n \sin[\gamma_n(h + b)], \quad (5.41)$$

$$V_n = r \sin[\gamma_n(h + b)] + s\gamma_n \cos[\gamma_n(h + b)]. \quad (5.42)$$

In order to determine the unknown coefficients for duct region \mathcal{R}_4 at $x = -L$, the subsequent matching condition of normal velocities are applied at interface:

$$\psi_{4x}(-L, y) = \begin{cases} \frac{-\mu}{\kappa} \psi_4(-L, y), & -h \leq y \leq -b, \\ \psi_{2x}(-L, y), & -b \leq y \leq -a, \\ \psi_{1x}(-L, y), & -a \leq y \leq a, \\ \psi_{3x}(-L, y), & a \leq y \leq b, \\ \frac{-\mu}{\kappa} \psi_4(-L, y), & b \leq y \leq h. \end{cases} \quad (5.43)$$

Therefore, using equations (5.8), (5.12), (5.13) and (5.19) in (5.43), we obtain

$$-\sum_{n=0}^{\infty} D_n^+ \varsigma_n Y_n e^{i\varsigma_n L} + \sum_{n=0}^{\infty} D_n^- \varsigma_n Y_n e^{-i\varsigma_n L} = \begin{cases} \frac{i\mu}{\kappa} \left(\sum_{n=0}^{\infty} D_n^+ Y_n e^{i\varsigma_n L} + \sum_{n=0}^{\infty} D_n^- Y_n e^{-i\varsigma_n L} \right), & -h \leq y \leq -b, \\ -\sum_{n=0}^{\infty} B_n \varkappa_n \cos[\lambda_n(y + a)], & -b \leq y < -a, \\ 1 - \sum_{n=0}^{\infty} A_n \vartheta_n \cos[\tau_n(y + a)], & -a \leq y < a, \\ -\sum_{n=0}^{\infty} C_n \varkappa_n \cos[\lambda_n(y - a)], & a \leq y < b, \\ \frac{i\mu}{\kappa} \left(\sum_{n=0}^{\infty} D_n^+ Y_n e^{i\varsigma_n L} + \sum_{n=0}^{\infty} D_n^- Y_n e^{-i\varsigma_n L} \right), & b \leq y \leq h, \end{cases} \quad (5.44)$$

which, when multiplied by Y_m , integrated from $-h$ to h , and used in accordance with the orthogonality relation (5.21), yields

$$\begin{aligned}
 -D_m^+ e^{i\varsigma_m L} + D_m^- e^{-i\varsigma_m L} = \frac{1}{\varsigma_m G_m} \left\{ R_{0m} - \sum_{n=0}^{\infty} A_n \vartheta_n R_{nm} - \sum_{n=0}^{\infty} B_n \varkappa_n P_{nm} \right. \\
 \left. - \sum_{n=0}^{\infty} C_n \varkappa_n Q_{nm} + \frac{i\mu}{\kappa} \sum_{n=0}^{\infty} D_n S_{mn} e^{i\varsigma_n L} + \frac{i\mu}{\kappa} \sum_{n=0}^{\infty} D_n^- S_{mn} e^{-i\varsigma_n L} \right. \\
 \left. + \frac{i\mu}{\kappa} \sum_{n=0}^{\infty} D_n H_{mn} e^{i\varsigma_n L} + \frac{i\mu}{\kappa} \sum_{n=0}^{\infty} D_n^- H_{mn} e^{-i\varsigma_n L} \right\}, \quad (5.45)
 \end{aligned}$$

where

$$H_{mn} = \int_{-h}^{-b} Y_{4m}(y) Y_{4n}(y) dy \quad \text{and} \quad S_{mn} = \int_b^h Y_{4m}(y) Y_{4n}(y) dy.$$

Similarly, the continuity conditions of the fluid pressure at $x = L$ are

$$\psi_6(L, y) = \psi_4(L, y), \quad -a \leq y \leq a. \quad (5.46)$$

On using equations (5.8) and (5.19) in (5.46), we get

$$\sum_{n=0}^{\infty} T_n \cos[\tau_n(y+a)] = \sum_{n=0}^{\infty} D_n^+ Y_n e^{-i\varsigma_n L} + \sum_{n=0}^{\infty} D_n^- Y_n e^{i\varsigma_n L}. \quad (5.47)$$

The multiplying of equation (5.47) with $\cos[\tau_m(y+a)]$, and integrating it from $-a$ to a and then employing the orthogonality relation (5.10), we have the form

$$T_m = \frac{1}{a\varepsilon_m} \left(\sum_{n=0}^{\infty} D_n^+ R_{mn} e^{-i\varsigma_n L} + \sum_{n=0}^{\infty} D_n^- R_{mn} e^{i\varsigma_n L} \right). \quad (5.48)$$

The matching condition of the fluid pressure at interface is

$$\psi_7(L, y) = \psi_4(L, y), \quad -b \leq y \leq -a. \quad (5.49)$$

On using equations (5.12) and (5.19) in (5.49), we get

$$\sum_{n=0}^{\infty} M_n \cos[\lambda_n(y+a)] = \sum_{n=0}^{\infty} D_n^+ Y_n e^{-i\varsigma_n L} + \sum_{n=0}^{\infty} D_n^- Y_n e^{i\varsigma_n L}. \quad (5.50)$$

Again, multiplying equation (5.50) with $\cos[\lambda_m(y + b)]$, integration it from $-b$ to $-a$ and applying the orthogonality relation (5.17), it is found that

$$M_m = \frac{1}{F_m} \left(\sum_{n=0}^{\infty} D_n^+ P_{mn} e^{-i\zeta_n L} + \sum_{n=0}^{\infty} D_n^- P_{mn} e^{i\zeta_n L} \right), \quad (5.51)$$

The continuity condition of the fluid pressure at $x = L$ is

$$\psi_5(L, y) = \psi_4(L, y), \quad a \leq y \leq b. \quad (5.52)$$

Using equations (5.13) and (5.19) in (5.52), we get

$$\sum_{n=0}^{\infty} K_n \cos[\lambda_n(y - a)] = \sum_{n=0}^{\infty} D_n^+ Y_n e^{-i\zeta_n L} + \sum_{n=0}^{\infty} D_n^- Y_n e^{i\zeta_n L}. \quad (5.53)$$

On multiplying equation (5.53) with $\cos[\lambda_m(y - a)]$, integrating the result from a to b and employing the orthogonality relation (5.17), we get

$$K_m = \frac{1}{F_m} \left(\sum_{n=0}^{\infty} D_n^+ Q_{mn} e^{-i\zeta_n L} + \sum_{n=0}^{\infty} D_n^- Q_{mn} e^{i\zeta_n L} \right). \quad (5.54)$$

In order to find the unknown coefficients for region \mathcal{R}_4 , at $x = L$, the related matching condition of normal velocities are used at interface

$$\psi_{4x}(L, y) = \begin{cases} \frac{\mu}{\kappa} \psi_4(L, y), & -h \leq y \leq -b, \\ \psi_{7x}(L, y), & -b \leq y \leq -a, \\ \psi_{6x}(L, y), & -a \leq y \leq a, \\ \psi_{5x}(L, y), & a \leq y \leq b, \\ \frac{\mu}{\kappa} \psi_4(L, y), & b \leq y \leq h. \end{cases} \quad (5.55)$$

Therefore, using equations (5.8), (5.12), (5.13) and (5.19) into (5.55), we obtain

$$\begin{aligned}
 & -\sum_{n=0}^{\infty} D_n^+ \varsigma_n Y_n e^{-i\varsigma_n L} + \sum_{n=0}^{\infty} D_n^- \varsigma_n Y_n e^{i\varsigma_n L} \\
 & = \begin{cases} \frac{-i\mu}{\kappa} \left(\sum_{n=0}^{\infty} D_n^+ Y_n e^{-i\varsigma_n L} + \sum_{n=0}^{\infty} D_n^- Y_n e^{i\varsigma_n L} \right), & -h \leq y \leq -b, \\ \sum_{n=0}^{\infty} M_n \varkappa_n \cos[\lambda_n(y+a)], & -b \leq y < -a, \\ \sum_{n=0}^{\infty} T_n \vartheta_n \cos[\tau_n(y+a)], & -a \leq y < a, \\ \sum_{n=0}^{\infty} K_n \varkappa_n \cos[\lambda_n(y-a)], & a \leq y < b, \\ \frac{-i\mu}{\kappa} \left(\sum_{n=0}^{\infty} D_n^+ Y_n e^{-i\varsigma_n L} + \sum_{n=0}^{\infty} D_n^- Y_n e^{i\varsigma_n L} \right), & b \leq y \leq h, \end{cases} \quad (5.56)
 \end{aligned}$$

which on multiplying with Y_m , integrating it from $-h$ to h and utilizing the orthogonality relation (5.56) yields

$$\begin{aligned}
 -D_m^+ e^{-i\varsigma_m L} + D_m^- e^{i\varsigma_m L} & = \frac{1}{\varsigma_m G_m} \left\{ \sum_{n=0}^{\infty} T_n \vartheta_n R_{nm} + \sum_{n=0}^{\infty} M_n \varkappa_n P_{nm} \right. \\
 & + \sum_{n=0}^{\infty} K_n \varkappa_n Q_{nm} - \frac{i\mu}{\kappa} \sum_{n=0}^{\infty} D_n S_{mn} e^{-i\varsigma_n L} - \frac{i\mu}{\kappa} \sum_{n=0}^{\infty} D_n^- S_{mn} e^{i\varsigma_n L} \\
 & \left. - \frac{i\mu}{\kappa} \sum_{n=0}^{\infty} D_n H_{mn} e^{-i\varsigma_n L} - \frac{i\mu}{\kappa} \sum_{n=0}^{\infty} D_n^- H_{mn} e^{i\varsigma_n L} \right\}. \quad (5.57)
 \end{aligned}$$

Solving (5.45) and (5.57) simultaneously, we get

$$\begin{aligned}
 D_m^{\pm} & = \frac{\mp 1}{4\varsigma_m G_m \cos(\varsigma_m L)} \left\{ R_{0m} - \frac{2\mu}{\kappa} \sum_{n=0}^{\infty} D_n^+ (S_{mn} + H_{mn}) \sin(\varsigma_n L) \right. \\
 & + \frac{2\mu}{\kappa} \sum_{n=0}^{\infty} D_n^- (S_{mn} + H_{mn}) \sin(\varsigma_n L) + \sum_{n=0}^{\infty} (T_n - A_n) \vartheta_n R_{nm} \\
 & \left. + \sum_{n=0}^{\infty} (M_n - B_n) \varkappa_n P_{nm} + \sum_{n=0}^{\infty} (K_n - C_n) \varkappa_n Q_{nm} \right\} \\
 & - \frac{1}{4i\varsigma_m G_m \sin(\varsigma_m L)} \left\{ R_{0m} + \frac{2i\mu}{\kappa} \sum_{n=0}^{\infty} D_n^+ (S_{mn} + H_{mn}) \cos(\varsigma_n L) \right. \\
 & + \frac{2i\mu}{\kappa} \sum_{n=0}^{\infty} D_n^- (S_{mn} + H_{mn}) \cos(\varsigma_n L) - \sum_{n=0}^{\infty} (T_n + A_n) \vartheta_n R_{nm} \\
 & \left. - \sum_{n=0}^{\infty} (M_n + B_n) \varkappa_n P_{nm} - \sum_{n=0}^{\infty} (K_n + C_n) \varkappa_n Q_{nm} \right\}. \quad (5.58)
 \end{aligned}$$

In this way, equation (5.58) lead to infinite system of equations in which D_m^+ and D_m^- ; $m = 0, 1, 2, \dots$, are unknowns.

To determine the unknown model coefficients, these are truncated and inverted.

Following the acquiring of the values of D_m^+ and D_m^- ; $m = 0, 1, 2, \dots$ the quantities $\{A_m, B_m, C_m, T_m, M_m, K_m\}$; $m = 0, 1, 2, \dots$ are found easily by using equations (5.26), (5.31), (5.38), (5.48), (5.51) and (5.54).

It is worth noting that the vertical step-discontinuities are transferred to rigid/hard ones by setting $\mu = 0$ in equation (5.58).

5.3 Energy Balance

The energy flux/power inside the duct regions is defined by the formula given below:

$$\frac{\partial \mathcal{E}}{\partial t} = \frac{1}{2} Re \left\{ i \int_{\Omega} \psi \left(\frac{\partial \psi}{\partial x} \right)^* dy \right\}, \quad (5.59)$$

where, superscript asterisk (*) denotes the complex conjugate.

From the definition of energy flux/power, the incident power is found to be

$$\mathcal{P}_{inc} = a.$$

Likewise, the power/energy flux components in duct regions are:

$$\mathcal{P}_1 = \frac{1}{2} Re \left\{ \sum_{n=0}^{\infty} |A_n|^2 \vartheta_n \varepsilon_n \right\}, \quad (5.60)$$

$$\mathcal{P}_2 = \frac{1}{2a} Re \left\{ \sum_{n=0}^{\infty} |B_n|^2 \varkappa_n F_n \right\}, \quad (5.61)$$

$$\mathcal{P}_3 = \frac{1}{2a} Re \left\{ \sum_{n=0}^{\infty} |C_n|^2 \varkappa_n F_n \right\}, \quad (5.62)$$

$$\mathcal{P}_5 = \frac{1}{2a} Re \left\{ \sum_{n=0}^{\infty} |K_n|^2 \varkappa_n F_n \right\}, \quad (5.63)$$

$$\mathcal{P}_6 = \frac{1}{2} Re \left\{ \sum_{n=0}^{\infty} |T_n|^2 \vartheta_n \varepsilon_n \right\}, \quad (5.64)$$

and

$$\mathcal{P}_7 = \frac{1}{2a} Re \left\{ \sum_{n=0}^{\infty} |M_n|^2 \varkappa_n F_n \right\}. \quad (5.65)$$

It is important to note that the power supplied to the system is equal to the sum of scattering powers in different duct regions, that is;

$$\mathcal{P}_{inc} = \mathcal{P}_1 + \mathcal{P}_2 + \mathcal{P}_3 + \mathcal{P}_5 + \mathcal{P}_6 + \mathcal{P}_7, \quad (5.66)$$

which is known as conserved power identity. We can scale the incident power at unity for analysis purposes by dividing equation (5.66) by a which is,

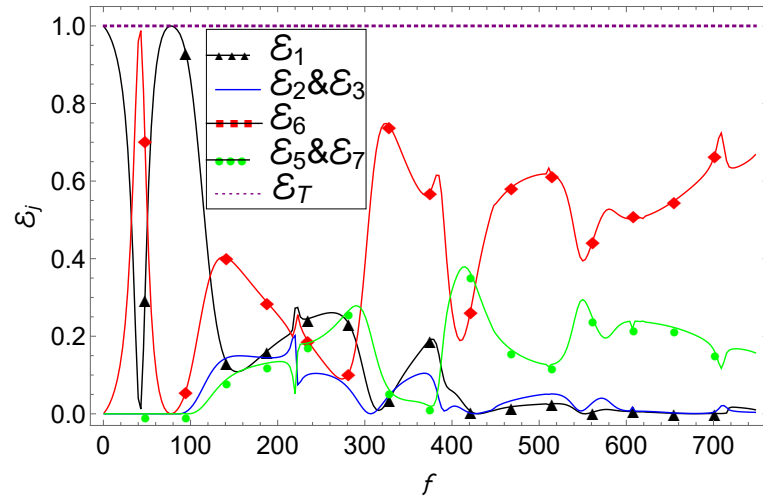
$$1 = \mathcal{E}_1 + \mathcal{E}_2 + \mathcal{E}_3 + \mathcal{E}_5 + \mathcal{E}_6 + \mathcal{E}_7, \quad (5.67)$$

where, $\mathcal{E}_j = \mathcal{P}_j/a ; j = 1, 2, 3, 5, 6, 7$.

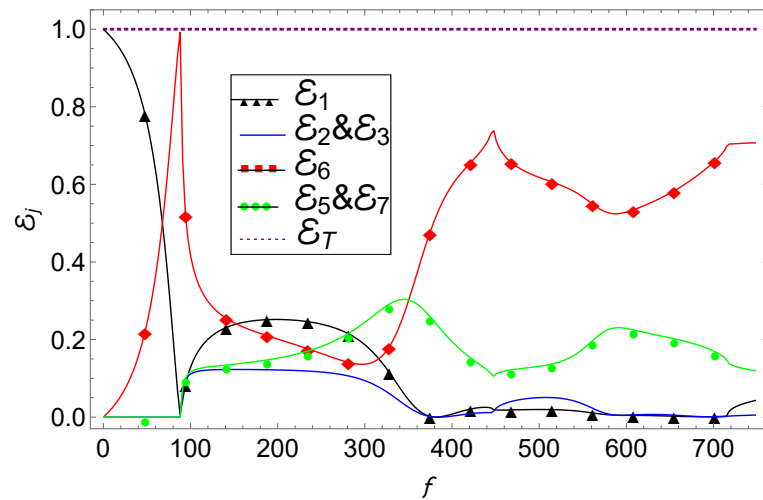
Note that $\mathcal{E}_j, j = 1, 2, 3, 5, 6, 7$ denote the energy/power flux components in duct sections $\mathcal{R}_j; j = 1, 2, 3, 5, 6, 7$ for which the incident power is being scaled at unity.

5.4 Numerical Results and Discussions

This section provides graphical illustration of the scattered fields. For the purpose, we truncate and solve the infinite system given by equation (5.58) to compute unknown coefficients to be used in eigenfunction expansion of respective field potentials. The underlying discussion is mainly focused in three ways while considering the waveguide structure with ($b \neq h$) and without step-discontinuities ($b = h$).



(a)



(b)

FIGURE 5.2: Radiated energy versus frequency (f) for all Robin type (mixed) bounding walls (a) with step-discontinuity ($b \neq h$) (b) without step-discontinuity ($b = h$) where $\bar{a} = 0.24m, \bar{b} = 3\bar{a}, p = q = r = s = \mu = \kappa = 1$ and $N = 10$.

The current study's main idea is to maintain pressure and normal velocity continuity at discrete transverse points across an axial duct discontinuity, as opposed to analytical matching, which aims to consistently enforce continuity conditions. As a result, numerical matching cannot be expected to be as accurate as analytical matching; however, expectations should in principle tend toward the approximation obtained while matching analytically as long as the number and location of the points at which numerical matching takes place are carefully chosen. This

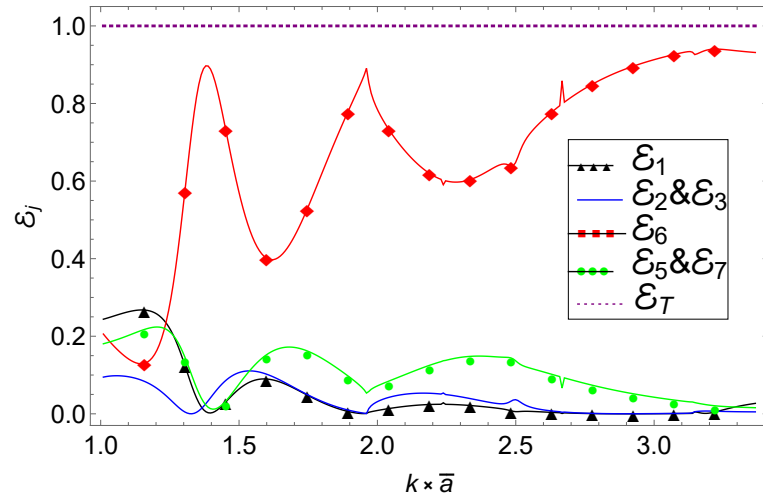
is true for both numerical and analytical mode matching; prior to matching, an adequate number of higher order axial modes must be predicted correctly so that the sound's pressure and velocity fields are properly represented, particularly on both sides of a discontinuity.

Figures 5.2(a) and 5.2(b) are plotted for power distribution against frequency regime f with ($b \neq h$) and without step-discontinuity ($b = h$), respectively. We have observed that the reflected power of \mathcal{R}_1 goes to minimum and transmitted power of region \mathcal{R}_6 behaves conversely after $f = 100Hz$.

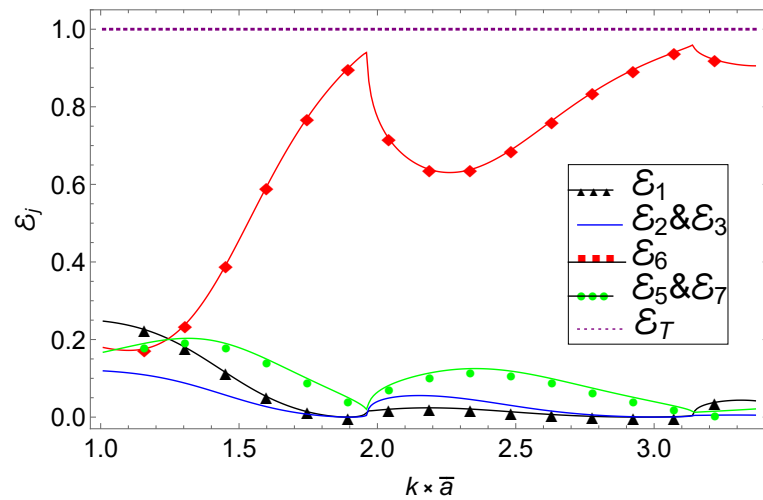
However, the sum of the reflected and transmitted powers is unity that successfully testifies the conserve power identity (5.67), as shown in Figures 5.2(a) and 5.2(b).

Following are the key observations:

- The presence of vertical discontinuity reveals higher amount of energy to be observed as compared in the absence of discontinuity.
- The number of cut-on modes reduce to fewer one when step of discontinuity is removed. However, more cut-on modes appeared at low frequencies ($f < 300Hz$) which show that more energy is absorbed.
- Out of all reflected regions, \mathcal{R}_j ; $j = 1, 2, 3$, \mathcal{R}_1 is the dominating region, where most of the power is reflected. Similarly, out of all transmitted regions, \mathcal{R}_j ; $j = 5, 6, 7$, \mathcal{R}_6 is the dominating region.
- It is observed that after certain level of frequency, say $300Hz$, most of the energy is transmitted through regions, \mathcal{R}_j ; $j = 5, 6, 7$.
- It can also be observed that a certain significant amount of absorption of energy occurs in Figure 5.2(a).
- Total energy remains conserved for both cases, when ($b \neq h$) and ($b = h$).
- For different frequencies, a tabular description of the power propagating in different duct sections, \mathcal{R}_j ; ($j = 1 - 3, 5 - 7$) of the trifurcated lined duct contained by an expansion chamber is shown (Table 5.1 and Table 5.2).



(a)



(b)

FIGURE 5.3: Radiated energy versus $(k \times \bar{a})$ for all Robin type (mixed) bounding walls (a) with step-discontinuity ($b \neq h$) (b) without step-discontinuity ($b = h$) where $\bar{a} = 0.24m, \bar{b} = 3\bar{a}, p = q = r = s = \mu = \kappa = 1$ and $N = 10$.

The same depiction is discussed in Figures 5.3(a) and 5.3(b) where power distribution is observed versus height of the duct $a = k \times \bar{a}$ in region \mathcal{R}_1 , which indeed is a region of incident.

We see that most of the energy is transmitted in region \mathcal{R}_6 when the duct height is increased after $k \times \bar{a} = 1.3m$.

However, the sum of the reflected and transmitted powers is unity that satisfies the conserve power identity (5.67), as shown in Figures 5.3(a) and 5.3(b).

The key findings are summarized below:

- The number of cut-on modes become fewer when step of discontinuity is removed. Also more cut-on modes are observed for larger duct heights, which show that more energy is absorbed.
- Out of all reflected regions, \mathcal{R}_j ; $j = 1, 2, 3$, \mathcal{R}_1 is the dominating region .
- The region \mathcal{R}_1 is dominated among all other reflected regions, whereas region \mathcal{R}_6 is dominated in transmitted regions.
- It is observed that after certain level of the duct height ($k \times \bar{a} > 1.15274m$), most of the energy is transmitted through regions, \mathcal{R}_j ; $j = 5, 6, 7$.
- It is also noted that when the dimensions of the duct spacing $k \times \bar{a}$ rise, the values of the reflection decrease.
- Total energy remains conserved for either case.
- In tabular form (Table 5.3 and Table 5.4), a brief description of the radiated power in different duct regions, \mathcal{R}_j ; ($j = 1 - 3, 5 - 7$) of the trifurcated lined duct contained by an expansion chamber is presented for different symmetric heights.

Figures 5.4(a) and 5.4(b) are plotted to see the reflected power behavior against frequency regime ($1Hz - 750Hz$), with and without multiple step-discontinuities.

These Figures depicts that before $f = 300Hz$ we observe a prominent reflection for all impedance, rigid and soft cases.

Following are the key observations:

- More cut-on modes are observed for discontinuous case whereas, the cut-on modes are reduced considerably when step of discontinuities are removed.
- More energy is absorbed in case of step-discontinuity, on the other hand, less amount of energy is absorbed when step of discontinuity is removed.

TABLE 5.1: Discontinuous trifurcated waveguide, when $\bar{a} = 0.24m$, $\bar{b} = 3\bar{a}$, $\bar{h} = 5\bar{a}$, $p = q = r = s = \mu = \kappa = 1$ and $\bar{L} = 0.25m$ by varying frequency.

f	\mathcal{E}_1	\mathcal{E}_2	\mathcal{E}_3	\mathcal{E}_6	\mathcal{E}_5	\mathcal{E}_7	\mathcal{E}_T
10	0.958932	0	0	0.0410685	0	0	1
40	0.0402103	0	0	0.95979	0	0	1
100	0.862736	0.0149758	0.0149758	0.10624	0.000536415	0.000536415	1
130	0.228493	0.125491	0.125491	0.393489	0.0635184	0.0635184	1
160	0.112258	0.149429	0.149429	0.362452	0.113215	0.113215	1
220	0.272394	0.201607	0.201607	0.220818	0.0517868	0.0517868	1
310	0.0206063	0.00211088	0.00211088	0.626226	0.174473	0.174473	1
400	0.0587968	0.0188314	0.0188314	0.265664	0.318938	0.318938	1
550	0.000504559	0.00807712	0.00807712	0.394229	0.294556	0.294556	1
640	0.00268968	0.00441115	0.00441115	0.528028	0.23023	0.23023	1
700	0.000880371	0.00404187	0.00404187	0.657877	0.16658	0.16658	1
745	0.0117687	0.00391965	0.00391965	0.660891	0.159751	0.159751	1

TABLE 5.2: Planar trifurcated waveguide, when $\bar{a} = 0.24m$, $\bar{b} = \bar{h} = 3\bar{a}$, $p = q = r = s = \mu = \kappa = 1$ and $\bar{L} = 0.25m$ by varying frequency.

f	\mathcal{E}_1	\mathcal{E}_2	\mathcal{E}_3	\mathcal{E}_6	\mathcal{E}_5	\mathcal{E}_7	\mathcal{E}_T
10	0.976583	0	0	0.0234168	0	0	1
40	0.844128	0	0	0.155872	0	0	1
100	0.12856	0.111061	0.111061	0.41693	0.116195	0.116195	1
130	0.21816	0.122274	0.122274	0.273464	0.131914	0.131914	1
160	0.243915	0.122757	0.122757	0.232605	0.138983	0.138983	1
220	0.24974	0.12025	0.12025	0.18683	0.161466	0.161466	1
310	0.165501	0.084435	0.084435	0.14222	0.261705	0.261705	1
400	0.00775665	0.00261788	0.00261788	0.597654	0.194677	0.194677	1
550	0.0140883	0.0340809	0.0340809	0.567793	0.174979	0.174979	1
640	0.00330787	0.00658215	0.00658215	0.565428	0.20905	0.20905	1
700	0.0012613	0.000544077	0.000544077	0.656883	0.170384	0.170384	1
745	0.0412523	0.0050833	0.0050833	0.706897	0.120842	0.120842	1

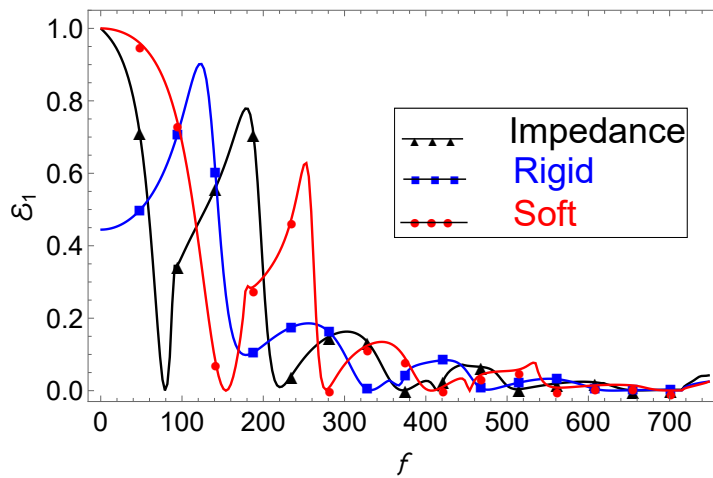
TABLE 5.3: Discontinuous trifurcated waveguide, when $f = 230Hz$, $\bar{b} = 3\bar{a}$, $\bar{h} = 5\bar{a}$, $p = q = r = s = \mu = \kappa = 1$ and $\bar{L} = 0.25m$ by varying height ($k \times \bar{a}$).

$k \times \bar{a}$	\mathcal{E}_1	\mathcal{E}_2	\mathcal{E}_3	\mathcal{E}_6	\mathcal{E}_5	\mathcal{E}_7	\mathcal{E}_T
1.0097	0.243903	0.0946318	0.0946318	0.205654	0.180589	0.180589	1
1.27895	0.175393	0.0181647	0.0181647	0.419297	0.18449	0.18449	1
1.40517	0.00338912	0.048954	0.048954	0.874791	0.0119559	0.0119559	1
1.60711	0.0892234	0.100162	0.100162	0.398523	0.155964	0.155964	1
2.00257	0.00893343	0.0323457	0.0323457	0.780686	0.0728446	0.0728446	1
2.22975	0.0245811	0.0509755	0.0509755	0.604486	0.134491	0.134491	1
2.44852	0.0129778	0.0258586	0.0258586	0.643113	0.146096	0.146096	1
2.70095	0.00179481	0.00329189	0.00329189	0.816331	0.0876454	0.0876454	1
2.80192	0.000361318	0.000741054	0.000741054	0.859219	0.0694688	0.0694688	1
3.00386	0.000231951	0.000592558	0.000592558	0.913753	0.042415	0.042415	1
3.2058	0.00260713	0.00703003	0.00703003	0.939682	0.0218255	0.0218255	1
3.34884	0.0251088	0.00512428	0.00512428	0.932443	0.0160996	0.0160996	1

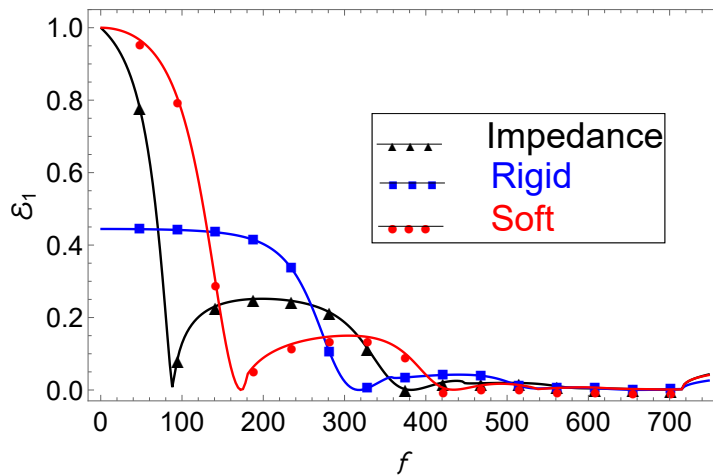
TABLE 5.4: Planar trifurcated waveguide, when $f = 230Hz$, $\bar{b} = \bar{h} = 3\bar{a}$, $p = q = r = s = \mu = \kappa = 1$ and $\bar{L} = 0.25m$ by varying height ($k \times \bar{a}$).

$k \times \bar{a}$	\mathcal{E}_1	\mathcal{E}_2	\mathcal{E}_3	\mathcal{E}_6	\mathcal{E}_5	\mathcal{E}_7	\mathcal{E}_T
1.0097	0.247425	0.119255	0.119255	0.179454	0.167305	0.167305	1
1.27895	0.190061	0.092207	0.092207	0.221003	0.202261	0.202261	1
1.40517	0.136594	0.0669746	0.0669746	0.334544	0.197456	0.197456	1
1.60711	0.0503648	0.0255517	0.0255517	0.604299	0.147116	0.147116	1
2.00257	0.0179779	0.0410638	0.0410638	0.768637	0.0656289	0.0656289	1
2.22975	0.0236446	0.0534853	0.0534853	0.631954	0.118715	0.118715	1
2.44852	0.015538	0.03384	0.03384	0.673735	0.121523	0.121523	1
2.70095	0.00409327	0.0101519	0.0101519	0.800471	0.087566	0.087566	1
2.80192	0.00150671	0.00460158	0.00460158	0.847926	0.070682	0.070682	1
3.00386	0.000212458	0.000151373	0.000151373	0.921059	0.0392129	0.0392129	1
3.2058	0.036013	0.00496306	0.00496306	0.924635	0.0147127	0.0147127	1
3.34884	0.0429858	0.00521982	0.00521982	0.905862	0.0203563	0.0203563	1

- It can also be observed that, more number of cut-on modes appeared in case of soft walls with step-discontinuities. The occurrence of these cut-on modes is responsible to attenuate the sound propagating through transmitted regions.
- Figure 5.4(a) depicts that, cut-on modes reduce in number when the outer boundaries of the duct regions are rigid, which ultimately resulted a lesser attenuation. More reflected energy results that the sound attenuates in transmitted region.



(a)



(b)

FIGURE 5.4: The reflected energy versus frequency (f) containing compressible fluid (a) with step-discontinuity ($b \neq h$) (b) without step-discontinuity ($b = h$), when all the outer boundaries are Impedance, Rigid and Soft respectively, for $\bar{a} = 0.24m, \bar{b} = 3\bar{a}, \bar{h} = 5\bar{a}$ and $N = 10$.

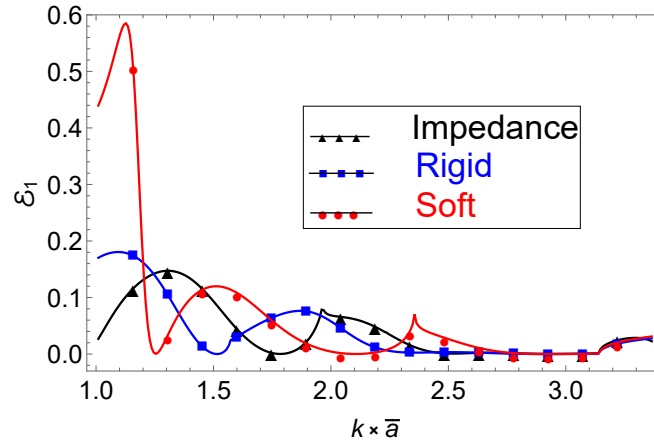
- It is observed that after certain level of frequency, say $300Hz$, the reflected energy (for all impedance, rigid and soft cases) goes to its minimum value.
- Figure 5.4(a) depicts that, cut-on modes reduce in number when the outer boundaries of the duct regions are rigid, which ultimately resulted a lesser attenuation. More reflected energy results that the sound attenuates in transmitted region.
- We've also observed that at certain cut-on (off) frequencies in certain regions, the reflected field coefficient is at its highest. This relates to the minimum downstream transmission or, most likely, the maximum attenuation produced.

Figures 5.5(a) and 5.5(b) are plotted to see the reflected power behavior against the symmetric height ($k \times \bar{a}$), with and without multiple step-discontinuities.

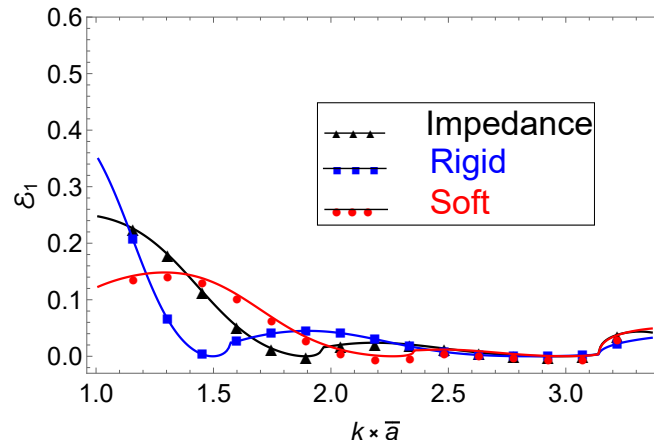
It is noted that on increasing the duct height for all impedance, rigid and soft cases, the reflected energy goes to minimum.

Following are the key observations:

- More cut-on modes are observed for discontinuous case, however, the cut-on modes are reduced considerably when step of discontinuities are removed.
- More energy is absorbed in the presence of step-discontinuity.
- It can also be observed that, most of the energy is reflected in case of soft walls with step-discontinuities.
- It is observed that after certain level of the duct height, say $2.0m$, the reflected energy for all impedance, rigid and soft case goes to its minimum value.
- More reflected energy results more sound attenuate in the transmitted region.
- It is noted that when the dimensions of the duct spacing ($k \times \bar{a}$) increase, the values of the reflection decrease.



(a)



(b)

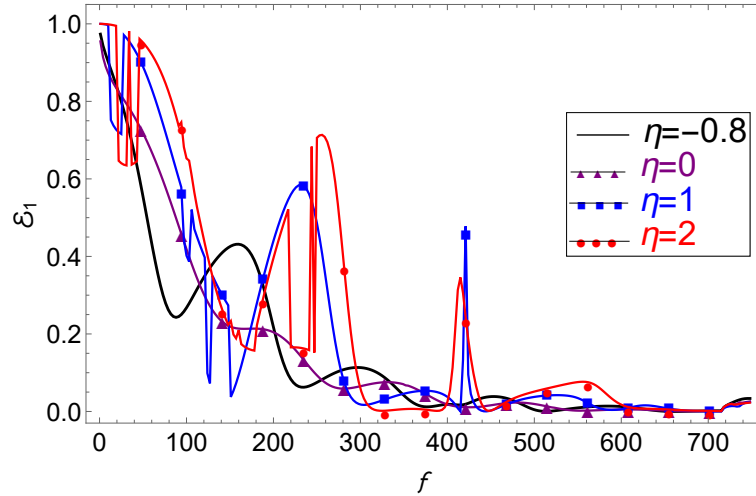
FIGURE 5.5: The reflected energy versus $(k \times \bar{a})$ containing compressible fluid (a) with step-discontinuity ($b \neq h$) (b) without step-discontinuity ($b = h$), when all the outer boundaries are Impedance, Rigid and Soft respectively, for $\bar{a} = 0.24m, \bar{b} = 3\bar{a}, \bar{h} = 5\bar{a}$ and $N = 10$.

In this part, we are interested to observe the reflected energy by considering the parametric setting as used by Rawlins [9]. The following values for the specific impedance ($\zeta = \xi + i\eta$) which is fibrous sheet, are used $\xi = 0.5, -1.0 < \eta < 3.0$ and for perforated sheet $\xi = 1, -1.0 < \eta < 3.0$.

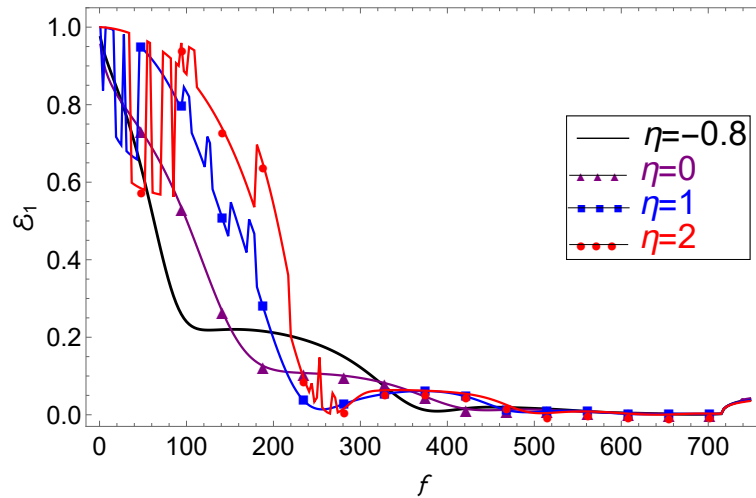
Keeping in mind that impedance parameters used in this article are related with that of Rawlins [9] as $p = 1, q = \frac{i\zeta}{k}$. Figures 5.6(a) and 5.7(a) are plotted in the presence of step-discontinuities ($b \neq h$) against frequency regime, respectively. Whereas Figures 5.6(b) and 5.7(b) are plotted in the absence of step-discontinuities

($b = h$).

It's also worth noticing that altering the porosity parameter η changes the reflected energy in the R_1 region dramatically. The conversion of eigenvalues from imaginary number to real or complex value, and vice versa, causes these variations.



(a)

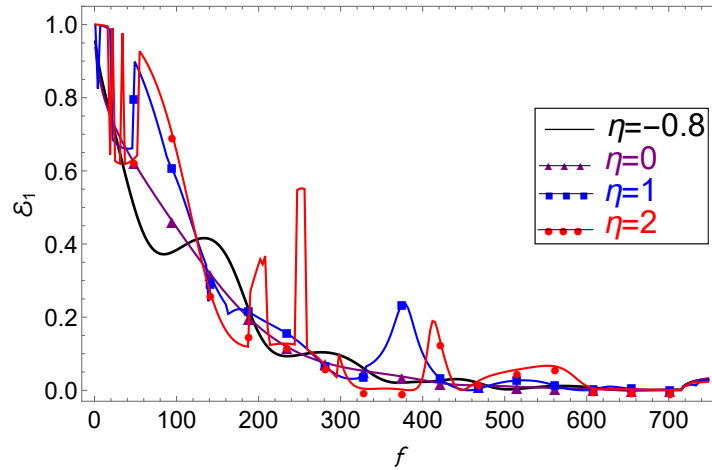


(b)

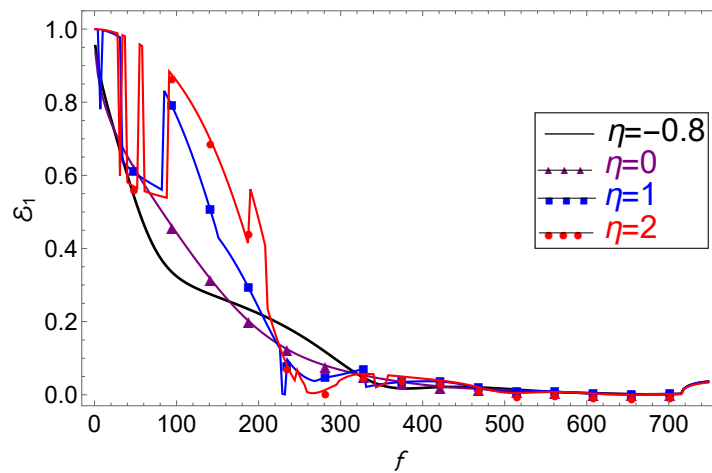
FIGURE 5.6: The reflected flux/power components against frequency containing compressible fluid in (a) discontinuous (b) continuous waveguides for $\bar{a} = 0.24m, \bar{b} = 3\bar{a}, \xi = 0.5, p = r = 1, q = s = i\zeta$ and $N = 10$.

Furthermore, for higher frequencies, bonded absorbent material has a relatively smooth frequency response. When the value of η is increased, the reflected energy curves show downward spikes. These emerge as a result of the appearance of new

cut-on duct modes. Furthermore, in the fibrous case, there are more abrupt curves than in the perforated lining, resulting in more attenuation.



(a)



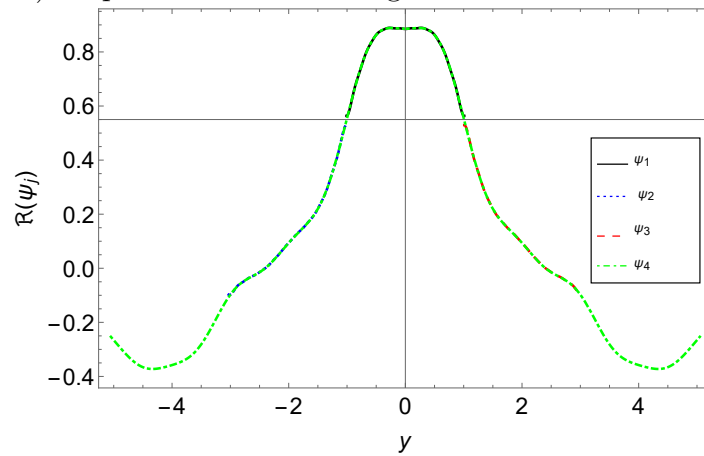
(b)

FIGURE 5.7: The reflected flux/power components against frequency containing compressible fluid in (a) discontinuous (b) continuous waveguides for $\bar{a} = 0.24m, \bar{b} = 3\bar{a}, \xi = 1, p = r = 1, q = s = i\zeta$ and $N = 10$.

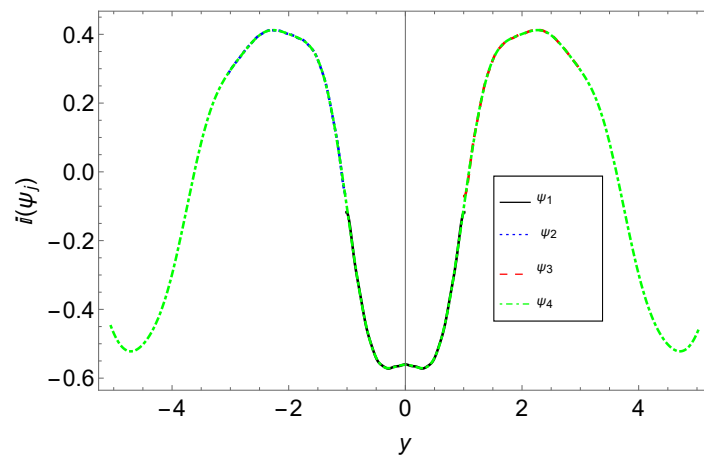
Following are the key observations:

- More fluctuations in reflected energy can be observed at low frequencies which decrease gradually as frequency increases.
- The reflected energy reduces considerably by increasing the frequency regime.
- Further, in case of no fibrous sheet, the curve pattern is quite smooth and very few modes appeared as cut-on.

- It can also be observed that, most of the energy is reflected in case of soft walls with step-discontinuities. However, the increasing value of η , increases the number of cut-on modes that results more sound attenuation propagating through transmitted region.
- It is observed that after certain level of frequency, say $300Hz$, the reflected energy for all impedance, rigid and soft case goes to its minimum value.
- It is also observed that, the cut-on modes reduced considerably when step of discontinuity is removed which results less sound attenuate in that region.
- It is also observed that the reflected field coefficient is maximum at certain cut-on (off) frequencies of various regions.



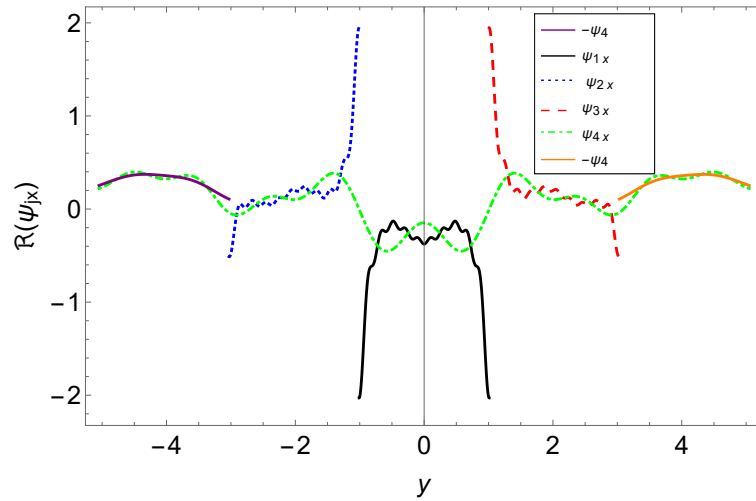
(a)



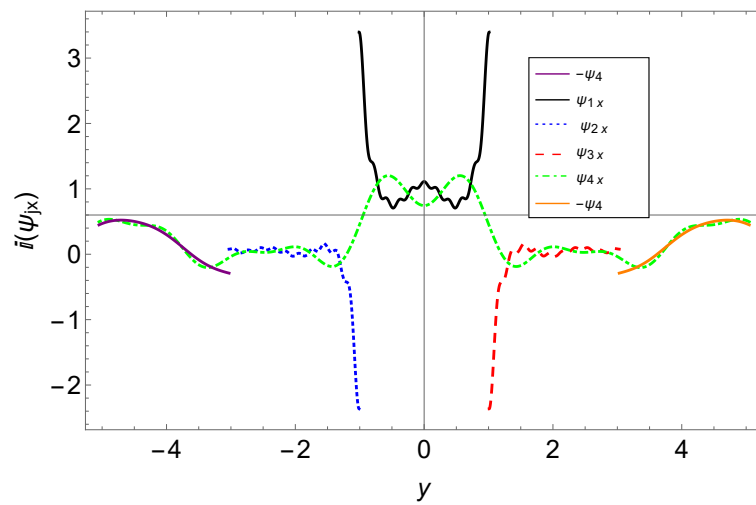
(b)

FIGURE 5.8: The real (a) and imaginary (b) parts of pressure at $x = -L$, for $\bar{a} = 0.24m$, $\bar{b} = 3\bar{a}$, $\bar{h} = 5\bar{a}$, $p = q = r = s = \mu = \kappa = 1$ and $N = 20$.

Now, the continuity conditions of pressure and normal velocity at $x = -L$ are sketched at interface to confirm the truncated solution.



(a)



(b)

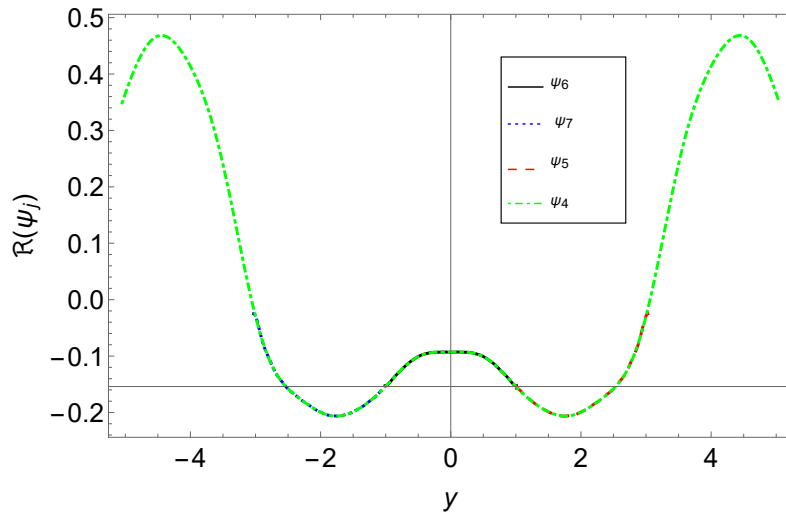
FIGURE 5.9: The real (a) and imaginary (b) parts of normal velocity at $x = -L$, for $\bar{a} = 0.24m$, $\bar{b} = 3\bar{a}$, $\bar{h} = 5\bar{a}$, $p = q = r = s = \mu = \kappa = 1$ and $N = 20$.

Through Figure 5.8, it can be seen that the real and imaginary parts of pressures $\psi_j(-L, y)$, $j = 1, 2, 3$ match exactly to the real and imaginary part of pressure $\psi_4(-L, y)$.

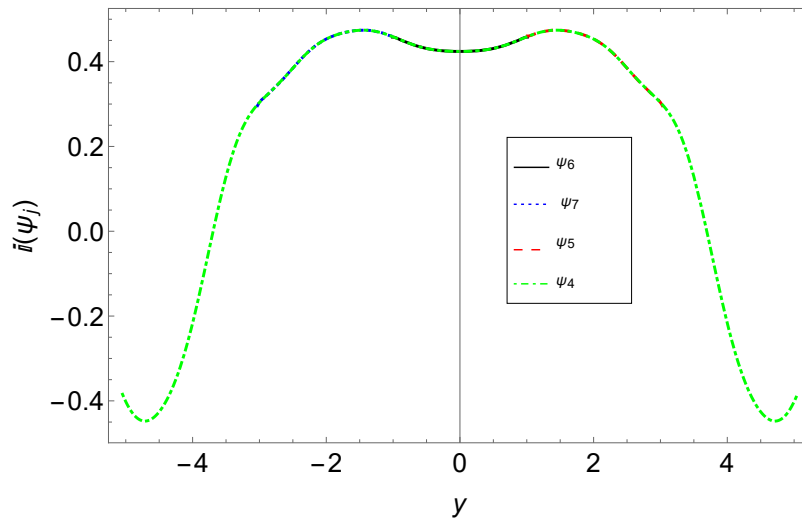
Likewise, Figure 5.9 shows that the real and imaginary parts of normal velocities $\psi_{4x}(-L, y)$, $-h < y < h$ match exactly with $\psi_{jx}(-L, y)$, $j = 1, 2, 3$ in their respective regions and $-\psi_4(-L, y)$, (for $-h < y < -b$ and $b < y < h$), respectively.

Similarly, the pressure and normal velocity continuity conditions at $x = L$ are sketched at interface to confirm the truncated solution.

Through Figure 5.10, it can be examine that the real and imaginary parts of pressures $\psi_j(L, y)$, $j = 5, 6, 7$ match exactly to the real and imaginary part of pressure $\psi_4(L, y)$.



(a)

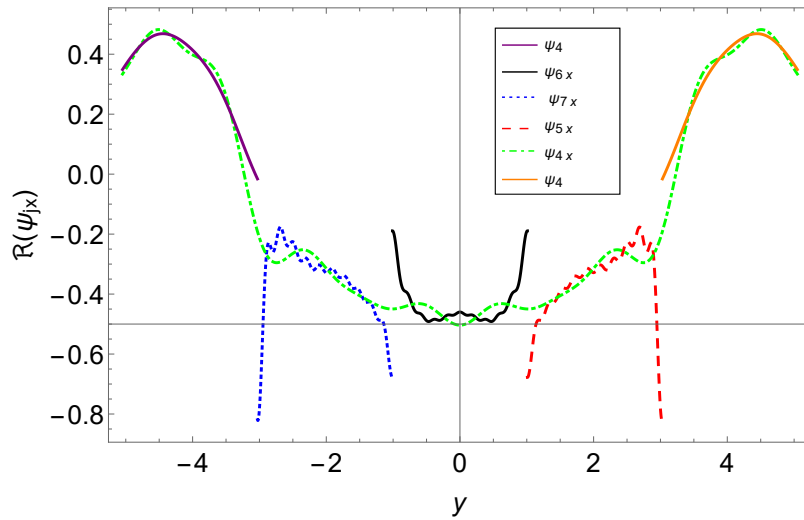


(b)

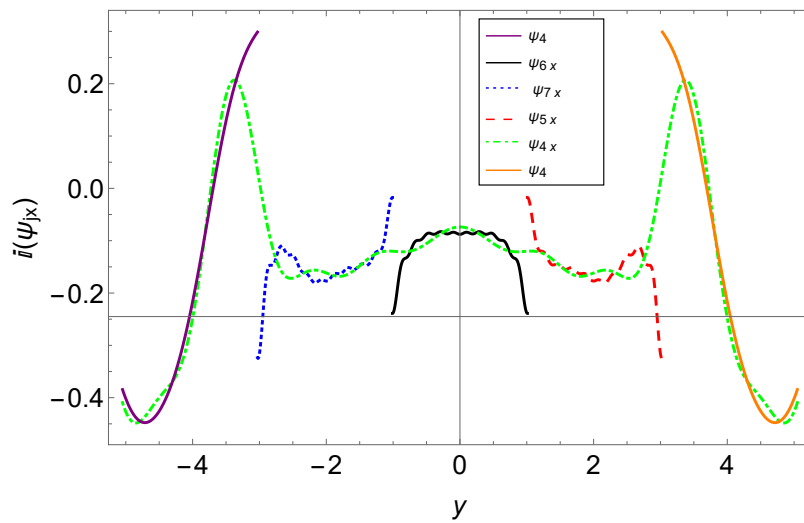
FIGURE 5.10: The real (a) and imaginary (b) parts of pressure at $x = L$, for $\bar{a} = 0.24m$, $\bar{b} = 3\bar{a}$, $\bar{h} = 5\bar{a}$, $p = q = r = s = \mu = \kappa = 1$ and $N = 20$.

Likewise, Figure 5.11 shows that the real and imaginary parts of normal velocities $\psi_{4x}(L, y)$, $-h < y < h$ match exactly with $\psi_{jx}(L, y)$, $j = 5, 6, 7$ in their respective

regions and $\psi_4(L, y)$, (for $-h < y < -b$ and $b < y < h$), respectively.



(a)



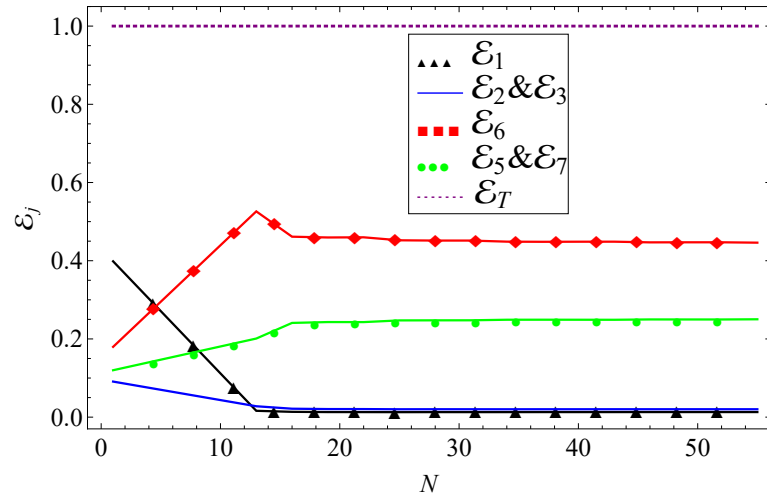
(b)

FIGURE 5.11: The real (a) and imaginary (b) parts of normal velocity at $x = L$, for $\bar{a} = 0.24m$, $\bar{b} = 3\bar{a}$, $\bar{h} = 5\bar{a}$, $p = q = r = s = \mu = \kappa = 1$ and $N = 20$.

One may consider the vertical symmetry to broken down the problem into two sub-problems as is done in [69].

The explanation related to this point is added in conclusion.

The point-wise variation of energies verses N are shown Figure 5.12, which clearly satisfy the conserve energy identity (5.67).



(a)

FIGURE 5.12: The scattering energies plotted against number of terms N for discontinuous structure where $\bar{a} = 0.24m$, $\bar{b} = 3\bar{a}$, $\bar{h} = 5\bar{a}$, $\bar{L} = 0.25m$, and $f = 530Hz$

Chapter 6

Analysis of Scattering in a Flexible Trifurcated Lined Waveguide with Step Discontinuities

In this chapter, analysis of scattering in a flexible trifurcated lined waveguide with step discontinuities is inquired through the MM approach.

Helmholtz's equation, as well as Dirichlet and higher order boundary conditions, govern the modelled problem.

Along the inner surface of the expansion chamber, an acoustically absorbent lining is added. Edge conditions are also enforced to define the physical behaviour of elastic membrane at finite edges.

The effect of the imposed edge conditions at the membrane's connections along the duct is thoroughly discussed.

The reflected and absorbed energy of scattered fields are depicted with and without structural discontinuities, as well as by varying the duct size versus various physical parameters. To prove the validity of the MM approach, appropriate numerical simulations are also performed.

6.1 Mathematical Formulation

In this section, we provide a mathematical interpretation of the scattering problem under discussion. We first discuss the physical configuration of the problem in Section 6.1.1 and then enlist the governing equations in Section 6.1.2. In Section 6.1.3, we provide the travelling wave formulations of the scattering potentials in various sections of the waveguide.

6.1.1 Geometric Configuration

Consider a two-dimensional infinite trifurcated waveguide, occupied by a compressible fluid of density $\bar{\rho}$ and speed of sound \bar{c} , having step discontinuities and an exterior in *vacou*. Precisely, assume that the waveguide consists of six subregions (see Figure 6.1)

$$\begin{aligned} \mathcal{R}_1^+ &:= \{(\bar{x}, \bar{y}) \in \mathbb{R}^2 \mid \bar{x} \in (-\infty, -\bar{L}), y \in (-\bar{a}, \bar{a})\}, \\ \mathcal{R}_2^+ &:= \{(\bar{x}, \bar{y}) \in \mathbb{R}^2 \mid \bar{x} \in (-\infty, -\bar{L}), y \in (-\bar{b}, -\bar{a})\}, \\ \mathcal{R}_3^+ &:= \{(\bar{x}, \bar{y}) \in \mathbb{R}^2 \mid \bar{x} \in (-\infty, -\bar{L}), y \in (\bar{a}, \bar{b})\}, \\ \mathcal{R}_1^- &:= \{(\bar{x}, \bar{y}) \in \mathbb{R}^2 \mid \bar{x} \in (\bar{L}, \infty), y \in (-\bar{a}, \bar{a})\}, \\ \mathcal{R}_2^- &:= \{(\bar{x}, \bar{y}) \in \mathbb{R}^2 \mid \bar{x} \in (\bar{L}, \infty), y \in (-\bar{b}, -\bar{a})\}, \\ \mathcal{R}_3^- &:= \{(\bar{x}, \bar{y}) \in \mathbb{R}^2 \mid \bar{x} \in (\bar{L}, \infty), y \in (\bar{a}, \bar{b})\}, \\ \mathcal{R}_4 &:= \{(\bar{x}, \bar{y}) \in \mathbb{R}^2 \mid \bar{x} \in (-\bar{L}, \bar{L}), y \in (-\bar{h}, \bar{h})\}. \end{aligned}$$

The waveguide is assumed to have step discontinuities at $\bar{x} = \pm L$ along vertical line segments $-\bar{h} \leq \bar{y} \leq -\bar{b}$ and $\bar{b} \leq \bar{y} \leq \bar{h}$.

An incident acoustic wave with time-harmonic dependence $e^{-i\omega t}$ is propagating in the region \mathcal{R}_1^+ from negative x -direction towards $\bar{x} = 0$, where it scatters into an infinite number of reflected and transmitted modes.

Here, $i = \sqrt{-1}$ and $\omega \in \mathbb{R}$ is the angular frequency of the incident field. Our aim here is to analyze the scattering potentials within different regions and to discuss

the energy balance in the waveguide. In specific, we are interested in the analysis of the scattered and transmitted power.

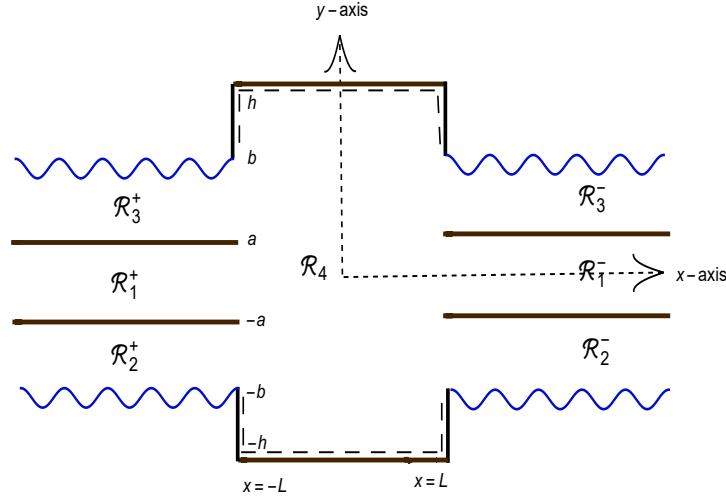


FIGURE 6.1: The geometry of the problem

Nota Bene:

For convenience, various quantities are frequently made non-dimensional using the time scale ω^{-1} and the length scale k^{-1} under the transformations

$$t = \omega \bar{t}, \quad x = k \bar{x} \quad \text{and} \quad y = k \bar{y}.$$

Here, k is the wavenumber and the superposed bar is used throughout this article to indicate dimensional quantities. Accordingly, the bar is dropped from the notation whenever the non-dimensional counterpart of a quantity is intended.

6.1.2 Governing Equations

The propagation of the time-harmonic acoustic wave in the waveguide is governed by non-dimensional Helmholtz equation

$$(\nabla^2 + 1) \psi(x, y) = 0, \quad -\infty < x < \infty, \tag{6.1}$$

where

$$\psi(x, y) := \begin{cases} \psi_j^\pm(x, y), & (x, y) \in \mathcal{R}_j^\pm, \quad j = 1, 2, 3, \\ \psi_4(x, y), & (x, y) \in \mathcal{R}_4, \end{cases}$$

represents the field potential in the waveguide.

The boundaries of different regions are defined as follows:

- (a) Regions \mathcal{R}_1^\pm have acoustically rigid boundaries.
- (b) Regions \mathcal{R}_2^\pm and \mathcal{R}_3^\pm have elastically flexible membrane type boundaries.
- (c) Region \mathcal{R}_4 has absorbing linings along boundaries and thus, impedance type conditions are imposed.

Therefore, ψ satisfies the boundary conditions

$$\frac{\partial \psi_j^+}{\partial y} = 0, \quad -\infty < x < -L, \quad y = a, \quad j = 1, 3, \quad (6.2)$$

$$\frac{\partial \psi_j^+}{\partial y} = 0, \quad -\infty < x < -L, \quad y = -a, \quad j = 1, 2, \quad (6.3)$$

$$\frac{\partial \psi_j^-}{\partial y} = 0, \quad L < x < \infty, \quad y = a, \quad j = 1, 3, \quad (6.4)$$

$$\frac{\partial \psi_j^-}{\partial y} = 0, \quad L < x < \infty, \quad y = -a, \quad j = 1, 2, \quad (6.5)$$

$$\left(\frac{\partial^2}{\partial x^2} + \mu^2 \right) \frac{\partial \psi_j^+}{\partial y} \pm \alpha \psi_j^+ = 0, \quad -\infty < x < -L, \quad y = b(\delta_{3j} - \delta_{2j}), \quad j = 3, 2, \quad (6.6)$$

$$\left(\frac{\partial^2}{\partial x^2} + \mu^2 \right) \frac{\partial \psi_j^-}{\partial y} \pm \alpha \psi_j^- = 0, \quad L < x < \infty, \quad y = b(\delta_{3j} - \delta_{2j}), \quad j = 3, 2, \quad (6.7)$$

$$\psi_4 \pm i\chi \frac{\partial \psi_4}{\partial y} = 0, \quad -L < x < L, \quad y = \pm h, \quad (6.8)$$

$$\psi_4 \pm i\chi \frac{\partial \psi_4}{\partial x} = 0, \quad x = \mp L, \quad -h \leq y \leq -b \text{ or } b \leq y \leq h, \quad (6.9)$$

where δ_{mn} represents the Kronecker's delta function and $\chi = \xi + i\eta$ is the specific impedance of the absorbing lining with acoustic resistance ξ and reactance η . It is specified that (the membrane wave-number) α and (the fluid loading parameter *in vacuo*) μ are defined by

$$\alpha = \frac{\omega^2 \rho}{Tk^3} \quad \text{and} \quad \mu := \frac{c}{c_m},$$

where ρ is the fluid density, c is the speed in compressible fluid (air), c_m is the wave speed on membrane, and T is the membrane tension [58]. In additions to the boundary conditions, the zero-displacement *edge conditions*,

$$\psi_{2y}^+(-L, -b) = 0, \tag{6.10a}$$

$$\psi_{3y}^+(-L, b) = 0, \tag{6.10b}$$

$$\psi_{2y}^-(L, -b) = 0, \tag{6.10c}$$

$$\psi_{3y}^-(L, b) = 0, \tag{6.10d}$$

are imposed at the joints between the membranes and the vertical strips to guarantee a unique solution to the boundary value problem.

These, so-called, *edge conditions* describe the physical nature of the connections and significantly affect the scattering profile of the waveguide. We refer, for instance, to [66] for a detailed discussion and a list of suitable edge conditions.

6.1.3 Traveling Wave Formulations

We discuss the traveling wave formulations for different regions separately.

6.1.3.1 Regions \mathcal{R}_1^\pm

Note that, Eqs. (6.1)–(6.5) suggest that the eigenmodes for the regions \mathcal{R}_1^\pm are

$$\psi_{1n}^\pm(x, y) = Y_{1n}(y) e^{\mp i\vartheta_n(x \pm L)}, \tag{6.11}$$

where $\vartheta_n = \sqrt{1 - \tau_n^2}$, for $n = 0, 1, 2, \dots$, is the wave-number of the n th reflected mode. Here, τ_n is the eigenvalue which satisfies the dispersion relation

$$\sin(2\tau_n a) = 0, \quad n = 0, 1, 2, \dots, \quad (6.12)$$

and $Y_{1n}(y) = \cos(\tau_n(y + a))$ is the corresponding eigenfunction. Consequently, the eigen-expansions of the potentials ψ_1^\pm are given by

$$\psi_1^+(x, y) = e^{i(x+L)} + \sum_{n=0}^{\infty} A_n^+ \psi_{1n}^+(x, y), \quad (6.13)$$

$$\psi_1^-(x, y) = \sum_{n=0}^{\infty} A_n^- \psi_{1n}^-(x, y). \quad (6.14)$$

The incident wave is defined by the first term in Eq. (6.13), whereas the reflected field is described by the summation term. The constants A_n^+ , for $n = 0, 1, 2, \dots$, are the unknown reflected mode coefficients which can be found applying the orthogonality relation

$$\int_{-a}^a Y_{1m}(y) Y_{1n}(y) dy = a \delta_{mn} \epsilon_m, \quad m, n = 0, 1, 2, \dots, \quad (6.15)$$

satisfied by the eigenfunctions $Y_{1n}(y)$ together with the matching conditions on potential ψ at the interfaces. In Eq. (6.15), $\epsilon_m = 2$ for $m = 0$ and $\epsilon_m = 1$, otherwise. The unknowns A_n^- in Eq. (6.14) can also be found in the similar fashion.

6.1.3.2 Regions \mathcal{R}_2^\pm

In regions \mathcal{R}_2^\pm , the eigenmodes can be calculated using (6.1)-(6.7) as

$$\psi_{2n}^\pm(x, y) = Y_{2n}(y) e^{\mp i \varkappa_n(x \pm L)}, \quad (6.16)$$

where $\varkappa_n = \sqrt{1 + \lambda_n^2}$, for $n = 0, 1, 2, \dots$, is the wave-number of the n th reflected mode, λ_n is the eigenvalue, and $Y_{2n}(y) = \cosh(\lambda_n(y + a))$ are the corresponding

eigenfunctions in the regions \mathcal{R}_2^\pm . Thus, the eigen-expansions of field potentials ψ_2^\pm are given by

$$\psi_2^\pm(x, y) = \sum_{n=0}^{\infty} B_n^\pm \psi_{2n}^\pm(x, y), \quad (6.17)$$

where B_n^\pm are unknown coefficients to be specified. Due to membrane type boundary at $y = -b$, eigenvalue λ_n satisfies the dispersion relation

$$(-1 - \lambda_n^2 + \mu^2) \lambda_n \sinh(\lambda_n(-b + a)) - \alpha \cosh(\lambda_n(-b + a)) = 0, \quad n = 0, 1, 2, \dots \quad (6.18)$$

The eigenfunction $Y_{2n}(y)$ satisfies the generalized orthogonality relation

$$\alpha \int_{-b}^{-a} Y_{2n}(y) Y_{2m}(y) dy = E_m \delta_{mn} - Y'_{2n}(-b) Y'_{2m}(-b), \quad m, n = 0, 1, 2, \dots \quad (6.19)$$

where

$$E_m := \frac{\alpha(b - a)}{2} + \left(\frac{1 + \lambda_m^2 - \mu^2}{2} + \lambda_m^2 \right) \sinh^2(\lambda_m(b - a)).$$

6.1.3.3 Regions \mathcal{R}_3^\pm

In regions \mathcal{R}_3^\pm , the eigenmodes are given by

$$\psi_{3n}^\pm(x, y) = Y_{3n}(y) e^{\mp i \lambda_n(x \pm L)}, \quad (6.20)$$

where $Y_{3n}(y) = \cosh(\lambda_n(y - a))$ is the eigenfunction corresponding to the eigenvalue λ_n , for $n = 0, 1, 2, \dots$, in the regions \mathcal{R}_3^\pm .

Thanks to the membrane-type boundary at $y = b$, eigenvalue λ_n satisfies the dispersion relation

$$(-1 - \lambda_n^2 + \mu^2) \lambda_n \sinh(\lambda_n(b - a)) + \alpha \cosh(\lambda_n(b - a)) = 0. \quad (6.21)$$

The functions $Y_{3n}(y)$ satisfies the generalized orthogonality relation

$$\alpha \int_a^b Y_{3n}(y) Y_{3m}(y) dy = E_m \delta_{mn} - Y'_{3n}(b) Y'_{3m}(b), \quad m, n = 0, 1, 2, \dots \quad (6.22)$$

The potential in the expanded form in \mathcal{R}_3^\pm is given by

$$\psi_3^\pm(x, y) = \sum_{n=0}^{\infty} C_n^\pm \psi_{3n}^\pm(x, y), \quad (6.23)$$

where the unknown coefficients C_n^\pm are to be specified employing the matching conditions and the generalized orthogonality relation (6.22).

6.1.3.4 Region \mathcal{R}_4

The eigen expansion of the potential ψ_4 , thanks to (6.1) and (6.8), is given by

$$\psi_4(x, y) = \sum_{n=0}^{\infty} Y_{4n}(y) (D_n^+ e^{-i\varsigma_n x} + D_n^- e^{i\varsigma_n x}), \quad (6.24)$$

where D_n^\pm , for $n = 0, 1, 2, \dots$, are constants to be determined and $\varsigma_n = \sqrt{1 - \gamma_n^2}$ is the n th mode wave-number.

Here, the eigenvalue γ_n satisfies the dispersion relation

$$(1 + \chi^2 \gamma_n^2) \sin(2\gamma_n h) + 2i\chi\gamma_n \cos(2\gamma_n h) = 0, \quad n = 0, 1, 2, \dots, \quad (6.25)$$

and the corresponding eigenfunction is written as

$$Y_{4n}(y) = \sin(\gamma_n(y + h)) + i\chi\gamma_n \cos(\gamma_n(y + h)), \quad n = 0, 1, 2, \dots.$$

Note that, function $Y_{4n}(y)$ satisfies the orthogonality relation

$$\int_{-h}^h Y_{4m}(y) Y_{4n}(y) dy = G_m \delta_{mn}, \quad m, n = 0, 1, 2, \dots, \quad (6.26)$$

where

$$G_m = \frac{1}{4\gamma_m} \left\{ 2\gamma_m \left(i\chi + 2h(1 - \chi^2 \gamma_m^2) - i\chi \cos(4h\gamma_m) \right) + (-1 - \chi^2 \gamma_m^2) \sin(4h\gamma_m) \right\}.$$

6.2 Mode-matching Solution

We adopt a mode-matching technique for solving the boundary value problem formulated in Section 6.1. It is built upon the idea of matching pressure and normal velocity modes across the regions at the interface. The unknown coefficients A_m^\pm , B_m^\pm , C_m^\pm , and D_m^\pm , for $m = 0, 1, 2, \dots$, will be found by using the matching conditions.

6.2.1 Matching Conditions at $x = -L$

It's important to note that the fluid pressure continuity conditions at the matching interface are given by

$$\psi_4(-L, y) = \begin{cases} \psi_2^+(-L, y), & -b \leq y \leq -a, \\ \psi_1^+(-L, y), & -a \leq y \leq a, \\ \psi_3^+(-L, y), & a \leq y \leq b. \end{cases} \quad (6.27)$$

Together with (6.17) and (6.24), the matching condition over $[-b, -a]$ in (6.27) furnishes

$$\sum_{n=0}^{\infty} B_n^+ Y_{2n}(y) = \sum_{n=0}^{\infty} Y_{4n}(y) (D_n^+ e^{i\varsigma_n L} + D_n^- e^{-i\varsigma_n L}). \quad (6.28)$$

Multiplying (6.28) by $Y_{2m}(y)$, integrating over $[-b, -a]$, and applying the orthogonality relation (6.19), we arrive at

$$B_m^+ = \frac{\alpha}{E_m} \sum_{n=0}^{\infty} P_{mn} (D_n^+ e^{i\varsigma_n L} + D_n^- e^{-i\varsigma_n L}) + \frac{e_1}{E_m} Y_{2m}'(-b), \quad (6.29)$$

where

$$P_{mn} = \int_{-b}^{-a} Y_{2m}(y) Y_{4n}(y) dy,$$

and

$$e_1 := \sum_{n=0}^{\infty} B_n^+ Y_{2n}'(-b).$$

Differentiating (6.17) term-by-term and invoking the edge condition (6.10a), it is

easy to find that

$$e_1 = \psi_{2y}^+(-L, -b) = 0.$$

The use of (6.13) and (6.24) together with the matching condition over $[-a, a]$ in (6.27) leads to

$$1 + \sum_{n=0}^{\infty} A_n^+ Y_{1n}(y) = \sum_{n=0}^{\infty} Y_{4n}(y) (D_n^+ e^{i\kappa_n L} + D_n^- e^{-i\kappa_n L}). \quad (6.30)$$

Therefore, by multiplying (6.30) by $Y_{1m}(y)$, integrating the resultant over $[-a, a]$, and using the orthogonality relation (6.15), we get

$$A_m^+ = \frac{-2\delta_{m0}}{\epsilon_m} + \frac{1}{a\epsilon_m} \sum_{n=0}^{\infty} R_{mn} (D_n^+ e^{i\kappa_n L} + D_n^- e^{-i\kappa_n L}), \quad (6.31)$$

where

$$R_{mn} = \int_{-a}^a Y_{1m}(y) Y_{4n}(y) dy.$$

Similarly, using equations (6.23) and (6.24) into (6.27) for the matching condition over $[a, b]$, we get

$$\sum_{n=0}^{\infty} C_n^+ Y_{3n}(y) = \sum_{n=0}^{\infty} Y_{4n}(y) (D_n^+ e^{i\kappa_n L} + D_n^- e^{-i\kappa_n L}). \quad (6.32)$$

On multiplying equation (6.32) by $Y_{3m}(y)$, integrating over $[a, b]$, and using the orthogonality relation (6.22), we get

$$C_m^+ = \frac{\alpha}{E_m} \sum_{n=0}^{\infty} Q_{mn} (D_n^+ e^{i\kappa_n L} + D_n^- e^{-i\kappa_n L}) + \frac{e_2}{E_m} Y_{3m}'(b), \quad (6.33)$$

where

$$Q_{mn} = \int_a^b Y_{3m}(y) Y_{4n}(y) dy \quad \text{and} \quad e_2 := \sum_{n=0}^{\infty} C_n^+ Y_{3n}'(b).$$

Taking derivative of (6.23) term-by-term and using the edge condition (6.10b), it is not difficult to see that

$$e_2 = \psi_{3y}^+(-L, b) = 0.$$

In terms of the normal velocities, we have the matching conditions

$$\psi_{4x}(-L, y) = \begin{cases} \frac{-1}{i\chi} \psi_4(-L, y), & -h \leq y \leq -b, \\ \psi_{2x}^+(-L, y), & -b \leq y \leq -a, \\ \psi_{1x}^+(-L, y), & -a \leq y \leq a, \\ \psi_{3x}^+(-L, y), & a \leq y \leq b, \\ \frac{-1}{i\chi} \psi_4(-L, y), & b \leq y \leq h. \end{cases} \quad (6.34)$$

Using equations (6.13), (6.17), (6.23), and (6.24) into (6.34), we obtain

$$\begin{aligned} & -\sum_{n=0}^{\infty} \varsigma_n Y_{4n}(y) (D_n^+ e^{i\varsigma_n L} - D_n^- e^{-i\varsigma_n L}) \\ &= \begin{cases} \frac{1}{\chi} \sum_{n=0}^{\infty} Y_{4n}(y) (D_n^+ e^{i\varsigma_n L} + D_n^- e^{-i\varsigma_n L}), & -h \leq y \leq -b, \\ -\sum_{n=0}^{\infty} B_n^+ \varkappa_n Y_{2n}(y), & -b \leq y < -a, \\ 1 - \sum_{n=0}^{\infty} A_n^+ \vartheta_n Y_{1n}(y), & -a \leq y < a, \\ -\sum_{n=0}^{\infty} C_n^+ \varkappa_n Y_{3n}(y), & a \leq y < b, \\ \frac{1}{\chi} \sum_{n=0}^{\infty} Y_{4n}(y) (D_n^+ e^{i\varsigma_n L} + D_n^- e^{-i\varsigma_n L}), & b \leq y \leq h. \end{cases} \quad (6.35) \end{aligned}$$

Multiplying (6.35) by $Y_{4m}(y)$, integrating over $[-h, h]$, and using the orthogonality relation (6.26), we get

$$\begin{aligned} -D_m^+ e^{i\varsigma_m L} + D_m^- e^{-i\varsigma_m L} &= \frac{1}{\varsigma_m G_m} \left\{ R_{0m} - \sum_{n=0}^{\infty} A_n^+ \vartheta_n R_{nm} - \sum_{n=0}^{\infty} B_n^+ \varkappa_n P_{nm} \right. \\ &\quad \left. - \sum_{n=0}^{\infty} C_n^+ \varkappa_n Q_{nm} + \frac{2}{\chi} \sum_{n=0}^{\infty} S_{nm} (D_n^+ e^{i\varsigma_n L} + D_n^- e^{-i\varsigma_n L}) \right\}, \quad (6.36) \end{aligned}$$

where

$$S_{nm} = \frac{(S_{nm}^+ + S_{nm}^-)}{2},$$

with

$$S_{nm}^+ = \int_b^h Y_{4n}(y) Y_{4m}(y) dy \quad \text{and} \quad S_{nm}^- = \int_{-h}^{-b} Y_{4n}(y) Y_{4m}(y) dy.$$

6.2.2 Matching Conditions at $x = L$

The continuity conditions of the fluid pressure at $x = L$ are

$$\psi_4(L, y) = \begin{cases} \psi_2^-(L, y), & -b \leq y \leq -a, \\ \psi_1^-(L, y), & -a \leq y \leq a, \\ \psi_3^-(L, y), & a \leq y \leq b. \end{cases} \quad (6.37)$$

Using equations (6.17) and (6.24) into continuity condition for $[-b, -a]$ in (6.37), we get

$$\sum_{n=0}^{\infty} B_n^- Y_{2n}(y) = \sum_{n=0}^{\infty} Y_{4n}(y) (D_n^+ e^{-i\zeta_n L} + D_n^- e^{i\zeta_n L}). \quad (6.38)$$

Multiplying equation (6.38) by $Y_{2m}(y)$, integrating over $[-b, -a]$ and using the orthogonality relation (6.19) successively, it is found that

$$B_m^- = \frac{\alpha}{E_m} \sum_{n=0}^{\infty} P_{mn} (D_n^+ e^{-i\zeta_n L} + D_n^- e^{i\zeta_n L}) + \frac{e_3}{E_m} Y'_{2m}(-b), \quad (6.39)$$

where

$$e_3 = \sum_{n=0}^{\infty} B_n^- Y'_{2n}(-b).$$

Thanks to (6.17) and the edge conditions (6.10c), we have

$$e_3 = \psi_{2y}^-(L, -b) = 0.$$

Similarly, using equations (6.14) and (6.24) into the continuity condition over $[-a, a]$ in (6.37), we obtain

$$\sum_{n=0}^{\infty} A_n^- Y_{1n}(y) = \sum_{n=0}^{\infty} Y_{4n}(y) (D_n^+ e^{-i\zeta_n L} + D_n^- e^{i\zeta_n L}). \quad (6.40)$$

Multiplying (6.40) by $Y_{1m}(y)$, integrating over $[-a, a]$ and then using the orthogonality relation (6.15), we get

$$A_m^- = \frac{1}{a\epsilon_m} \sum_{n=0}^{\infty} R_{mn} (D_n^+ e^{-i\zeta_n L} + D_n^- e^{i\zeta_n L}). \quad (6.41)$$

Finally, using equations (6.23) and (6.24) into the continuity condition over $[a, b]$ in (6.37), we get

$$\sum_{n=0}^{\infty} C_n^- Y_{3n}(y) = \sum_{n=0}^{\infty} Y_{4n}(y) (D_n^+ e^{-i\varsigma_n L} + D_n^- e^{i\varsigma_n L}). \quad (6.42)$$

Multiplying (6.42) by $Y_{3m}(y)$, integrating over $[a, b]$, and on using the orthogonality relation (6.22), we get

$$C_m^- = \frac{\alpha}{E_m} \sum_{n=0}^{\infty} Q_{mn} (D_n^+ e^{-i\varsigma_n L} + D_n^- e^{i\varsigma_n L}) + \frac{e_4}{E_m} Y_{3m}'(b), \quad (6.43)$$

where $e_4 := \sum_{n=0}^{\infty} C_n^- Y_{3n}'(b)$.

Differentiating (6.23) term-by-term and using the edge condition (6.10d), we get

$$e_4 = \psi_{3y}^-(L, b) = 0.$$

On the other hand, the matching conditions for the normal velocity at $x = L$ are

$$\psi_{4x}(L, y) = \begin{cases} \frac{1}{i\chi} \psi_4(L, y), & -h \leq y \leq -b, \\ \psi_{2x}^-(L, y), & -b \leq y \leq -a, \\ \psi_{1x}^-(L, y), & -a \leq y \leq a, \\ \psi_{3x}^-(L, y), & a \leq y \leq b, \\ \frac{1}{i\chi} \psi_4(L, y), & b \leq y \leq h. \end{cases} \quad (6.44)$$

Therefore, using (6.14), (6.17), (6.23), and (6.24) into (6.44), we obtain

$$\begin{aligned} & - \sum_{n=0}^{\infty} \varsigma_n Y_{4n}(y) (D_n^+ e^{-i\varsigma_n L} - D_n^- e^{i\varsigma_n L}) \\ & = \begin{cases} -\frac{1}{\chi} \sum_{n=0}^{\infty} Y_{4n}(y) (D_n^+ e^{-i\varsigma_n L} + D_n^- e^{i\varsigma_n L}), & -h \leq y \leq -b, \\ \sum_{n=0}^{\infty} B_n^- \varkappa_n Y_{2n}(y), & -b \leq y < -a, \\ \sum_{n=0}^{\infty} A^- \vartheta_n Y_{1n}(y), & -a \leq y < a, \\ \sum_{n=0}^{\infty} C^- \varkappa_n Y_{3n}(y), & a \leq y < b, \\ -\frac{1}{\chi} \sum_{n=0}^{\infty} Y_{4n}(y) (D_n^+ e^{-i\varsigma_n L} + D_n^- e^{i\varsigma_n L}), & b \leq y \leq h. \end{cases} \quad (6.45) \end{aligned}$$

Multiplying (6.45) by $Y_{4m}(y)$, integrating from $[-h, h]$, and using the orthogonality relation (6.26), we arrive at

$$\begin{aligned}
 -D_m^+ e^{-i\varsigma_m L} + D_m^- e^{i\varsigma_m L} = & \frac{1}{\varsigma_m G_m} \left\{ \sum_{n=0}^{\infty} A_n^- \vartheta_n R_{nm} + \sum_{n=0}^{\infty} B_n^- \varkappa_n P_{nm} \right. \\
 & \left. + \sum_{n=0}^{\infty} C_n^- \varkappa_n Q_{nm} - \frac{2}{\chi} \sum_{n=0}^{\infty} S_{nm} (D_n^+ e^{-i\varsigma_n L} - D_n^- e^{i\varsigma_n L}) \right\}. \quad (6.46)
 \end{aligned}$$

Therefore, solving (6.36) and (6.46) simultaneously, leads to

$$\begin{aligned}
 D_m^\pm = & \frac{\mp 1}{4\varsigma_m G_m \cos(\varsigma_m L)} \left\{ R_{0m} + \sum_{n=0}^{\infty} (A_n^- - A_n^+) \vartheta_n R_{nm} + \sum_{n=0}^{\infty} (B_n^- - B_n^+) \varkappa_n P_{nm} \right. \\
 & \left. + \sum_{n=0}^{\infty} (C_n^- - C_n^+) \varkappa_n Q_{nm} - \frac{4}{i\chi} \sum_{n=0}^{\infty} S_{nm} (D_n^+ - D_n^-) \sin(\varsigma_n L) \right\} \\
 & - \frac{1}{4i\varsigma_m G_m \sin(\varsigma_m L)} \left\{ R_{0m} - \sum_{n=0}^{\infty} (A_n^- + A_n^+) \vartheta_n R_{nm} - \sum_{n=0}^{\infty} (B_n^- + B_n^+) \varkappa_n P_{nm} \right. \\
 & \left. - \sum_{n=0}^{\infty} (C_n^- + C_n^+) \varkappa_n Q_{nm} + \frac{4}{\chi} \sum_{n=0}^{\infty} S_{nm} (D_n^+ + D_n^-) \cos(\varsigma_n L) \right\}. \quad (6.47)
 \end{aligned}$$

Therefore, Eq. (6.47) leads to another system of infinite equations in unknown modal coefficients.

Hence, the quantities $A_m^\pm, B_m^\pm, C_m^\pm$ and D_m^\pm are found by solving Eqs. (6.29), (6.31), (6.33), (6.39), (6.41), and (6.43) simultaneously.

These equations combine to form an infinite linear system that can be truncated at a finite number of terms and numerically solved for the unknown modal coefficients.

6.2.3 Energy Balance

The energy flux/power inside the duct regions for fluid and for membrane \mathcal{R}_j^\pm , for $j = 1, 2, 3, 4$, are given by

$$\left. \frac{\partial \mathcal{E}}{\partial t} \right|_{fluid} = \Re \left\{ i \int_{\Omega} \psi \left(\frac{\partial \psi}{\partial x} \right)^* dy \right\}, \quad (6.48)$$

and

$$\left. \frac{\partial \mathcal{E}}{\partial t} \right|_{\text{membrane}} = \Re \left\{ \frac{i}{\alpha} \left(\frac{\partial \psi}{\partial y} \right) \left(\frac{\partial^2 \psi}{\partial x \partial y} \right)^* \right\}, \quad (6.49)$$

where superposed asterisk (*) denotes the complex conjugate, \mathcal{E} represents the energy and Ω is the domain of regions \mathcal{R}_1^\pm .

By definition, the incident power is found to be $\mathcal{P}_{\text{inc}} = 2a$. We refer the interested readers to [58, 67] for more details. Similarly, the power/energy flux components in duct sections \mathcal{R}_j^\pm , for $j = 1, 2, 3$ are

$$\begin{aligned} \mathcal{P}_1^\pm &= \frac{1}{2} \Re \left\{ \sum_{n=0}^{\infty} |A_n^\pm|^2 \vartheta_n \epsilon_n \right\}, \\ \mathcal{P}_2^\pm &= \frac{1}{2\alpha a} \Re \left\{ \sum_{n=0}^{\infty} |B_n^\pm|^2 \varkappa_n E_n \right\}, \\ \mathcal{P}_3^\pm &= \frac{1}{2\alpha a} \Re \left\{ \sum_{n=0}^{\infty} |C_n^\pm|^2 \varkappa_n E_n \right\}. \end{aligned}$$

It's important to note that the power fed into the system equals the sum of the scattering powers in different duct regions, i.e.,

$$\mathcal{P}_{\text{inc}} = \mathcal{P}_{\text{abs}} + \sum_{\dagger \in \{+, -\}} \sum_{j=1}^3 \mathcal{P}_j^\dagger. \quad (6.50)$$

It is called the conserved power identity. We can scale the incident power at unity for analysis purpose, which is obtained by dividing equation (6.50) by $2a$, i.e.,

$$1 = \mathcal{E}_{\text{abs}} + \sum_{\dagger \in \{+, -\}} \sum_{j=1}^3 \mathcal{E}_j^\dagger, \quad (6.51)$$

where $\mathcal{E}_j^\pm = \mathcal{P}_j^\pm / 2a$, for $j = 1, 2, 3$, denote the power/energy flux components in duct regions \mathcal{R}_j^\pm . The incident power is scaled at unity in this case. Thus from equation (6.51), the absorbed power \mathcal{E}_{abs} becomes;

$$\mathcal{E}_{\text{abs}} = 1 - \sum_{\dagger \in \{+, -\}} \sum_{j=1}^3 \mathcal{E}_j^\dagger. \quad (6.52)$$

6.3 Numerical Investigation and Discussion

The infinite system of linear algebraic equations (6.29), (6.31), (6.33), (6.41), (6.43), (6.39), and (6.47) is truncated by fixing a truncation parameter $N \in \mathbb{N}$ and setting $m = n = 0, 1, 2, \dots, N$. The truncated system consisting of $8(N + 1)$ equations in $8(N + 1)$ unknown is solved numerically. Throughout this section, we consider the speed of sound in air $c = 343 \text{ms}^{-1}$, density of air $\rho = 1.2043 \text{kgm}^{-3}$, the density of the membranes $\rho_m = 0.1715 \text{kgm}^{-3}$, and $T = 350 \text{Nm}$ be the tension of the membranes.

The parametric values of absorbing lining depend upon the specific impedance $\chi = \xi + i\eta$ of the material in which ξ and η are resistive and reactive components of specific impedance χ . The values of acoustic resistance and acoustic reactance are assumed $\xi = 0.5$ and $-1.0 < \eta < 3.0$ for fibrous sheet and $0 < \xi < 3.0$ and $-1.0 < \eta < 3.0$ for perforated sheet [9].

6.3.1 Validation of the Mode-matching Scheme

The correctness of the truncated solution is affirmed by reconstructing the matching conditions.

It is necessary to confirm that all the matching conditions have been satisfied. Higher accuracy is achieved by increasing the truncation parameter N .

We delineate the real and imaginary components of the dimensionless pressures and normal velocities at the interfaces to substantiate the validity of the solution scheme.

In Figures 6.2-6.3, the real and imaginary parts of dimensionless pressures and normal velocities are sketched at interfaces $x = \pm L$ to validate the truncated solution. It can be observed in Figures 6.2-6.3 that the real and imaginary components of the pressure $\psi_j^+(-L, y)$, for $j = 1, 2, 3$, match exactly to the real and imaginary parts of $\psi_4(-L, y)$. Similarly, real and imaginary parts of pressures $\psi_j^-(L, y)$, for $j = 1, 2, 3$, match exactly to those of $\psi_4(L, y)$.

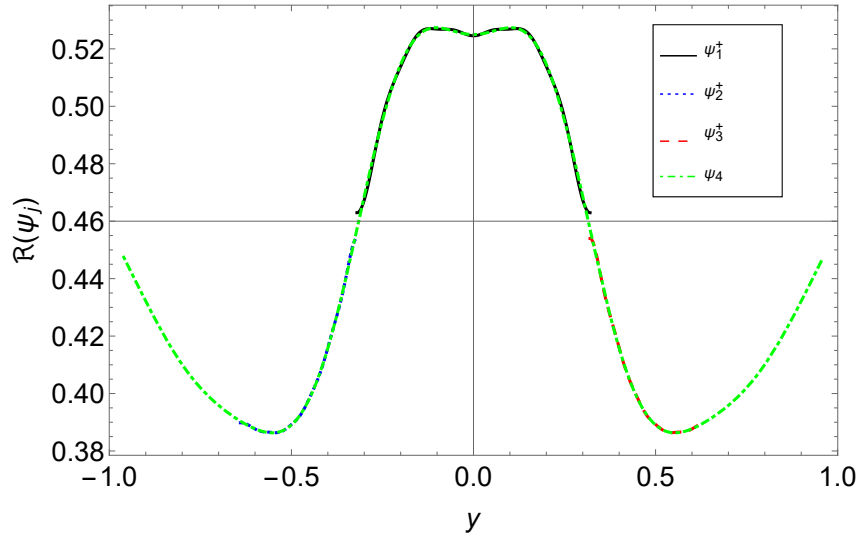
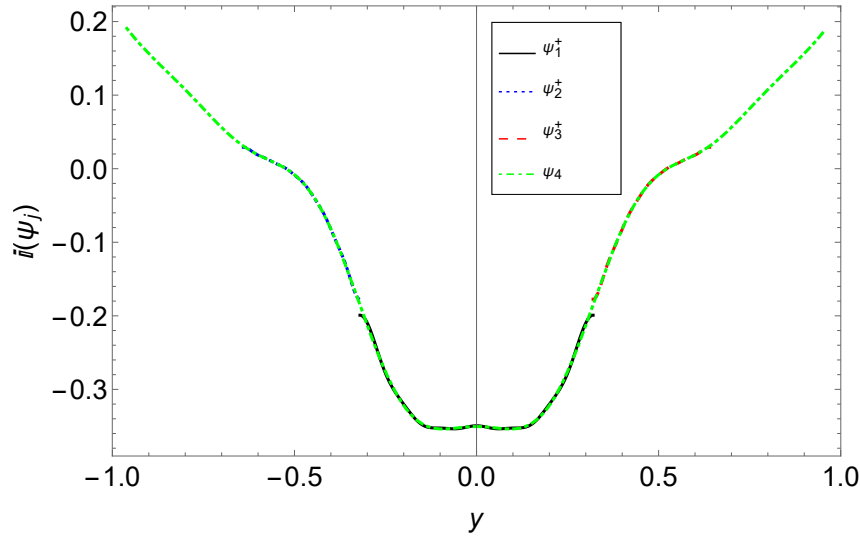

 (a) Real part at $x = -L$

 (b) Imaginary part at $x = -L$

 FIGURE 6.2: The real and imaginary components of the pressure at $x = -L$ when $\bar{a} = 0.05m$, $\bar{b} = 0.1m$, $\chi = 0.5 + 0.5i$, $\bar{h} = 0.15m$, and $f = 350Hz$.

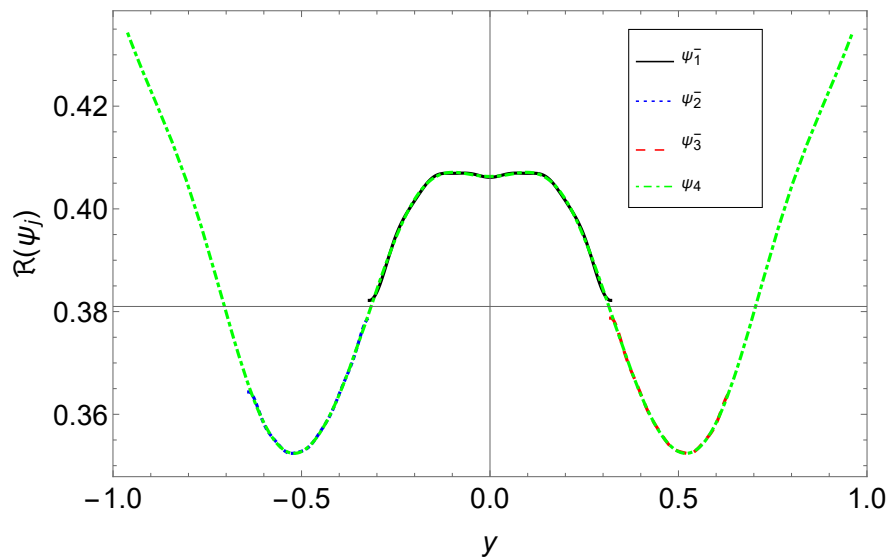
Figures 6.4-6.5 substantiates that the real and imaginary parts of normal velocity $\psi_{4x}(-L, y)$ coincides with $\psi_{jx}^{\dagger}(-L, y)$, for $j = 1, 2, 3$, over $-h < y < h$ and with $(-1/i\chi)\psi_4(-L, y)$ over $-h < y < -b$ and $b < y < h$.

Further, the real and imaginary parts of normal velocity $\psi_{4x}(L, y)$ match with $\psi_{jx}^{-}(L, y)$, for $j = 1, 2, 3$, over $-h < y < h$ and with $(1/i\chi)\psi_4(L, y)$ over $-h < y < -b$ and $b < y < h$.

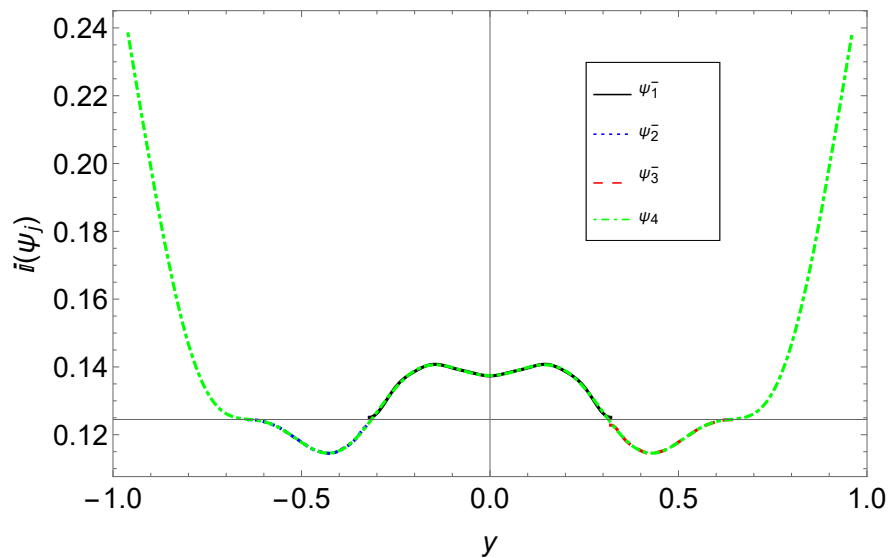
Nevertheless, the real and imaginary parts of normal velocities are not perfectly matched at the edges or corners due to the presence of singularities in the geometrical configuration where the velocity fields are not defined.

Moreover, there are assumption of step-discontinuities in matching conditions.

In a nutshell, all the matching conditions of the pressures and normal velocities are reasonably satisfied by the truncated numerical solution.

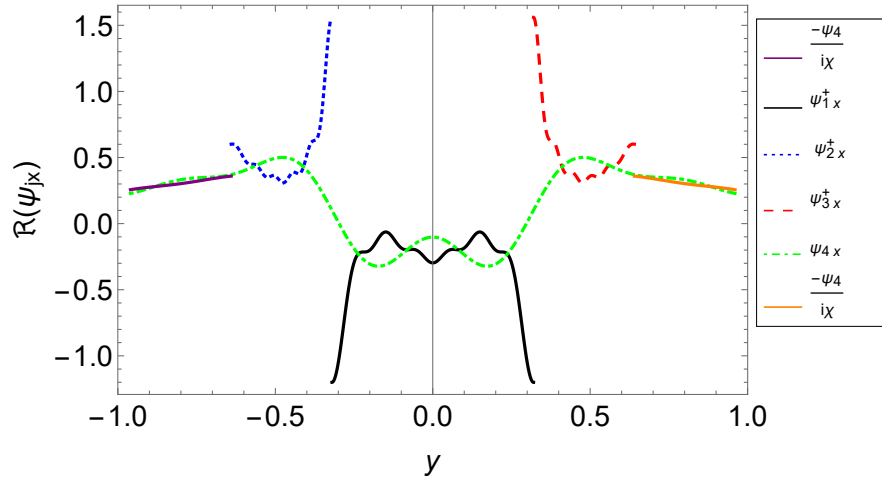


(a) Real part at $x = L$

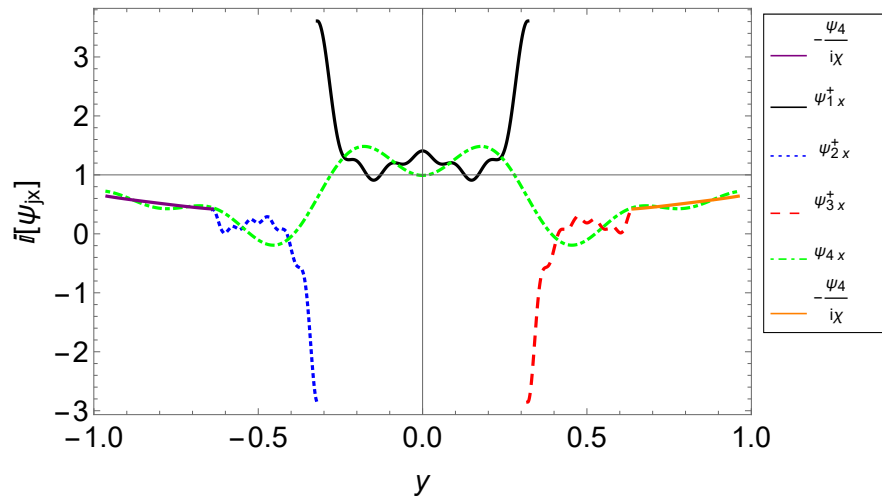


(b) Imaginary part at $x = L$

FIGURE 6.3: The real and imaginary components of the pressure at $x = L$ when $\bar{a} = 0.05m$, $\bar{b} = 0.1m$, $\chi = 0.5 + 0.5i$, $\bar{h} = 0.15m$, and $f = 350Hz$.



(a) Real part at $x = -L$



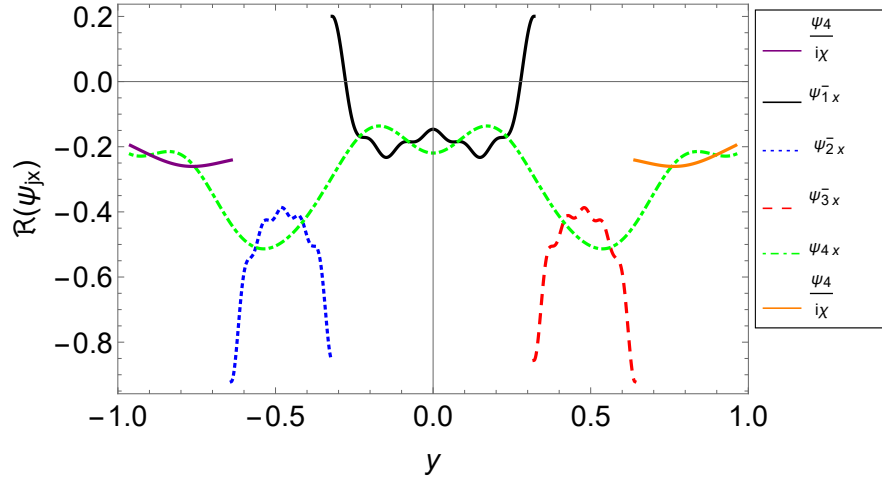
(b) Imaginary part at $x = -L$

FIGURE 6.4: The real and imaginary components of the normal velocity at $x = -L$ when $\bar{a} = 0.05m$, $\bar{b} = 0.1m$, $\chi = 0.5 + 0.5i$, $\bar{h} = 0.15m$, and $f = 350Hz$.

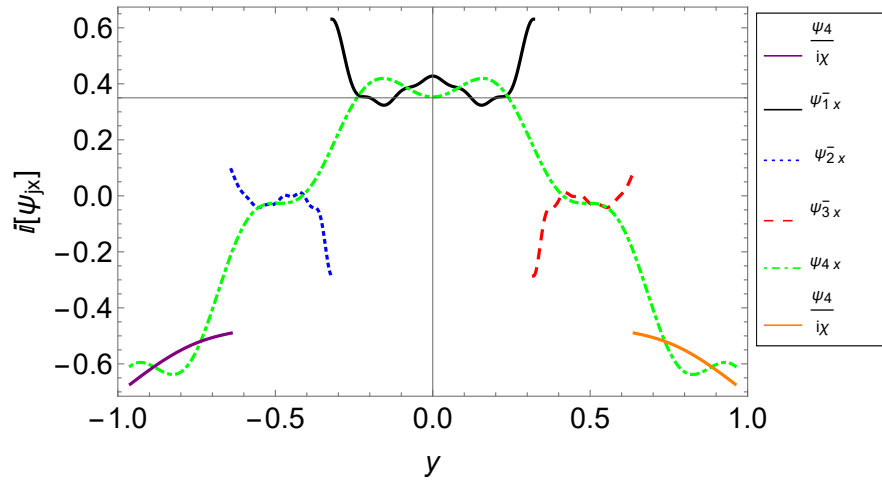
6.3.2 Analysis of Reflected and Absorbed Powers

In this section, we discuss the influence of absorbing linings across the walls of the expansion chamber, \mathcal{R}_4 , on the reflected and absorbed powers in different frequency bandwidths with structural continuity or discontinuity.

We separately discuss the influence of resistance ξ and the reactance η on the power.



(a) Real part at $x = L$



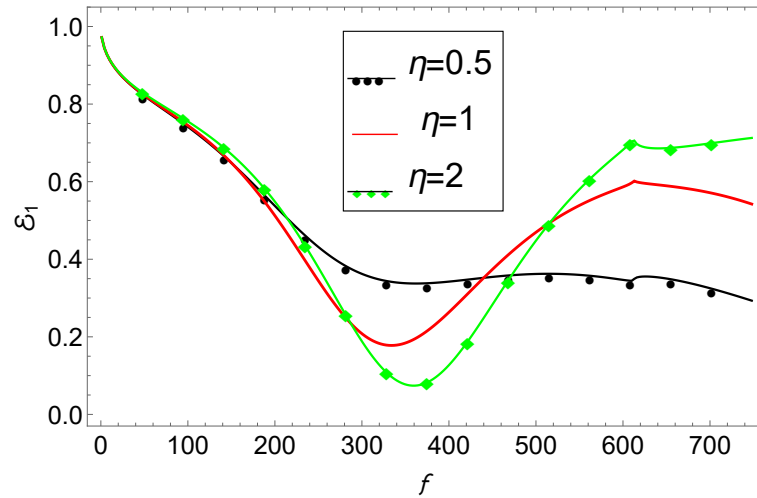
(b) Imaginary part at $x = L$

FIGURE 6.5: The real and imaginary components of the normal velocity at $x = L$ when $\bar{a} = 0.05m$, $\bar{b} = 0.1m$, $\chi = 0.5 + 0.5i$, $\bar{h} = 0.15m$, and $f = 350Hz$.

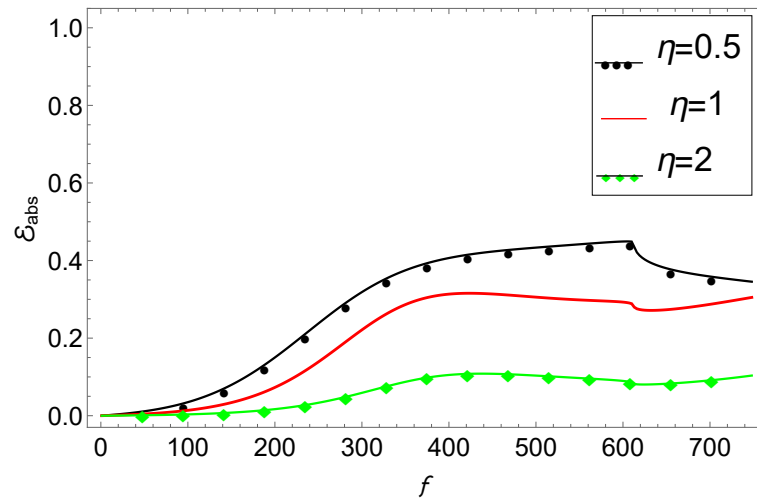
6.3.2.1 Influence of Reactance on Power

The reflected power (\mathcal{E}_1) and absorbed power (\mathcal{E}_{abs}) are plotted in Figures 6.6-6.7 over the frequency bandwidth $1Hz \leq f \leq 750Hz$ for different values of reactance η .

Figures 6.6(a)-6.6(b) correspond to an the central region that includes cavities (i.e., $\bar{h} > \bar{b}$) whereas Figures 6.7(a)-6.7(b) correspond to an central region without cavities (i.e., $\bar{h} = \bar{b}$). .



(a) Reflected energy, $\bar{h} = 0.15m$



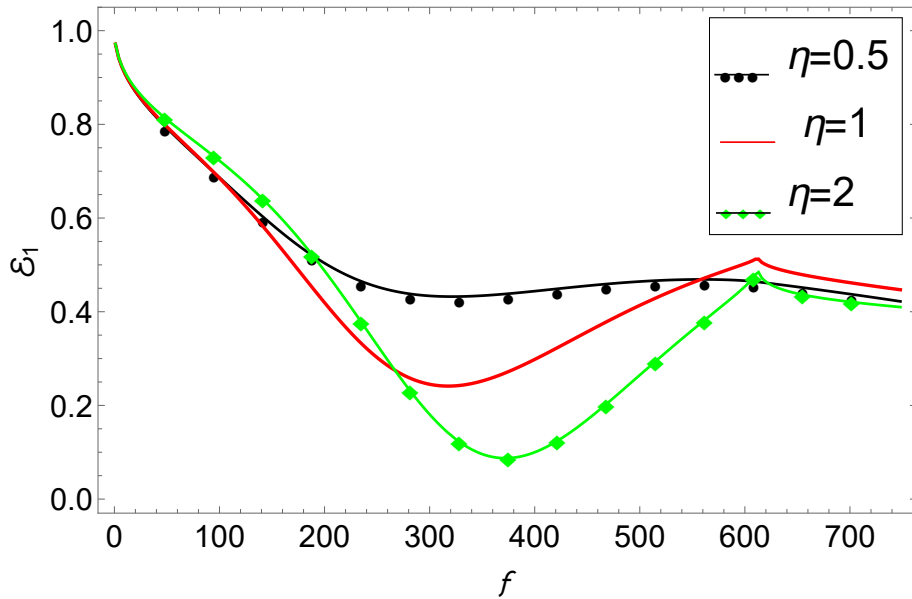
(b) Absorbed energy, $\bar{h} = 0.15m$

FIGURE 6.6: Energy versus frequency with fibrous lining along the walls of the expansion chamber when $\bar{a} = 0.05m$, $\bar{b} = 0.1m$, and $N = 10$.

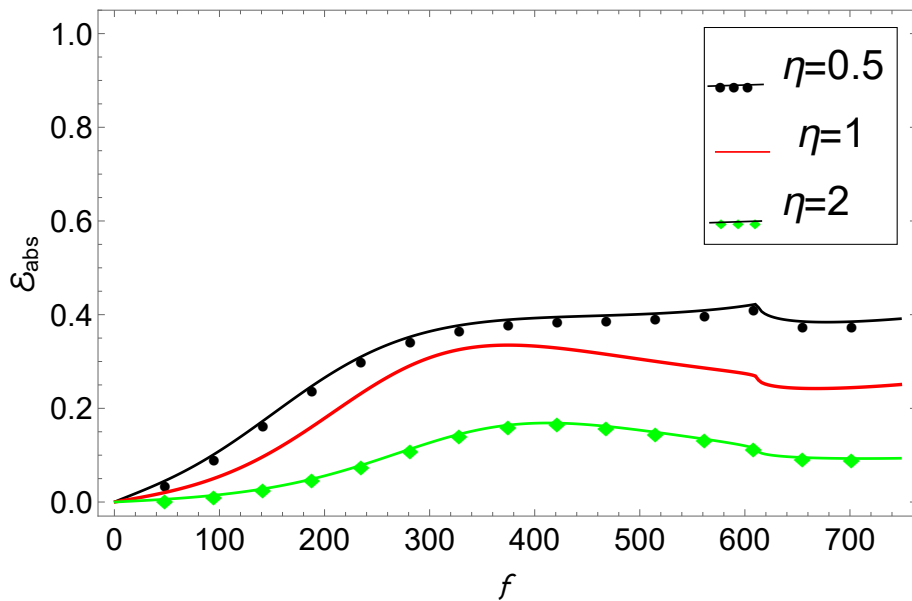
It can be remarked from Figures 6.6(a) and 6.7(a) that the magnitude of reflected power \mathcal{E}_1 falls off from $0Hz$ to $334Hz$ and then varies up to the cut-off frequency $613Hz$.

Beyond this frequency, the magnitude increases again, but not as much as it did in the low-frequency ranges.

The minima in Figures 6.6(a) and 6.7(a) correspond to the cut-off (on) frequencies of various high wave-modes that can propagate in the duct.



(a) Reflected energy, $\bar{h} = 0.1m$



(b) Absorbed energy, $\bar{h} = 0.1m$

FIGURE 6.7: Energy versus frequency with fibrous lining along the walls of the expansion chamber when $\bar{a} = 0.05m$, $\bar{b} = 0.1m$, and $N = 10$.

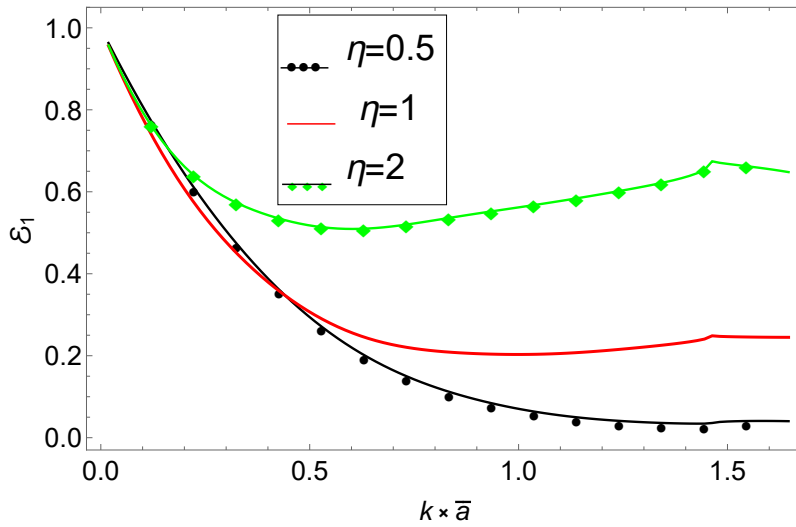
The notion is based on the behavioral changes of the eigenvalues from complex to real and vice versa.

The reflected energy decays monotonically with increasing values of η in the frequency band $1Hz < f < 613Hz$ and then varies inversely for $f > 613Hz$.

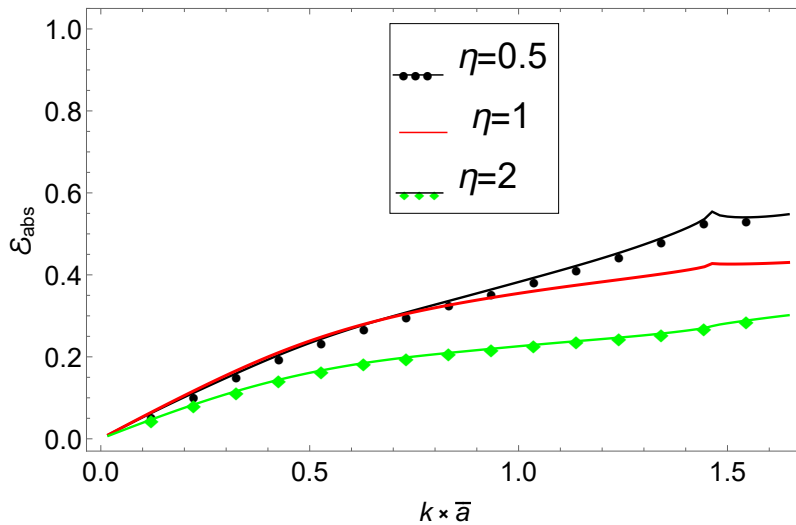
This is the point where the secondary mode of \mathcal{R}_j^\pm , for $j = 2, 3$, becomes cut-on.

Variation of the reflected power in the band $1Hz < f < 613Hz$ provides evidence of the variation of the real and imaginary parts of eigenvalues of the expansion chamber.

Figures 6.6(b) and 6.7(b) indicate that as the value of η increases, the level of the absorbed energy drops. If we enhance the frequency up to the level of $613Hz$, the absorbed energy steadily rises.

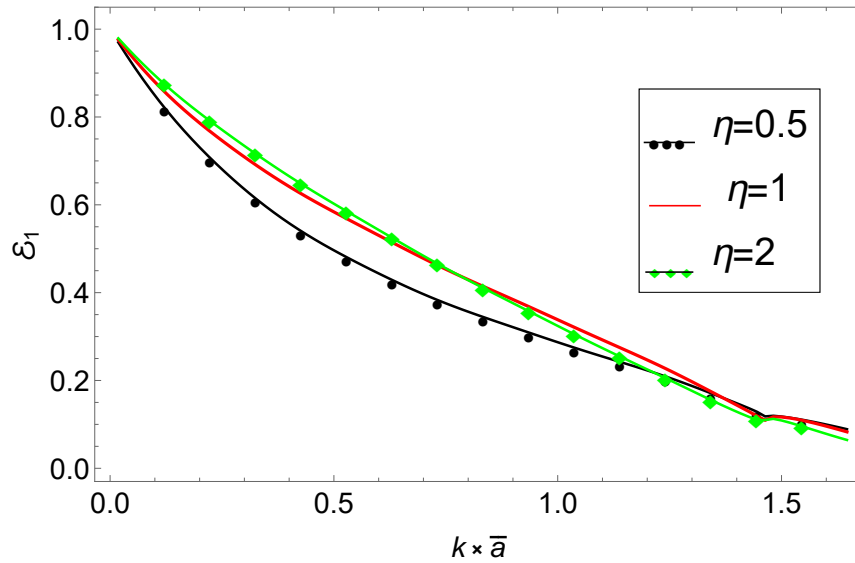


(a) Reflected energy, $\bar{h} = 0.15m$

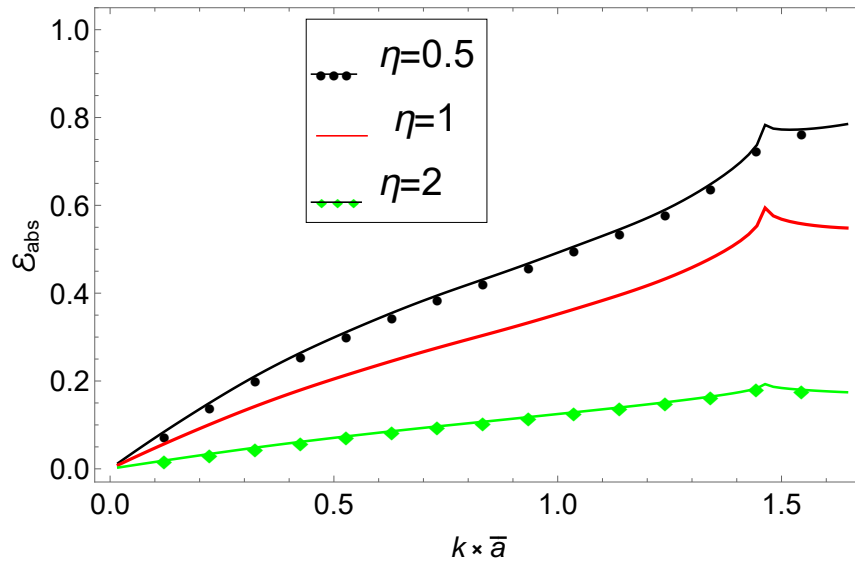


(b) Absorbed energy, $\bar{h} = 0.15m$

FIGURE 6.8: Energy versus duct height ($k \times \bar{a}$) with fibrous lining along the walls of the expansion chamber when $f = 1000Hz$, $\bar{b} = 0.1m$, and $N = 10$.



(a) Reflected energy, $\bar{h} = 0.1m$



(b) Absorbed energy, $\bar{h} = 0.1m$

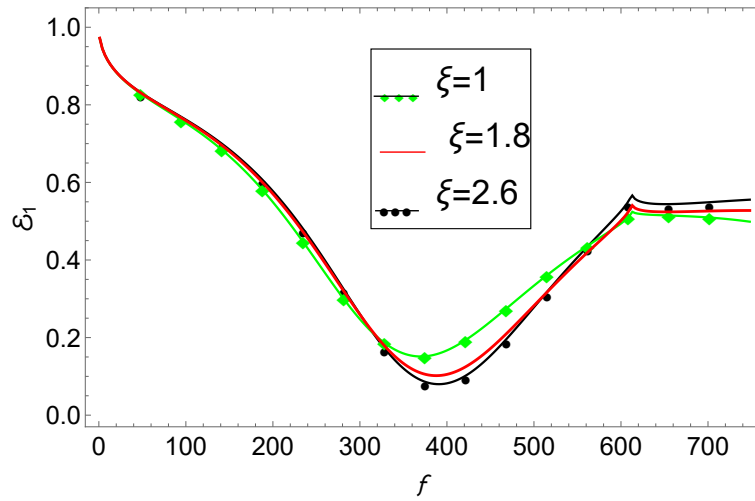
FIGURE 6.9: Energy versus duct height ($k \times \bar{a}$) with fibrous lining along the walls of the expansion chamber when $f = 1000Hz$, $\bar{b} = 0.1m$, and $N = 10$.

There is a tilt in the behavior, the energy level drops a little down and then gets straight.

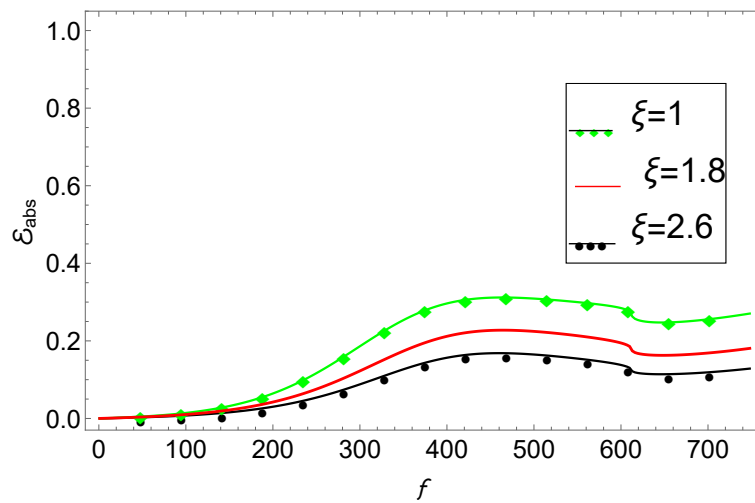
The sound level fads out gradually as the absorbed energy goes up.

It is seen from Figures 6.6(b) and 6.7(b) that absorbed energy increases for small values of η and becomes smooth after the first cut-on.

Note that more absorbed energy results in more sound attenuation in the transmitted region.



(a) Reflected energy, $\bar{h} = 0.15m$



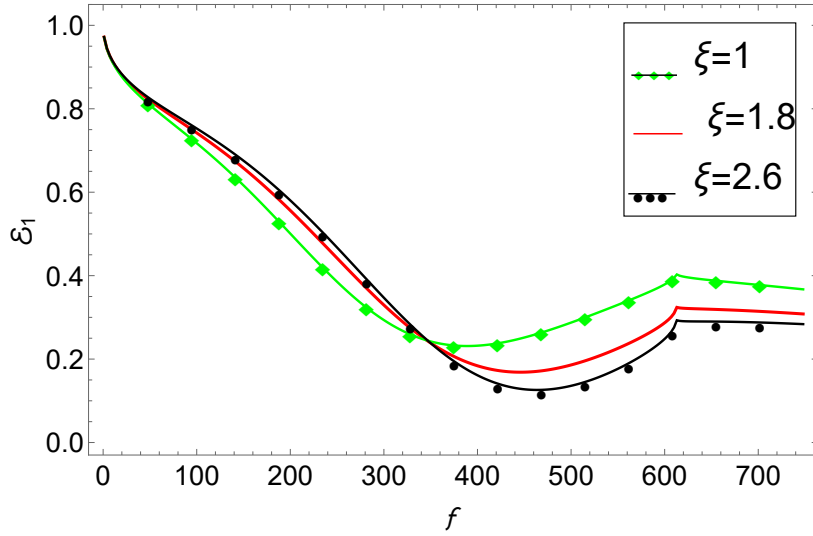
(b) Absorbed energy, $\bar{h} = 0.15m$

FIGURE 6.10: Energy versus frequency with perforated lining along the walls of the expansion chamber when $\bar{a} = 0.05m$, $\bar{b} = 0.1m$, and $N = 10$.

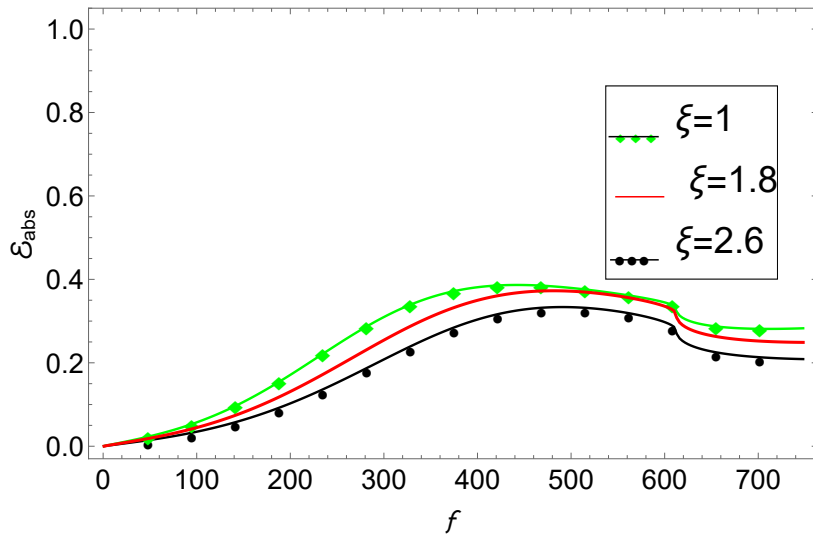
The cut-on frequency of the first propagating mode is $613Hz$. Thus, the presence of an absorbent material causes the fundamental mode to be non-planar.

As can be remarked from Figures 6.6(a) and 6.7(a), the reflected energy reduces significantly with an increase in the acoustic reactance η (especially, for $\eta = 2$). Hence, the rate of attenuation depends on the value of the specific impedance.

The lining also seems to quickly smooth out the lobe pattern of the reflection after $f = 400Hz$ approximately.



(a) Reflected energy, $\bar{h} = 0.1m$



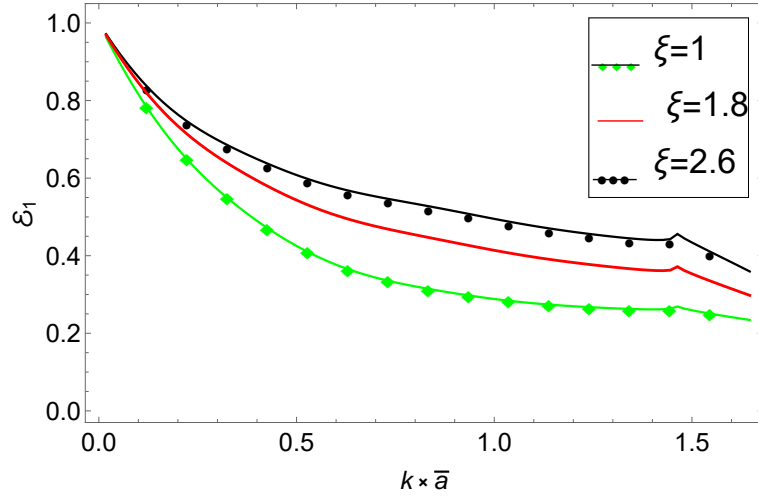
(b) Absorbed energy, $\bar{h} = 0.1m$

FIGURE 6.11: Energy versus frequency with perforated lining along the walls of the expansion chamber when $\bar{a} = 0.05m$, $\bar{b} = 0.1m$, and $N = 10$.

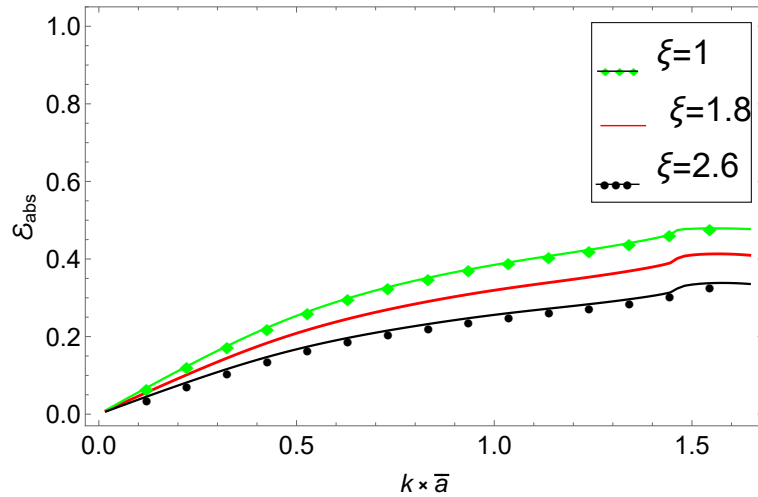
Figures 6.8 and 6.9 establish the relationship between the energy distribution and the structural-discontinuity of the expansion chamber (i.e., when $\bar{h} > \bar{b}$ or $\bar{h} = \bar{b}$).

Specifically, the reflected and absorbed energies are plotted versus the duct height ($k \times \bar{a}$) at a fixed frequency $f = 1000Hz$ for different values of η .

It can be found from Figure 6.8(a) that the reflected power increases by increasing the height of the duct. For a waveguide with cavities in the expansion chamber, a steady increase in the duct height between the infinite plates gives a decreasing value of the reflected power. On the other hand, the membranes reflect a significant portion of the power for small duct heights, but this quickly drops to zero as the height increases. Moreover, the reflected energy increases by increasing η .



(a) Reflected energy, $\bar{h} = 0.15m$

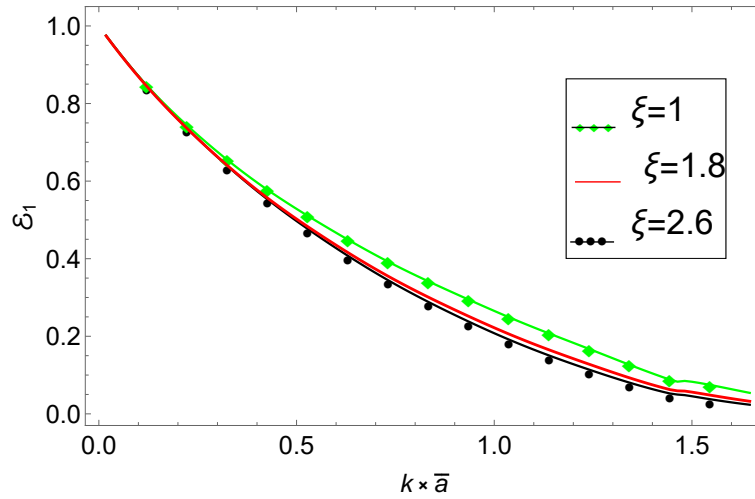


(b) Absorbed energy, $\bar{h} = 0.15m$

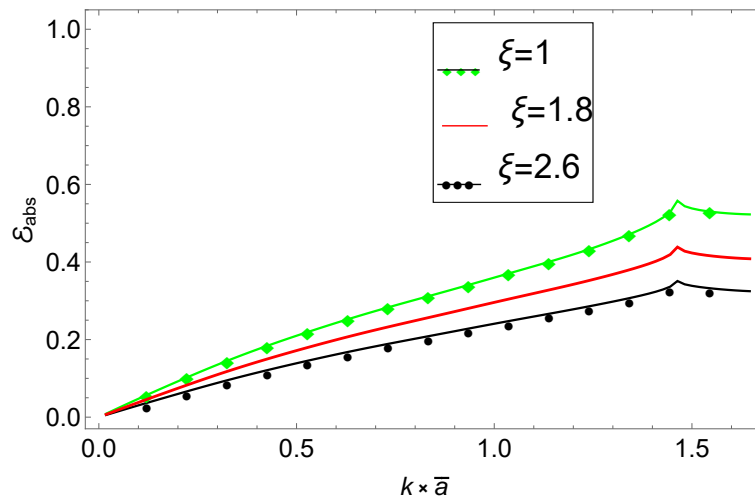
FIGURE 6.12: Energy versus duct height ($k \times \bar{a}$) with perforated lining along the walls of the expansion chamber when $f = 1000Hz$, $\bar{b} = 0.1m$, and $N = 10$.

In Figures 6.8(b) and 6.9(b), the absorbed power (\mathcal{E}_{abs}) is plotted versus the height of the duct ($k \times \bar{a}$) for different values of η . It is observed that the absorbed

power increases as the channel waveguide width increases, however, an opposite behavior is observed after the first cut-on (with $k \times \bar{a} > 1.5m$). It is noted that a slightly less amount of energy is absorbed due to the cavities as compared to the waveguides without cavities. The energy absorption increases more rapidly if the height of the inner duct is increased. It can be observed that more energy is absorbed for smaller values of η ; see, for example, Figures 6.8(b) and 6.9(b).



(a) Reflected energy, $\bar{h} = 0.1m$



(b) Absorbed energy, $\bar{h} = 0.1m$

FIGURE 6.13: Energy versus duct height ($k \times \bar{a}$) with perforated lining along the walls of the expansion chamber when $f = 1000Hz$, $\bar{b} = 0.1m$, and $N = 10$.

For small duct height ($k \times \bar{a} < 0.8m$), the behavior of the absorbed power remains unchanged for discontinuous waveguides.

6.3.2.2 Influence of Resistance on Power

The reflected and absorbed energies are plotted in Figures 6.10 – 6.11 against frequency over the bandwidth $1Hz \leq f \leq 750Hz$ when the central region \mathcal{R}_4 has a perforated lining with reactance $\eta = 1$ and resistance $\xi = 1, 1.8, \text{ or } 2.6$.

It is noticed in Figures 6.10(a) and 6.11(a) that the reflected energy (\mathcal{E}_1) of the first propagating mode diminishes in the frequency band $1Hz < f < 360Hz$ and then rises up to $f = 613Hz$, after which it becomes smooth. This behavior of reflected energy is admitted due to the variation of the real and imaginary parts of the eigenvalues corresponding to the expansion chamber.

It is also observed that a less amount of energy is reflected when the value of the acoustic resistance ascends in regime $360Hz < f < 613Hz$. Outside this bandwidth, the behavior reversed in the absence of step-discontinuities. The performance of the absorbed power against frequency is delineated in Figures 6.10(b) and 6.11(b) for different choices of ξ .

The absorbed energy gradually increases with increasing frequency till the cut-on mode frequency $f = 613Hz$ and then becomes smooth. This is the point where the membrane-bounded duct starts propagating and is known as the cut-on point for the secondary mode. However, a decrease in the absorption is recorded with an increasing resistance (see, e.g., Figure 6.10(b)).

The behavior of the reflected energy versus non-dimensional height of the inner duct (i.e., $k \times \bar{a}$) is elaborated through Figures 6.12 – 6.13 for different choices of the resistance ξ .

A strictly monotone decrease in the reflected energy is observed in Figure 6.13(a) for an increase in the duct spacing ($k \times \bar{a}$). The pattern of curves is due to the behavioral changes in the eigenvalues. The cut-on modes are responsible for the attenuation of the transmitted sound.

In Figures 6.12(b) and 6.13(b), the absorbed power (\mathcal{E}_{abs}) is plotted against height of the duct for different values of the resistance ξ .

It is remarked that the absorbed power increases whereas reflection decrease when the height of the duct ($k \times \bar{a}$) is increased.

However, a smooth behavior of the absorbed energies is observed after the first cut-on when the step-discontinuities are present. Moreover, the curve is quite smooth, and very few cut-on modes appear in the case of the perforated lining.

In a nutshell, the fibrous case absorbs more energy than the perforated one, and a discontinuous setting absorbs more energy than a continuous setting. The presence of extra propagating modes in regions with discontinuities is responsible for the later impact.

Power is transmitted into those regions, thereby enhancing the reflection. This device setting is suitable, when more internal reflection is required. In contrast, the planar central region (without discontinuity) yields less internal reflection than a discontinuous expansion chamber.

Chapter 7

Conclusions and Future Recommendations

This chapter summarizes the findings of this dissertation and provides suggestions for further research in the field.

7.1 Conclusions

In this dissertation, an analysis of wave scattering in bifurcated and trifurcated waveguides with material contrast and multiple step-discontinuities was performed. We designed and debated the performance of the waveguide structures for controlling active noise transmission. The chapter-wise summary of the dissertation is provided hereinafter. Chapter 1 depicts the state of the art relevant to the subject matter along with the avant-garde.

The fundamental concepts that are necessary to understand and analyze the scattering mechanism of the acoustic waves in different waveguide structures, the derivation of the linear acoustic wave equation along different types of boundary conditions for different waveguide models have been discussed in Chapter 2. Also, the standard orthogonality relations have been explored based on physical models in the category of the SL system.

In chapter 3, we have discussed the acoustic scattering in a trifurcated waveguide involving structural discontinuity at an interface. The inside of the duct regions contains compressible fluid while the bounding wall conditions are selected to be rigid and/or soft. By varying inside and bounding characteristics of the regions, two physical problems are formulated together. The MM approach has been invoked to solve the envisaged boundary value problems.

The eigenfunctions along with the appropriate orthogonality attributes in their concerning regions enable to reshape differential system into a linear algebraic system that is truncated and solved numerically. The provided solution remains valid for both discontinuous and planar waveguide structures. It also helps us to discuss the radiated energy versus the variation of the geometric discontinuity and the size of the regions.

This problem can be regarded as a prototype problem that provides a benchmark scheme to model and solve a range of bifurcated or trifurcated waveguide problems involving geometric discontinuities and various material properties of medium and bounding walls. It is interesting to notice that the conservation of energy flux across the duct regions not only confirms the propagation of cut-on duct modes in various duct sections but also provides a useful check on the accuracy of the presented algebra.

Besides this, the truncated solution has also been used to reconstruct the matching of pressure and normal velocity modes at the interfaces. The validation of matching conditions at the interfaces along with the conservation of energy flux across the duct regions substantiates the appositeness of the MM solution altogether.

In chapter 4, the wave scattering characteristics of a planar trifurcated lined duct for different bounding properties have been examined. The governing problem was formulated and solved by considering general expressions of mixed boundary conditions.

The eigenfunctions enable a differential system to be recast into a linear algebraic system that may be truncated and solved numerically after utilising the proper orthogonality relations and matching conditions in relevant regions. The idea was

to observe the wave scattering behavior of trifurcated lined duct by varying the bounding properties and size of the duct and observing the field behavior with and without structural discontinuity.

The existing results for a trifurcated lined duct for different bounding properties (soft, rigid, impedance) without structural discontinuity have been recovered from our general solution framework. Moreover, the radiated energy in all duct regions has been computed and discussed through apposite numerical results. It is depicted that the lined ducts produced lesser noise as compared to hard or soft ducts. Further, the conservation of energy flux across the duct regions have been attained successfully, confirming the propagation of cut-on duct modes in various duct sections and providing validation on the accuracy of the presented algebra. Besides, the truncated solution has been validated to reconstruct the matching of pressure and normal velocity modes.

Chapter 5 was dedicated to the study of the radiated and reflected energies in infinite trifurcated waveguides comprising an expansion chamber. Two silencer configurations with discontinuous and planar expansion chambers were considered when the bounding properties of the core region were assumed to be rigid, soft, or impedance type with absorbent linings. The governing problem was formulated and solved by considering general expressions of mixed boundary conditions. It can be observed that energy is absorbed more in the planar case than the discontinuous case and also there is more absorption of energy in a perforated case than that of a fibrous sheet.

It is noted that the reflected energy was considerably reduced in the increasing frequency regime. Further, the curve pattern was observed to be smooth with very few cut-on modes in the case of no fibrous sheet. More cut-on modes are observed for the discontinuous case. However, the cut-on modes are reduced considerably when the step of discontinuities is removed. The conservation of energy flux across the duct regions has been attained successfully, confirming the propagation of cut-on duct modes in various duct sections and providing validation on the accuracy of algebra.

The truncated solution has been validated to reconstruct the matching conditions

of pressure and normal velocity modes. This together justified the use of the MM technique for these problems. Therefore, it is concluded from obtained results that the proposed model can be used as a perfect broadband acoustic energy absorber. The results of this study are an important step forward to understand the mechanism of waveguide acoustic attenuation and the analysis presented in this chapter has many applications in duct acoustics and noise reduction systems. We can take the geometric symmetry in the vertical direction. This increases the cost of algebra but the results are same.

In chapter 6, the wave scattering characteristics of a flexible trifurcated lined duct involving an expansion chamber for different bounding properties have been examined. The governing problem is formulated and solved by considering general expressions of mixed boundary conditions. The reflected and absorbed energies in different duct regions have been computed and apposite numerical results are provided to understand the dependence of the scattering energies on pertinent material and geometric parameters. It is observed that the lined ducts with perforated materials produced lesser noise as compared to the fibrous materials. Further, the conservation of energy flux across the duct regions was successfully verified, confirming the propagation of cut-on duct modes in various duct sections and providing validation of the results.

Furthermore, numerical tests are also conducted to look into the impact of absorbent linings and edge conditions on flexural mode attenuation. The structure-borne or fluid-borne mode exits the guiding structure, with visual representations of the consequences. The use of absorbent linings, on the other hand, is ineffectual for structure-borne mode accidents. This lining, on the other hand, shows a high level of fluid-borne mode incident absorption. In fluid-borne mode accidents, however, edge circumstances have just a minimal impact.

Different silencer design also affects attenuation for both structure-borne and fluid-borne mode occurrences. The majority of acoustic power propagates via structure borne in structure-borne mode excitation, whereas the most of energy propagates via fluid in fluid-borne mode excitation. Only the fluid-borne incidence is affected by the consideration of absorbent lining along the walls.

One may consider the geometric symmetry along vertical direction to broken down the problem into two sub-problems: symmetric sub-problem and anti-symmetric sub-problem, as is done in [69]. These sub-problems can be solved separately and then are combined to get the solution of original problem. These sub-problems are easy to resolve as compared with original problem. However, this practice might increase the algebraic cost but yields same results.

7.2 Future Recommendations

Future work would be to extend in the following manners.

- The problem of obtaining MM solutions and low frequency approximations for a flexible channel surrounded by elastic plates/membranes with an inserted expansion chamber.
- It is also possible to perform an asymptotic analysis to determine optimal dispersive relations and low-frequency attenuation conditions. Thus, introducing material contrast relations that will suit all duct regions would be a reasonable first step in this direction.
- The two-dimensional problems can be expanded to three-dimensional cartesian coordinates (x, y, z) using sound-hard inlet/outlet ducts and an elastic plate connected at the mouth of the expansion chamber to broaden the scope of the investigation. The difficulties can be expanded further by introducing absorption and porosity effects in the finite cavity.
- MM technique was used to solve the problem of a flexible panel bounded by elastic plates with an inserted expansion chamber in the presence of mean flow.
- Finally, inverse wave propagation in a trifurcated waveguide is a possible extension of the difficulties addressed in this dissertation, with the aim of reconstructing initial data or interfacial conditions from the given information at the boundaries.

Bibliography

- [1] A. Cummings, “Sound attenuation in ducts lined on two opposite walls with porous material, with some application to splitters”, *Journal of Sound and Vibration*, vol. 49, no. 1, pp. 9-35, 1976.
- [2] D. A. Bies, C. H. Hansen and G. E. Bridges, “Sound attenuation in rectangular and circular cross-section ducts with flow and bulk-reacting liner”, *Journal of Sound and Vibration*, vol. 146, no. 1, pp. 47-80, 1991.
- [3] S. K. Kakoty and V. K. Roy, “Bulk reaction modeling of ducts with and without mean flow”, *The Journal of the Acoustical Society of America*, vol. 112, no. 1, pp. 75-83, 2002.
- [4] R. J. Astley and A. Cummings, “A finite element scheme for attenuation in ducts lined with porous material: comparison with experiment”, *Journal of Sound and Vibration*, vol. 116, no. 2, pp. 239-263, 1987.
- [5] M. Hassan and A. D. Rawlins, “Radiation from a two dimensional duct”, *Canadian Journal of Physics*, vol. 75, no. 6, pp. 375-384, 1997.
- [6] B. Polat, “Plane wave diffraction by a semi-infinite soft/hard parallel plate waveguide”, *Canadian Journal of Physics*, vol. 76, no. 10, pp. 771-784, 1998.
- [7] I. H. Tayyar, A. Buyukaksoy and A. Isikyeyer, “Wiener-Hopf analysis of the parallel plate waveguide with opposing rectangular dielectric-filled grooves”, *Canadian Journal of Physics*, vol. 86, no. 5, pp. 733-745, 2008.

-
- [8] M. Ayub, M. H. Tiwana and A. B. Mann, “Acoustic diffraction in a trifurcated waveguide with mean flow”, *Communications in Nonlinear Science and Numerical Simulation*, vol. 15, no. 12, pp. 3939-3949, 2010.
- [9] M. Hassan and A. D. Rawlins, “Sound radiation in a planar trifurcated lined duct”, *Wave Motion*, vol. 29, no. 2, pp. 157-174, 1999.
- [10] M. Ayub, M. H. Tiwana and A. B. Mann, “Wiener-Hopf analysis of an acoustic plane wave in a trifurcated waveguide”, *Archive of Applied Mechanics*, vol. 81, no. 6, pp. 701-713, 2010.
- [11] A. Demír and A. Büyükaksoy, “Wiener-Hopf approach for predicting the transmission loss of a circular silencer with a locally reacting lining”, *International Journal of Engineering Science*, vol. 43, no. 5-6, pp. 398-416, 2005.
- [12] J. B. Lawrie, “Comments on a class of orthogonality relations relevant to fluid-structure interaction,” *Meccanica*, vol. 47, no. 3, pp. 783-788, 2012.
- [13] J. B. Lawrie and R. Kirby, “Mode matching without root finding: Application to a dissipative silencer”, *The Journal of the Acoustical Society of America*, vol. 119, no. 4, pp. 2050-2061, 2006.
- [14] R. Kirby, “Modeling sound propagation in acoustic waveguides using a hybrid numerical method”, *The Journal of the Acoustical Society of America*, vol. 124, no. 4, pp. 1930-1940, 2008.
- [15] M. Afzal, R. Nawaz, M. Ayub and A. Wahab, “Acoustic scattering in flexible waveguide involving step discontinuity”, *PLOS ONE*, vol. 9, no. 8, e103807, 2014.
- [16] M. Afzal, R. Nawaz and A. Ullah, “Attenuation of dissipative device involving coupled wave scattering and change in material properties”, *Applied Mathematics and Computation*, vol. 290, pp. 154-163, 2016.
- [17] L. Rayleigh, “The Theory of Sound”, *Dover, New York*, vol. 2, pp. 476, 1945.
- [18] A. Boström, “Transmission and reflection of acoustic waves by an obstacle in a waveguide”, *Wave Motion*, vol. 2, no. 2, pp. 167-184, 1980.

- [19] J. H. Miles, "Acoustic transmission matrix of a variable area duct or nozzle carrying a compressible subsonic flow", *The Journal of the Acoustical Society of America*, vol. 69, no. 6, pp. 1577-1586, 1981.
- [20] R. Nawaz and J. B. Lawrie, "Scattering of a fluid-structure coupled wave at a flanged junction between two flexible waveguides", *The Journal of the Acoustical Society of America*, vol. 134, no. 3, pp. 1939-1949, 2013.
- [21] R. Nawaz, M. Afzal and M. Ayub, "Acoustic propagation in two-dimensional waveguide for membrane bounded ducts", *Communications in Nonlinear Science and Numerical Simulation*, vol. 20, no. 2, pp. 421-433, 2015.
- [22] A. D. Rawlins, "Radiation of sound from an unflanged rigid cylindrical duct with an acoustically absorbing internal surface", *Proceedings of the Royal Society A*, vol. 361, no. 1704, pp. 65-91, 1978.
- [23] A. Demir and A. Buyukaksoy, "Radiation of plane sound waves by a rigid circular cylindrical pipe with a partial internal impedance loading", *Acta Acustica United with Acustica*, vol. 89, no. 4, pp. 578-585, 2003.
- [24] P. M. Morse, "The transmission of sound inside pipes", *The Journal of the Acoustical Society of America*, vol. 11, no. 2, pp. 205-210, 1939.
- [25] D. S. Jones, "Diffraction by three semi-infinite planes", *Proceedings of the Royal Society A*, vol. 404, no. 1827, pp. 299-321, 1986.
- [26] S. Asghar, M. Ayub and B. Ahmad, "Point source diffraction by three half planes in a moving fluid" *Wave Motion*, vol. 15, no. 3, pp. 201-220, 1992.
- [27] I. D. Abrahams, "Scattering of sound by two parallel semi-infinite screens", *Wave Motion*, vol. 9, no. 4, pp. 289-300, 1987.
- [28] B. Polat, "High frequency from a semi-infinite cylindrical resistive pipe", *International Journal of Electronics and Communications (AEU)*, vol. 53, pp. 241-246, 1999.

-
- [29] A. D. Rawlins, "Two waveguide trifurcated problems", *Mathematical Proceedings of the Cambridge Philosophical Society*, vol. 121, no. 3, pp. 555-573, 1997.
- [30] M. Ayub, M. H. Tiwana and A. B. Mann, "Propagation of sound in a duct with mean flow", *Communications in Nonlinear Science and Numerical Simulation*, vol. 14, no. 9-10, pp. 3578-3590, 2009.
- [31] R. Kirby, "The acoustic modelling of dissipative elements in automotive exhausts", PhD Thesis, *University of Hull*, 1996.
- [32] R. Kirby and J. B. Lawrie, "A point collocation approach to modelling large dissipative silencers", *Journal of Sound and Vibration*, vol. 286, no. 1-2, pp. 313-339, 2005.
- [33] A. Selamet, P. M. Radavich, "The effect of length on the acoustic attenuation performance of concentric expansion chambers: an analytical, computational and experimental investigation", *Journal of Sound and Vibration*, vol. 201, no. 4, pp. 407-426, 1997.
- [34] A. Selamet and Z. L. Ji, "Acoustic attenuation performance of circular expansion chambers with extended inlet/outlet", *Journal of Sound and Vibration*, vol. 223, no. 2, pp. 197-212, 1999.
- [35] M. Abom, "Derivation of four-pole parameters including higher order mode effects for expansion chamber mufflers with extended inlet and outlet", *Journal of Sound and Vibration*, vol. 137, no. 3, pp. 403-418, 1990.
- [36] A. Bykaksoy and B. Polat, "A bifurcated waveguide problem", *ARI-An International Journal for Physics and Engineering Sciences*, vol. 51, no. 3, pp. 196-202, 1999.
- [37] A. D. Rawlins, "Wave propagation in a bifurcated impedance-lined cylindrical waveguide", *Journal of Engineering Mathematics*, vol. 59, no. 4, pp. 419-435, 2007.

- [38] L. Huang, "Broadband sound reflection by plates covering side-branch cavities in a duct", *The Journal of the Acoustical Society of America*, vol. 119, no. 5, pp. 2628-2638, 2006.
- [39] C. Q. Wang, L. Cheng and L. Huang, "Realization of a broadband low frequency plate silencer using sandwich plates", *Journal of Sound and Vibration*, vol. 318, no. 4-5, pp. 792-808, 2008.
- [40] A. D. Lapin, "Sound attenuation in waveguide (review)", *Soviet Physics - Acoustics*, vol. 21, no. 3, pp. 215-222, 1975.
- [41] M. Afzal, M. Ayub, R. Nawaz and A. Wahab, "Mode-matching solution of a scattering problem in flexible waveguide with abrupt geometric changes", *American Mathematical Society*, pp. 113-129, 2016.
- [42] S. Shafique, M. Afzal and R. Nawaz, "On mode-matching analysis of fluid-structure coupled wave scattering between two flexible waveguides", *Canadian Journal of Physics*, vol. 95, no. 6, pp. 581-589, 2017.
- [43] T. Nawaz, M. Afzal and R. Nawaz, "The scattering analysis of trifurcated waveguide involving structural discontinuities", *Advances in Mechanical Engineering*, vol. 11, no. 7, pp. 1-10, 2019.
- [44] M. Afzal, J. U. Satti and R. Nawaz, "Scattering characteristics of non-planar trifurcated waveguides", *Meccanica*, vol. 55, pp. 977-988, 2020.
- [45] A. D. Rawlins, "The solution of a mixed boundary value problem in the theory of diffraction by a semi-infinite plane", *Proceedings of the Royal Society A*, vol. 346, pp. 469-484, 1975.
- [46] A. D. Rawlins, "A bifurcated circular waveguide problem", *IMA Journal of Applied Mathematics*, vol. 54, no. 1, pp. 59-81, 1995.
- [47] W. Koch, "Radiation of sound from a two-dimensional acoustically lined duct", *Journal of Sound and Vibration*, vol. 55, no. 2, pp. 255-274, 1977.
- [48] J. B. Keller, "Geometric theory of diffraction", *Journal of the Optical Society of America A*, vol. 52, no. 2, pp. 116-130, 1962.

- [49] B. Noble, "Methods based on the Wiener-Hopf technique for the solution of partial differential equations", *New York, Pergamon Press*, no. 1, 1958.
- [50] S. M. Candel, "Acoustic radiation from the end of a two-dimensional duct, effects of uniform flow and duct lining", *Journal of Sound and Vibration*, vol. 28, no. 1, pp. 1-13, 1973.
- [51] P. R. Brazier-smith, "The acoustic properties of two co-planar half-plane plates", *Proceedings of the Royal Society A*, vol. 409, no. 1836, pp. 115-139, 1987.
- [52] K. U. Ingard, "Notes on the sound absorption technology", *Archives of Acoustics*, vol. 21, no. 1, pp. 115-117, 1996.
- [53] L. Huang, Y. S. Choy, R. M. C. So and T. L. Chong, "Experimental studies on sound propagation in a flexible duct", *The Journal of the Acoustical Society of America*, vol. 108, no. 2, pp. 624-631, 2000.
- [54] J. B. Lawrie and I. D. Abrahams, "An orthogonality condition for a class of problem with high order boundary conditions, applications in sound/structure interaction", *The Quarterly Journal of Mechanics and Applied Mathematics*, vol. 52, no. 2, pp. 161-181, 1999.
- [55] C. N. Wang, "Numerical decoupling analysis of a resonator with absorbent material", *Applied Acoustics*, vol. 58, no. 2, pp. 109-122, 1999.
- [56] M. E. Delany and E. N. Bazley, "Acoustical properties of fibrous absorbent materials", *Applied Acoustics*, vol. 3, no. 2, pp. 105-116, 1970.
- [57] N. Peake and I. D. Abrahams, "Sound radiation from a semi-infinite lined duct", *Wave Motion*, vol. 92, 102407, 2020.
- [58] D. P. Warren, J. B. Lawrie and I. M. Mohamed, "Acoustic scattering in waveguides with discontinuities in height and material property", *Wave Motion*, vol. 36, no. 2, pp. 119-142, 2002.
- [59] M. Hassan, "Wave scattering by soft-hard three spaced waveguide", *Applied Mathematical Modelling*, vol. 38, no. 17-18, pp. 4528-4537, 2014.

- [60] M. Hassan, M. H. Meylan , A. Bashir and M. Sumbul, “Mode-matching analysis for wave scattering in triple and pentafurcated spaced ducts”, *Mathematical Methods in the Applied Sciences*, vol. 39, no. 11, pp. 3043-3057, 2016.
- [61] M. Hassan, N. Mahvish, and R. Nawaz, “Reflected field analysis of soft-hard pentafurcated waveguide”, *Advances in Mechanical Engineering*, vol. 9, no. 5, pp. 1-11, 2017.
- [62] L. E. Kinsler, A. R. Frey, A. B. Coppens and J. V. Sanders, “Fundamentals of Acoustics (4th edition)”, 1999.
- [63] P. Morse and K. Ingard, “Encyclopedia of Physics”, *Acoustics I. Springer Verlag, Berlin*, 1961.
- [64] J. W. Brown and R. V. Churchill, “Fourier Series and Boundary Value Problems”, 1982.
- [65] T. D. Rossing, “Springer Handbook of Acoustics”, 2007.
- [66] J. B. Lawrie and I. D. Abrahams, “Scattering of fluid loaded elastic plate waves at the vertex of a wedge of arbitrary angle, I. analytic solution”, *IMA Journal of Applied Mathematics*, vol 59, pp. 1-23, 1997.
- [67] H. Afsar and Y. Akbar, “Energy distribution of bifurcated waveguide structure with planar and non-planar surfaces ”, *Mathematics and Mechanics of Solids*, pp. 1-15, 2022.
- [68] G. W. C. Kaye and T. H. Laby, “Tables of physical and chemical constants”, 15th edition, *Longman Scientific and Technical, UK*, 1986.
- [69] M. Afzal, J. U. Satti, A. Wahab and R. Nawaz, “Scattering analysis of a partitioned membrane-bounded cavity with material contrast”, *The Journal of the Acoustical Society of America*, vol. 151, pp. 31-44, 2022.